TIME DEPENDENT FAULT MECHANICS AND WAVE PROPAGATION IN ROCKS

A DISSERTATION

SUBMITTED TO THE DEPARTMENT OF GEOPHYSICS

AND THE COMMITTEE ON GRADUATE STUDIES

OF STANFORD UNIVERSITY

IN PARTIAL FULFILLMENT OF THE REQUIREMENTS

FOR THE DEGREE OF

DOCTOR OF PHILOSOPHY

by

Gerald Mathew Mavko

May 1977

I certify that I have read this thesis and that in my opinion it is fully adequate, in scope and quality, as a dissertation for the degree of Doctor of Philosophy.

Amos M. Nur
(Principal Adviser)

I certify that I have read this thesis and that in my opinion it is fully adequate, in scope and quality, as a dissertation for the degree of Doctor of Philosophy.

David M. Boore

I certify that I have read this thesis and that in my opinion it is fully adequate, in scope and quality, as a dissertation for the degree of Doctor of Philosophy.

George A. Thompson

Approved for the University Committee on Graduate Studies:

W. B. Carnochan
Dean of Graduate Studies

ABSTRACT

A number of simple mechanical models are presented for the transient or inelastic elements of a major earthquake cycle. The gross response to faulting is studied by approximating the earth's crust and upper mantle as a stiff elastic lithosphere over a weaker ductile asthenosphere. Several localized mechanisms for attenuation and material relaxation are then discussed.

In the first case the transient postseismic response of a viscous asthenosphere is examined. At time t = 0 a dislocation is introduced instantaneously into an elastic layer (lithosphere) over a viscoelastic half space (asthenosphere), representing the sudden slip of a major earthquake. The subsequent time dependent surface deformation is found analytically for a screw dislocation (strike slip fault) and approximated for an edge dislocation (dip slip fault) using the correspondence principle. The theoretical displacements agree with the postseismic deformation of the 1946 Nankaido (thrust type) earthquake. Observed amplitudes of displacements and time constants of 3-5 years yield for the asthenosphere a viscosity of 10^{19}-10^{20} poise and a 50 percent relaxation of the shear modulus.

Three partial melt models of asthenospheric relaxation are considered to account for the observed time constant of 3-5 years: large scale diffusion of melt through a porous matrix can decay over thousands to billions of years, and is much too slow. Simple shearing in "penny-shaped" cracks happens on a seismic time scale and is much too rapid. Interconnected penny-shaped cracks at different orientations with respect to the principal stresses respond an an intermediate time scale by short range

melt squirt from one crack to another, providing a reasonable mechanism to account for the transient deformation at Nankaido.

The second section focuses on the mechanics of strain accumulation and release along a major strike slip plate boundary. Assuming an elastic lithosphere a linear relation is found between the mean stress on the fault, the average fault slip and the relative plate displacement away from the fault. From this a constant applied stress boundary condition is seen to concentrate all strain changes close to the fault. In contrast a constant plate speed condition can cause a varying strain field out to distances from the fault comparable to the fault length.

Finally, two separate models are presented for the microscopic details of deformation and attenuation within the crust. In the first model dislocation theory is used to study the deformation of realistic (non-elliptical) cracks in a loaded elastic material. The cracks considered are two dimensional with non-blunted, tapered ends. Under compression the cracks shorten by closing near the crack tips. Stresses remain finite everywhere. At a given load the effective rock compressibility due to arbitrarily shaped tapered cracks depends only on crack length, giving results identical to a distribution of elliptical cracks of the same lengths. However, at different loads the varying length causes the modulus to vary.

The second model describes the attenuation of seismic waves in rocks with partially liquid saturated flat cracks or pores. The presence of at least a small fraction of a free gaseous phase permits the fluid to flow freely when the pore is compressed under wave excitation. The resulting attenuation is much higher than with complete saturation.

The attenuation is sensitive to the aspect ratios of the pores and the liquid droplets occupying the pores, with flatter pores resulting in higher attenuation. Details of pore shape other than aspect ratio appear to have little effect on the general behavior provided the crack width is slowly varying over the length of the liquid drop.

ACKNOWLEDGEMENTS

I wish to express my appreciation and gratitude to my advisor Dr. Amos Nur, for his advice and encouragement in the research and preparation of this dissertation. I would also like to thank the faculty and students of the Geophysics Department of Stanford University for useful discussions, especially Drs. M. Lee Bell and Luis Canales-L. Thanks also to Mary Dowden for her continuous help throughout my graduate career.

The love and encouragement of my wife and colleague, Barbara, made it possible for me to bear the difficulties of graduate research both at and away from the university.

This research and my graduate studies were supported by a National Science Foundation graduate fellowship as well as grants/contracts GA 36135X and DES 75-04874 from the National Science Foundation (Division of Earth Sciences); 14-08-0001-15885 from the U.S. Geological Survey; and by E(04-3) 326-P.A.#45 from the U.S. Energy Resource and Development Administration.

TABLE OF CONTENTS

Abstract		iii
Acknowledgements		vi
Part I:	Time Dependent Fault Mechanics	1
Chapter 1:	Transient Elements of the Earthquake Cycle	2
Chapter 2:	Postseismic Viscoelastic Rebound	14
Chapter 3:	Melt Squirt in the Asthenosphere	41
Chapter 4:	The Mechanics of Strain Accumulation and Release on a Strike-slip Fault	57
Part II:	The Effect of Cracks on Wave Propagation in Rocks	97
Chapter 5:	The Effect of Non-elliptical Cracks on the Compressibility of Rocks	98
Chapter 6:	Wave Attenuation in Partially Saturated Rocks	135

PART I: TIME DEPENDENT FAULT MECHANICS

CHAPTER 1

TRANSIENT ELEMENTS OF THE EARTHQUAKE CYCLE

Nature of the Observations

Most theories concerning earthquakes are based on elastic rebound--the idea that elastic strain energy is gradually stored in the earth and is abruptly released during episodes of brittle failure known as earthquakes. In the context of plate tectonics, the process of strain build-up and release at major plate boundaries repeats itself in a roughly cyclic fashion. Comparisons of the accumulation of deformation at the earth's surface before large earthquakes with the instantaneous deformation during earthquakes show that they often approximately cancel. This led to the idea of a rebound (Reid, 1910).

However, additional transient displacements, lasting from minutes to years--entirely unpredicted by elastic rebound--often accompany moderate to large earthquakes. For example, following the 1966 Parkfield, California, earthquake (M = 5.5; right-lateral strike-slip) near-surface fault creep continued, at a decaying rate, for several years. Figure 1 (from Smith and Wyss, 1968; replotted by Scholz and others, 1969) shows the postseismic fault slip inferred from five small-scale geodetic stations established in the epicentral region. Although little or no surface breakage occurred during the main event, as much as 25 cm of slip accumulated in the 3 years immediately thereafter. In addition, road damage occurring within several years before, and

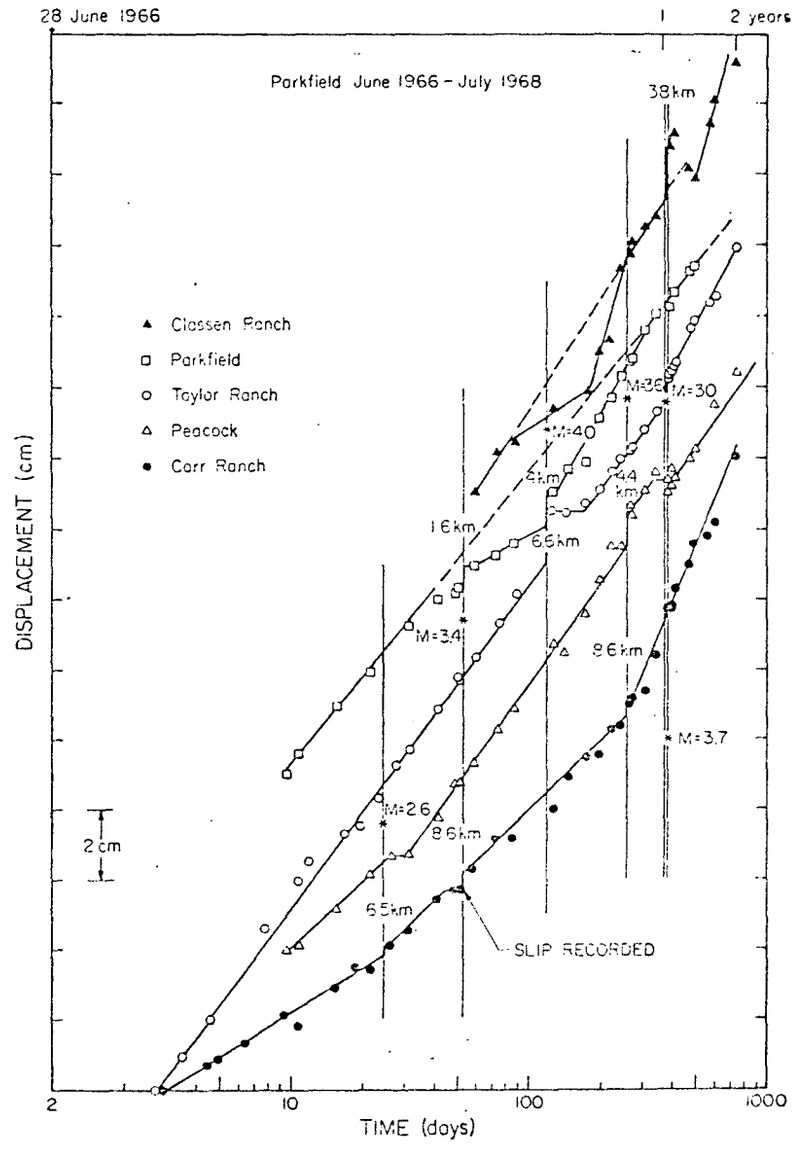

Figure 1. Cumulative slip across the fault following the Parkfield earthquake measured with five small-scale geodetic networks. The ordinate intercepts are arranged arbitrarily. The mainshock was at t = 1. (after Scholz,et al., 1969)

en-echelon cracks formed within a month before the earthquake (Allen and Smith, 1966) suggest a preseismic transient.

Even the great 1906 San Francisco earthquake, which led H. F. Reid to propose the elastic rebound mechanism, was followed by transient deformation. Thatcher (1975) suggests that substantial postseismic crustal strains, continuing for at least 30 years following the earthquake, can be inferred from geodetic resurveys since 1906. These strains can be explained (though not uniquely) by $\sim$4 m of aseismic fault slip from 10 to 30 km depth, without additional surface slip. Thatcher (1975) also suggests anomalously rapid strain accumulation during the 50 years prior to 1906, although the evidence is weak.

Perhaps the most spectacular example of measureable postseismic deformation was observed following the 1946 Nankaido, Japan, earthquake (M = 8.2; thrust type) where upheavals of as much as 2 m occurred over a 1 to 3 year period. Figure 2 (from Matuzawa, 1964; Kanamori, 1973) shows the rather complicated nature, in space and time, of the vertical displacement. The transient mechanism has been interpreted either as aseismic fault slip at depth (Fitch and Scholz, 1971) or viscoelastic rebound of the asthenosphere without fault slip (see Chap. 2; also Nur and Mavko, 1974). A similar analysis of postseismic uplift following the 1964 Alaskan (thrust type) earthquake is reported by Brown and others (1976). In this case the transient decay lasted about 1 to 8 years depending on distance from the fault trace, and was attributed to fault slip.

Particularly short-lived transients have also been observed. Figure 3 shows fault slip lasting only several hours, recorded after a Matsushiro shock on September 6, 1966 (data from Nakamura and Tsuneishi,

a

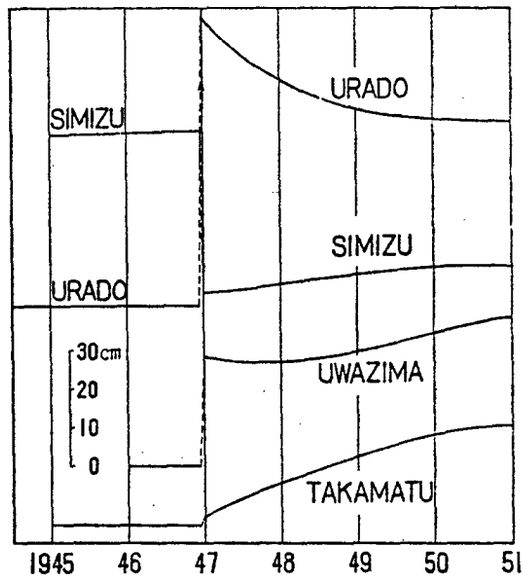

b

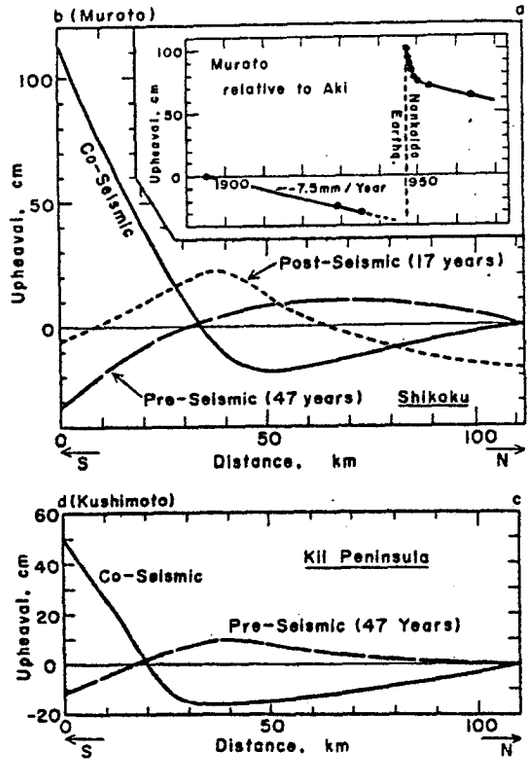

Figure 2. Deformation accompanying the 1946 Nankaido earthquake.

(a) Smoothed sea level at four tide guage stations (after Matuzawa,1964).

(b) Pre-, co-, and postseismic vertical deformation along profiles roughly normal to the fault trace (after Kanamori, 1973).

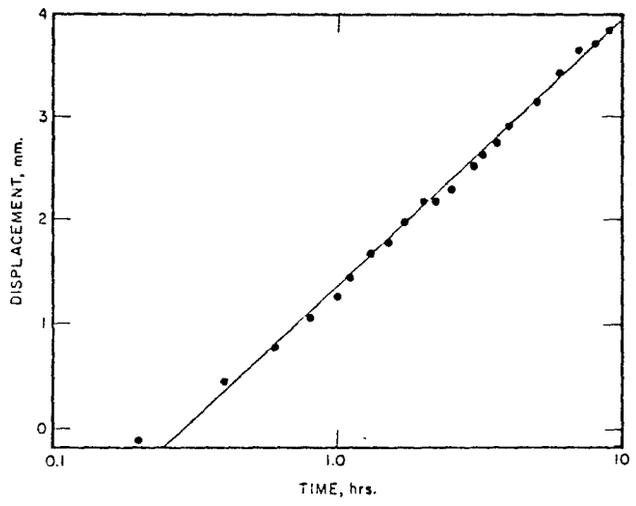

Figure 3. Fault slippage following the magnitude 5.0 earthquake of September 6, 1966 at Matsushiro. (data from Nakamura and Tsuneishi, 1967; replotted by Scholz, 1972)

1967; replotted by Scholz, 1972). A precursory aseismic slip with time constant of 300 to 600 sec, starting about 1000 sec before the main shock of the 1960 Chilean earthquake has been inferred from long-period surface waves and body waves (Kanamori and Cipar, 1975) and from free oscillations (Kanamori and Anderson, 1975).

Further examples of transient deformation are reviewed by Scholz (1972), Kanamori (1973) and Dunbar (1977).

In general these observations of pre- and postseismic deformation are rarely better than qualitative evidence of transient phenomena. The reliability and spatial distribution of geodetic data is particularly poor, and the time window of all observations is seldom greater than a few tens of years. Unambiguous interpretation of the mechanism is usually impossible. Nevertheless, useful information about the earthquake cycle can be gained from these observations:

1. The relaxation spectrum. Order of magnitude estimates of the characteristic times of transients, whether they occurred before or after an earthquake, or perhaps the lack of a transient, can put constraints on proposed mechanisms.

2. Scale. The approximate spatial dimensions and orientation of the anomalous strain field can be an indication of the relaxation mechanism and its depth.

A number of specific transient mechanisms and their relation to these observations will be discussed throughout Part I of this thesis. In particular we identify some potentially important relaxation processes in the next section. Some simple strike-slip and dip-slip fault models will be examined in Chapters 2 and 4.

The Viscous Element

In a strictly elastic earth, complete elastic rebound would take place in a few seconds, with the characteristic time of strain release determined by the seismic source rise time, fault dimensions, and rupture velocity. The only slow deformation would be the accumulation of tectonic strain. In contrast, the observed pre- and postseismic transients indicate a much broader relaxation spectrum. Our concept of plate tectonics suggests steady plate motion over a period of at least several seismic cycles (10^2 to 10^3 years), and we might expect a steady accumulation of strain between earthquakes. However, episodes of accelerated strain are observed indicating a localized viscous instability which can initiate and arrest each strain event. Furthermore, seismic precursors and postseismic transients imply a rate-dependent damping associated with the otherwise brittle release of energy.

What are these transient mechanisms? A simple mechanical model for the earth's crust and upper mantle, suggested by plate tectonics, consists of a relatively elastic brittle lithosphere overlying a viscous, ductile asthenosphere. Geometrically we can distinguish three general sources of relaxation within this model:

1. Relaxation in the asthenosphere. The asthenosphere is characterized by high temperature relaxation mechanisms. Solid mineral grains can flow plastically by atomic diffusion and the motion of lattice dislocations (e.g. Gordon, 1965; Weertman and Weertman, 1975; Heard, 1976). This makes the polycrystalline composite fluidlike over long time scales and can account for the large-scale, finite

deformation implied by plate motion and the low strength implied by isostatic equilibrium. In addition, enhanced deformation at grain boundaries can occur resulting from dislocation motion and diffusion (e.g. Ke, 1947; Zener, 1948; Anderson, 1967) or the viscous flow of melt (Walsh, 1969; Mavko and Nur, 1975). Other loss mechanisms which are relevant at seismic frequencies include thermoelastic, dislocation damping, point defect diffusion, and grain boundary effects (e.g. Anderson, 1967). We will discuss in more detail the possible role of asthenospheric relaxation during major earthquake faulting in Chapters 2, 3 and 4.

2. Relaxation in the lithosphere. Based on analyses of glacial rebound and lithospheric flexure (Walcott, 1973), the gross behavior of the lithosphere appears to be essentially elastic on time scales of up to several major earthquake cycles (10^2 to 10^4 years). Therefore it seems unlikely that large-scale plastic flow or solid-state creep in the lithosphere is important as a transient mechanism. (We will discuss fault creep separately.) However, a smaller scale viscoelastic response to sudden changes in the stress field might result from concentrated plastic flow at grain boundaries in the hot lower lithosphere and from frictional sliding or viscous shearing of water at grain boundaries and fractures in the shallow crust. Regional diffusion of water in response to dilatancy (Nur, 1973) or the sudden change of stress field due to an earthquake (Nur and Booker, 1972) might also occur in the shallow crust.

3. Fault creep. In addition to direct observations of surface fault creep aseismic fault slip has been invoked at depth in the lithosphere to explain pre- and postseismic surface deformation

(e.g. Fitch and Scholz, 1971; Thatcher, 1975; Brown and others, 1976). However, very little is known about the detailed stress-strain behavior of the fault zone, and hence the physical mechanism of creep, at any depth. Nason and Weertman (1973) conclude little more than the existence of an upper yield phenomenon from shallow creep events. In the laboratory transient stable sliding sometimes precedes stick slip on frictional surfaces (Scholz and others, 1969) at conditions corresponding to several kilometers depth. At higher temperatures and pressures Stesky (1974) observes a nonlinear stress-strain rate sliding law similar to that expected for solid-state creep. In Chapter 3 we discuss some general effects of fault slip on strain accumulation along a major strike-slip fault.

References

Allen, C.R., and S.W. Smith, Parkfield earthquakes of June 27-29, Monterey and San Luis Obispo counties, California. Pre-earthquake and post-earthquake surficial displacements, Bull. Seismol. Soc. Am., 56, 966-967, 1966.

Anderson, D.L., The anelasticity of the mantle, Geophys. J. R. Astr. Soc., 14, 135-164, 1967.

Brown, L.D., R.E. Reilinger, S.R. Holdahl, and E.I. Balazs, Post-seismic crustal uplift near Anchorage Alaska, preprint, 1976.

Dunbar, W.S., The Determination of Fault Models from Geodetic Data, Ph.D. Thesis, Stanford University, 1977.

Fitch, T. and C.H. Scholz, Mechanism of underthrusting in Southwest Japan: a model of convergent plate interactions, J. Geophys. Res., 80, 11, 1444-1447, 1975.

Gordon, R.B., Diffusion creep in the earth's mantle, J. Geophys. Res., 70, 10, 2413-2418, 1965.

Kanamori, H., Mode of strain release associated with major earthquakes in Japan in Annual Review of Earth and Planetary Sciences vol. 1, edited by F.A. Donath, F.G. Stehli, and G.W. Wetherill, Annual Reviews, Palo Alto, Ca., 1973.

Heard, H.C., Comparison of the flow properties of rocks at crustal conditions, Phil. Trans. R. Soc. Lond. A. 283, 173-186, 1976.

Kanamori, H. and D.L. Anderson, Amplitude of the earth's free oscillations and long period of the earthquake source, J. Geophys. Res., 80, 8, 1075-1078, 1975.

Kanamori, H. and J.J. Cipar, Focal processes of the great Chilean

earthquake, May 22, 1960, Phys. Earth Planet. Interiors, 9, 128-136, 1974.

Ke, T.S., Experimental evidence of the viscous behavior of grain boundaries in metals, Phys. Rev., 71, 533, 1947.

Matuzawa, T., Study of Earthquakes, Uno Shoten, Tokyo, 1964

Mavko, G. and A. Nur, Melt squirt in the asthenosphere, J. Geophys. Res., 80, 11, 1444-1447, 1975.

Nakamura, K. and Tsuneishi, Ground cracks at Matsushiro probably of strike-slip fault origin, Bull. Earthquake Res. Inst. Univ. Tokyo, 45, 417-472, 1967.

Nur, A., Role of pore fluids in faulting, Phil. Trans. R. Soc. Lond. A., 274, 297-304, 1973.

Nason, R. and J. Weertman, A dislocation theory analysis of fault creep events, J. Geophys. Res., 78, 32, 7745-7751, 1973.

Nur, A. and J. R. Booker, Aftershocks caused by pore fluid flow?, Science, 175, 885-887, 25 Feb 1972.

Nur, A. and G. Mavko, Postseismic viscoelastic rebound, Science, 183, 4121, 204-206, 1974.

Reid, H. F., The mechanics of the earthquake, in: The California Earthquake of April 18, 1906. Rept. State Earthquake Invest. Comm., Carnegie Inst., Washington, D.C., 1910.

Scholz, C.H., Crustal movements in tectonic areas, In: E.F. Savarensky and T. Rikitake (Editors) Forerunners of Strong Earthquakes, Tectonophysics 14(3/4), 201-217, 1972.

Scholz, C.H., M. Wyss and S.W. Smith, Seismic and aseismic slip on the San Andreas fault, J. Geophys. Res., 74, 8, 2049-2069, 1969.

Smith, S.W., and M. Wyss, Displacement on the San Andreas fault

initiated by the 1966 Parkfield earthquake, Bull. Seismol. Soc. Am., 58, 1955-1974, 1968.

Stesky, R.M., Steady-state creep law for frictional sliding at high temperature and pressure, abstract in EOS, 55, 4, 1974.

Thatcher, W., Strain accumulation and release mechanism of the 1906 San Francisco earthquake, J. Geophys. Res., 80, 35, 4862-4872, 1975.

Walcott, R.I., Structure of the earth from glacioisostatic rebound, in Annual Review of Earth and Planetary Sciences, vol. 1, edited by F.A. Donath, F.G. Stehli, and G.W. Wetherill, Annual Reviews, Palo Alto, Ca., 1973.

Walsh, J.B., A new analysis of attenuation in partially melted rock, J. Geophys. Res., 74, 4333, 1969.

Weertman, J. and J.R. Weertman, High temperature creep of rock and mantle viscosity in Annual review of Earth and Planetary Sciences, vol. 3, edited by F.A. Donath, F.G. Stehli, and G.W. Wetherill, Annual Reviews, Palo Alto, Ca., 1975.

Zener, C., Elasticity and Anelasticity of Metals, University of Chicago Press, Chicago, 1948.

CHAPTER 2

POSTSEISMIC VISCOELASTIC REBOUND

A simple, widely accepted model for the mechanical behavior of the earth's crust and upper mantle consists of a relatively elastic, brittle lithosphere overlying a viscous, ductile asthenosphere. Evidence for the existence of the asthenosphere comes from the viscous rebound of the crust upon removal of surface loads such as the post glacial uplift of Fennoscandia (Walcott, 1973), and Lake Bonneville (Crittenden, 1963) where rebound followed the disappearance of the water load. The brittleness and elasticity of the lithosphere are implied by the abundance of crustal earthquakes and the associated elastic rebound.

In a strictly elastic earth, complete elastic rebound would take place in a few seconds, and the only slow deformation would be the accumulation of tectonic strain. In contrast, in an earth with a viscous element, a large earthquake would consist of an initial elastic rebound, followed by a transient element of deformation controlled by the viscosity.

The purpose of this study is to construct a dislocation model which will enable us to estimate the time constant, the magnitude, and the spatial distribution of the viscously induced post earthquake deformation in the crust and upper mantle. We will then compare some available rebound data with the theoretical results, in order to

determine whether viscous deformation plays any important role in postseismic deformation.

The Dislocation Model

The problem is to determine the characteristics of time dependent deformation which follows the sudden slip on large earthquake faults in an earth which has an elastic lithosphere and a viscoelastic asthenosphere. The distribution of viscosity, and the dependence of viscosity on stress in some regions of the asthenosphere are probably quite complex. Furthermore, the slip on faults during large earthquakes may also be rather complicated. Generally slip is not uniform over the fault plane and the relative strength of its vertical and horizontal components are variable in space.

Because of lack of detailed information concerning either viscosity in the earth or slip distributions on large faults, we will consider a very simple model of the lithosphere-asthenosphere composite and a very simple model of a large fault. The lithosphere will be represented by a single elastic layer with thickness H, overlying a linear viscoelastic half space as shown in figure 1.

We consider two types of faults. A strike-slip fault will be represented by a single screw dislocation in the elastic layer, with a dislocation line at depth $D < H$ below the free surface of the layer. A thrust fault will be represented by an edge dislocation in the elastic layer, with a dislocation line at depth $D < H$, and with a slip surface with dip θ, measured from the free surface, as shown in figure 1.

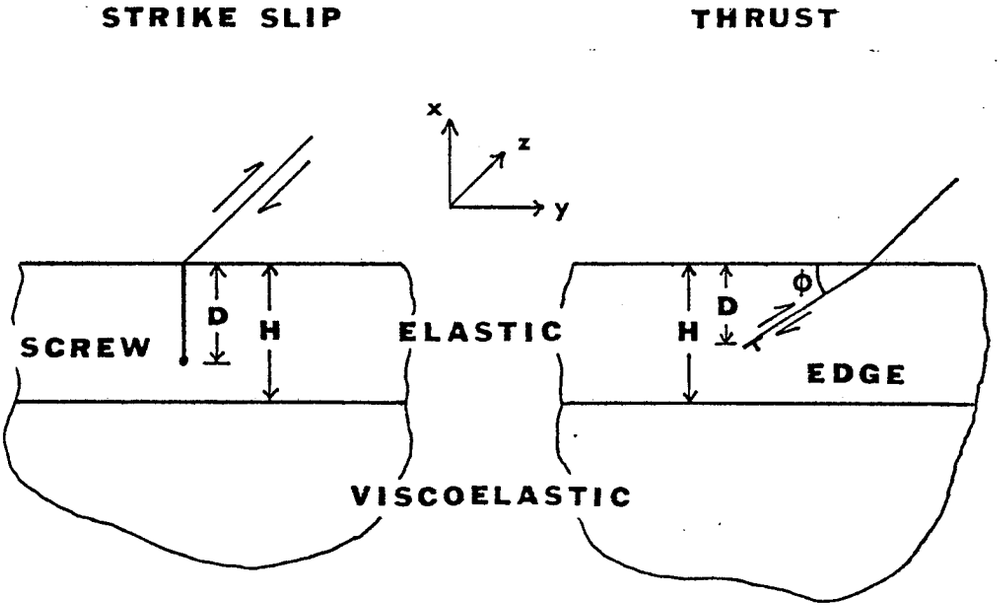

Figure 1. Simple models for earthquakes in an elastic lithosphere over a viscoelastic asthenosphere. A strike slip fault is modelled by a screw dislocation, and a thrust fault by an edge, introduced at $t = 0$.

We will further simplify the problem by ignoring the process of tectonic stress buildup. Instead, we will assume that at time t = 0 sufficient tectonic stress has accumulated to cause sudden slip or stress drop on the fault.

Method of Solution

The solution to the elastic-viscoelastic problem is obtained in two steps. In the first step we solve for the static displacements and stresses in an elastic layered model with welded contacts. In the second step we make use of the correspondence principle and the Laplace transform to obtain the time dependent solution.

Screw and Edge Dislocations in the Elastic Composite

Consider a two dimensional elastic layer (region 1) with shear modulus μ_1, bulk modulus K_1, Poisson's ratio ν_1 and thickness H, over an elastic half space (region 2) with shear modulus μ_2, bulk modulus K_2, and Poisson's ratio ν_2. The surface x = 0, where x is upward, is the free surface.

In one case we introduce at depth D a screw dislocation line parallel with the z direction and with slip Δu, as shown in figure 1. The slip plane (mathematically, the branch cut) lies in the vertical plane y = 0 ($x \geq -D$). The deformation associated with such a screw dislocation is completely described by a single component of displacement u_z and the corresponding two shear stresses σ_{xz} and σ_{yz}.

In the other case, an edge dislocation with constant slip Δu is placed at depth D, parallel with the z direction. The slip plane, with arbitrary dip ϕ, extends upward from the dislocation line in the

positive x and y directions. Here the deformation is described by the displacements u_x and u_y and the stresses σ_{xx}, σ_{yy}, and σ_{xy}.

In the earth, we can measure directly only the deformation of the free surface. For the screw the displacement at this surface (x = 0) in our model is (see appendix)

$$u_z = \frac{\Delta u}{\pi}\left[\tan^{-1}\left(\frac{y}{D}\right) + \sum_{n=1}^{\infty}\left[\frac{\mu_1-\mu_2}{\mu_1+\mu_2}\right]^n\left[\tan^{-1}\left(\frac{y}{2nH+D}\right) - \tan^{-1}\left(\frac{y}{2nH-D}\right)\right]\right] \quad (1)$$

The jump Δu at y = 0 is the offset on the slip plane. When $\mu_1 = \mu_2$, u_z reduces to the well known expression for a screw dislocation in an elastic half space. When $\mu_2 = 0$, u_z describes the surface deformation of a traction-free elastic layer with an internal screw dislocation.

For the edge dislocation, the free surface (x = 0) displacements in our model are given approximately by

$$u_x = \Delta u\left\{\frac{(1-\frac{\mu_2}{\mu_1})}{(1+\delta_1\frac{\mu_2}{\mu_1})}(f_1+f_1') + \frac{(\delta_2-\delta_1\frac{\mu_2}{\mu_1})}{(\delta_2+\frac{\mu_2}{\mu_1})}(f_2+f_2') + (f_3+f_3')\right\}$$

$$u_y = \Delta u\left\{\frac{(1-\frac{\mu_2}{\mu_1})}{(1+\delta_1\frac{\mu_2}{\mu_1})}(g_1+g_1') + \frac{(\delta_2-\delta_1\frac{\mu_2}{\mu_1})}{(\delta_2+\frac{\mu_2}{\mu_1})}(g_2+g_2') + (g_3+g_3')\right\} \quad (2)$$

where Δu is the magnitude of the burgers vector; $\delta_i = 3 - 4\nu_i$; and f_i, f_i', g_i, and g_i' are geometric factors given in the appendix. The exact solution for an edge dislocation parallel to the boundary of two joined elastic half spaces is given by Mura (1968). The solution for an edge dislocation in a layer over a half space can be constructed by evaluating the tractions at the desired free surface in the two joined half spaces problem and superimposing a solution that exactly cancels the tractions at the free surface. Lee and Dundurs (1973) do this for the case of an edge dislocation with the burgers vector

normal to the free surface, but even with the loss of generality the expression is unwieldy. Here the free surface displacements, equations (2) are approximated by placing two equal and opposite edge dislocations in an elastic half space, sharing a common slip plane. A plane midway between the two ($x = 0$) will represent the "free surface," and the displacement at this plane is taken as roughly proportional to the exact solution.

The Viscoelastic Problem

Suppose now that the lower half space is not elastic, but viscoelastic. The correspondence principle provides an easy method to obtain the slow, time dependent deformation in response to the sudden deformation of a dislocation created at time zero. The principle states that any formal solution of Navier's equation in the classical theory of linear elasticity offers a corresponding solution for a viscoelastic body, provided the elastic moduli are replaced by corresponding complex moduli in dynamic problems and a Laplace operator in the static one. It is also necessary that the elastic and viscoelastic problems have identical boundary conditions. If the viscous behavior is due to a shear process such as creep or relaxation of viscous fluid in pockets of melt, then only the shear modulus μ_2 must be replaced by the corresponding Laplace operator. For a standard linear viscoelastic solid the Laplace operator $\bar{\mu}$ is

$$\bar{\mu}(s) = \frac{1}{2}\frac{b_0 + b_1 s}{a_0 + a_1 s} \tag{3}$$

where a_0, a_1, b_0, and b_1 are constants in the generalized relations between the shear stress σ_{ij} and shear strain ε_{ij} $(i \neq j)$:

$$(a_0 + a_1\frac{\partial}{\partial t})\ \sigma_{ij} = (b_0 + b_1\frac{\partial}{\partial t})\ \varepsilon_{ij} \qquad (i \neq j) \tag{4}$$

and s is the transform variable. Note that when $a_1 = b_1 = 0$, equation (4) gives the relations for a linear elastic solid with shear modulus $\mu = b_0/2a_0$ and when $a_1 = b_0 = 0$, it yields the relations for a Newtonian fluid, with viscosity $\eta = b_1/2a_0$. Only shear relaxation is considered, the bulk modulus K_2 for the half space kept constant.

In order to obtain the complete viscoelastic solution, it is also necessary to introduce the initial condition that Δu is a Heaviside step function:

$$\Delta u(t) = \Delta u\ H(t)$$

The Laplace transform of this condition is

$$\overline{\Delta u} = \frac{\Delta u}{s}$$

Substituting $\overline{\mu}$ and $\overline{\Delta u}$ into the elastic solutions, equations (1) and (2), and taking the inverse Laplace transform yields the following time dependent displacements at the free surface (see appendix).
For the screw

$$u_z(t) = \frac{\Delta u}{\pi}\tan^{-1}\frac{y}{D} + \frac{\Delta u}{\pi}\sum_{n=1}^{\infty}\left(\tan^{-1}\frac{y}{2nH+D} - \tan^{-1}\frac{y}{2nH-D}\right) F_n(t) \qquad t > 0$$

and for the edge

$$u_x(t) = \Delta u[A(t)(f_1+f_1^i) + B(t)(f_2+f_2^i) + (f_3+f_3^i)] \qquad t > 0$$

$$u_y(t) = \Delta u[A(t)(g_1+g_1^i) + B(t)(g_2+g_2^i) + (g_3+g_3^i)] \qquad t > 0$$

where $F_n(t)$, $A(t)$ and $B(t)$ are time functions given in the appendix.

Discussion of Theoretical Results

The most important feature of both the edge and screw dislocation models is the change with time of the surface deformation from an

initial configuration toward a final relaxed state. Figure 2 shows the horizontal surface displacement for a vertical strike-slip fault, and figure 3, the vertical displacement for a thrust fault with 30° dip. In both cases the ordinate is in units of fault slip and the abscissa is in units of elastic layer thickness; both plots are for faults extending to a depth of 0.75 the layer thickness. The limiting cases, at times $t = 0$ and $t = \infty$, are found by substituting $\mu_2 = \mu(0)$ and $\mu_2 = \mu(\infty)$ respectively into the elastic solutions, where $\mu(0)$ and $\mu(\infty)$ are the unrelaxed and relaxed moduli respectively.

Certain features are common to both models. First, the overall amplitude of the surface displacement is determined by and proportional to the fault slip, being largest right at the slip plane and tending to zero far from the fault. For fixed material constants (and fixed dip in the dip-slip case) variations in fault depth simply stretch or shrink the horizontal scale without changing the basic shape of deformation. Shallower faults have a much more localized effect; deeper faults, much broader. Deeper faults are also accompanied by a larger and hence more measurable change in displacement with time between initial and relaxed states, especially at distances of one to five layer thicknesses from the fault trace (on the hanging wall side of a thrust).

Similarly, a greater change in displacement between initial and relaxed states, without change in the horizontal scale, is accomplished with a lower ratio of final viscoelastic shear modulus to initial viscoelastic shear modulus, permitting a higher degree of relaxation of the half space.

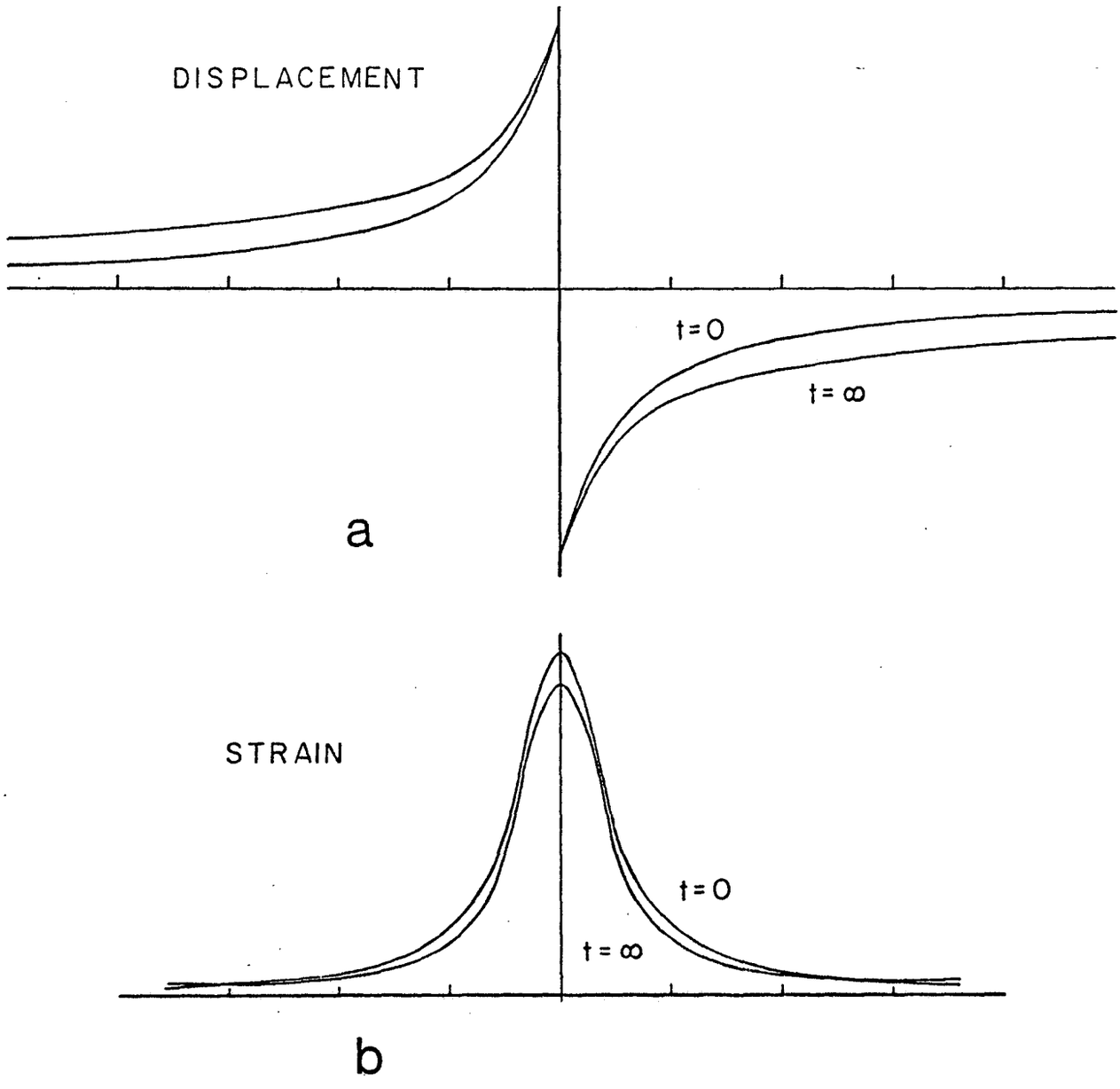

Figure 2. Horizontal displacement and strain at the free surface for the strike slip case. The initial deformation at t = 0 is the coseismic part. As the asthenosphere relaxes the deformation approaches the curves t = ∞.

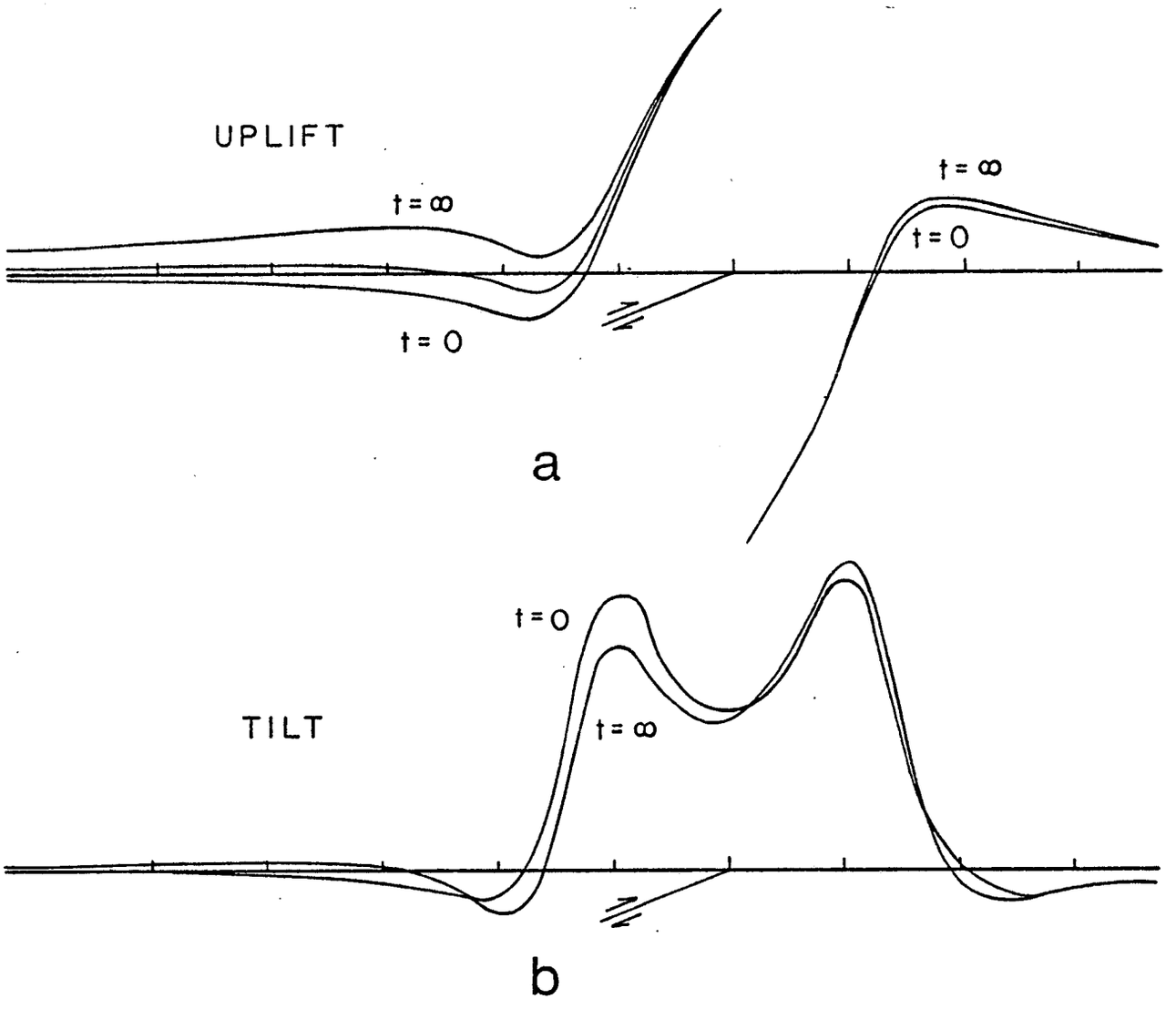

Figure 3. Vertical displacement and tilt at the free surface for the thrust case.

The time dependent deformation, following the introduction of a screw dislocation spreads away from the fault with time, as shown in figure 2. Although the large initial displacement (fig. 2a) is confined to a distance of about two layer thicknesses from the fault, the subsequent slow change of displacement with time is pronounced at much greater distances. The initial shear strain (fig. 2b) is high and localized. With time its magnitude on the fault itself decreases, indicating a corresponding recovery of the initial stress drop, and it also spreads out.

The time dependent displacements shown in figure 2a always increase with time in the same sense as the initial motions at time zero. However, the sense of strain change with time depends on position. Beyond about three layer thicknesses from the fault, strain varies with time in the same sense as the initial strain; however, near the fault, strains clearly slow recovery in the opposite sense to initial strains.

The sudden appearance of the edge dislocation in the model produces initial surface displacement and tilts similar to values in an elastic half space (fig. 3). As time progresses the deformation changes due to the relaxation of the shear modulus in the lower half space, and the surface displacement spreads out. For example, the hinge point (at which the vertical displacement changes from upward to downward) moves away from the surface break, as shown in figure 3a.

The tilts of the surface, normal to the fault strike, are shown in figure 3b. Although the region of large tilt is confined to within approximately two layer thicknesses of the fault, the changes with time, relative to the initial tilt, occur over a broader area, as far away

as four or five layer thicknesses. Unlike the deformation in a homogeneous viscoelastic half space, the redistribution of displacement and tilt measured at fixed points on the surface as a function of time show complicated patterns. There are points in which the viscous displacement is in the same sense as the initial displacement. In other regions the sense is reversed. Similar complexity is apparent in the changes of tilt with time. These complexities arise not because of the viscoelastic zone but are due to the inhomogeneous structure. In a homogeneous viscoelastic half space the time dependent displacements and tilts do not change in sense anywhere.

The time behavior of the slow transient deformation is derived in the appendix for both the screw and edge dislocations. In detail the behavior is fairly complicated. However, in each case the initial relaxation is approximately exponential, with a time constant of

$$\tau \simeq \alpha\eta/\mu_1 \qquad (5)$$

where η is the viscosity of the viscoelastic asthenosphere and μ_1 is the rigidity of the elastic lithosphere. The constant α depends on the ratio of asthenospheric rigidity to lithospheric rigidity as well as on the amount of viscoelastic relaxation. For moderate amounts of relaxation, i.e. $0.2 < \mu(\infty)/\mu(0) < 0.8$, and $1 < \mu_1/\mu(0) < 2$ the value of α lies between 1 and 10. Thus, to a first order approximation, we might use $\tau \simeq 5\eta/\mu_1$.

Application to the Earth

Our models show that crustal earthquakes with sufficiently deep faults should be followed by measurable postseismic deformation, if

some region in the mantle is indeed viscous (and part of the crust elastic). The most spectacular example of postseismic deformation was obtained following the Nankaido, Japan, 1946 thrust-type earthquake (M = 8.2, December 20, 1946).

In figure 4a we compare the results computed from a selected edge dislocation model (dip 30°, depth 0.75 of the layer thickness) with the observed coseismic and postseismic deformation along a profile perpendicular to the surface break, reproduced from Kanamori (1973).

The computed and the observed initial coseismic vertical displacement are quite similar, both showing a zone of great uplift next to the fault, and a broad zone of subsidence further away. The theoretical postseismic vertical displacement is obtained by subtracting the initial displacement from the final one, and the observed postseismic displacement is obtained from changes in beach levels during the 17 year period following the earthquake.

The similarity between the two postseismic curves is striking. In both, most of the postseismic recovery takes place in the broad region of initial subsidence, and in both the amplitude of recovery is of the same order of magnitude as the initial amplitude of subsidence. This indicates that the postseismic deformation of the Nankaido earthquake results in all likelihood from viscous adjustments in the lower crust or the upper mentle of the earth.

In figure 4b we compare computed displacement time functions at selected points with observed vertical displacements measured at beaches on Shikoku Island (Kanamori, 1973). Both displacement sets show the initial, coseismic displacement, followed by slow added deformation; and both

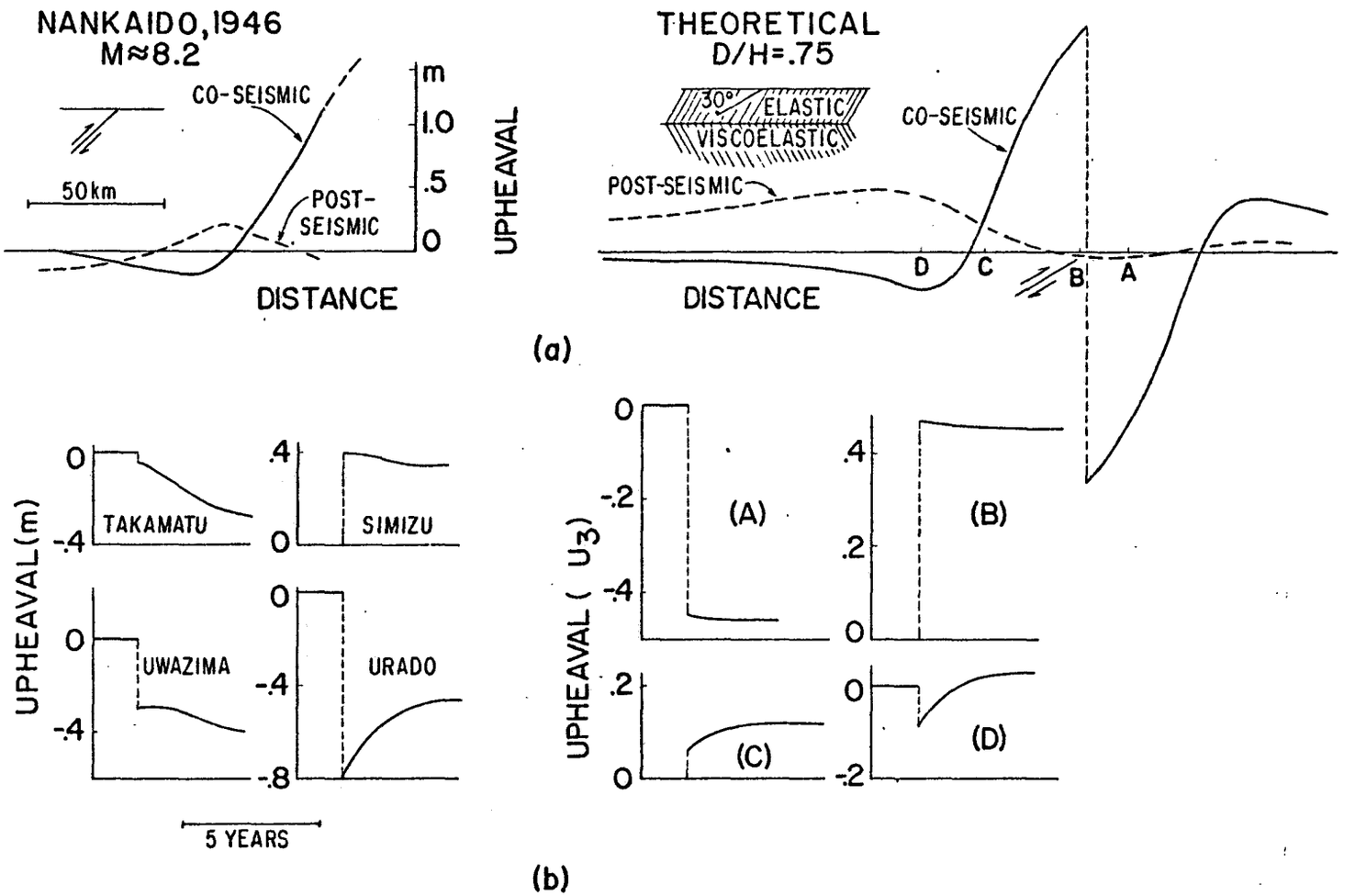

Figure 4. Comparison between theoretical and observed seismic and postseismic deformation. (a) Spatial distribution of vertical displacements. (b) Vertical displacement time functions at selected points.

sets show large, similar variation of these shapes over small horizontal distances.

The decay time τ for the observed deformation is of the order of 5 years. Taking an average crustal shear modulus $\mu_1 = 8 \cdot 10^{11}$ dyne/cm^2, $\tau = 1.6 \cdot 10^8$ sec and $\alpha = 5$, we obtain the viscosity $\eta = 5 \cdot 10^{19}$ poise. This value is in gratifying agreement, though not identical, with estimates based on very long viscous rebound from crustal loading in Fennoscandia and North America. The amplitude of observed transient deformation indicates roughly a 50 percent relaxation of the shear modulus of the asthenosphere.

The agreement between the postseismic data and the model, based on the current concepts of plate tectonics, provides not only an attractive explanation for postseismic deformation of large earthquakes, but also a new confirmation that the asthenosphere behaves viscously, even over short periods of time. Careful monitoring of deformation following large earthquakes may thus be used as a new tool for studying the mantle, and help to unravel the poorly understood physical processes responsible for its overall rheology.

Appendix

Elastic Solution, Screw Dislocation

The elastic solution to this problem is well known and can be found in Chou (1966), Rybicki (1971) or Chinnery and Jovanovich (1972). Consider the geometry shown in figure 5a. An infinite elastic slab (region 1) of thickness H and shear modulus μ_1 is sandwiched between two elastic half spaces (regions 0 and 2) with rigidities μ_0 and

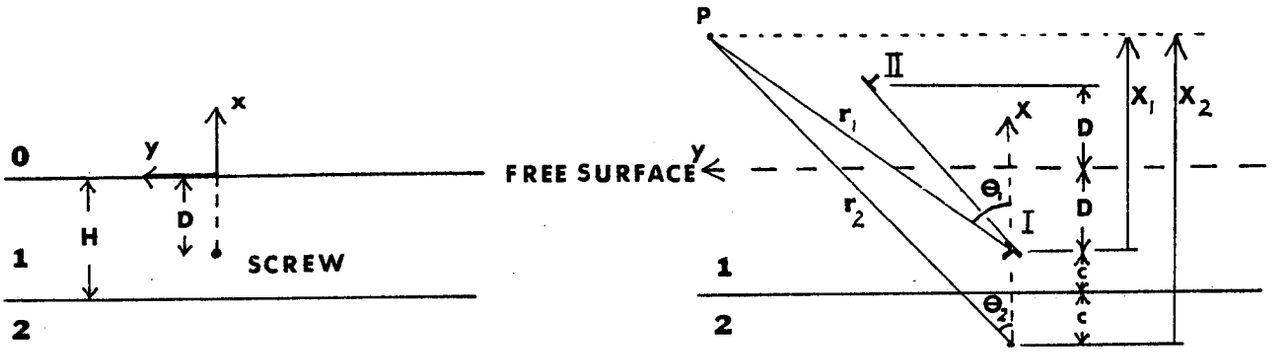

a b

Figure 5. Dislocation models in layer-half space composites, showing dimensions.

μ_2 respectively. A screw dislocation with axis parallel to the z direction and burgers vector Δu is inserted at a depth $x = -D$.

Since the behavior at the surface $x = 0$ is sought, it is only necessary to find the displacements in region 1. The effect of the surfaces at $x = 0$ and $x = -H$ can be included by replacing these surfaces with an infinite distribution of image dislocations. Each has a displacement field $u_z(x,y)$ of the form

$$u_z = \frac{b_i}{2\pi} \tan^{-1}\left(\frac{y}{x-a_i}\right) \tag{A-1}$$

where b_i is the burgers vector and a_i is the position of the dislocation or image along the x axis; the values b_i diminish in size as $|a_i|$ increases, allowing the infinite series to converge.

Summing over the contributions from all dislocations the total displacement in region 1 is given by

$$u_z = \frac{\Delta u}{2\pi}\left\{\tan^{-1}\left(\frac{y}{x+D}\right) + K\cdot\tan^{-1}\left(\frac{y}{x-D}\right) + \sum_{n=1}^{\infty}(MK)^n\left[\tan^{-1}\left(\frac{y}{x-2nH+D}\right) + \tan^{-1}\left(\frac{y}{x+2nH+D}\right) + K\cdot\tan^{-1}\left(\frac{y}{x-2nH-D}\right) + \frac{1}{K}\tan^{-1}\left(\frac{y}{x+2nH-D}\right)\right]\right\} \tag{A-2}$$

and the shear stress $\sigma_{yz} = \mu_1(\partial u_z/\partial y)$ is

$$\sigma_{yz} = \mu_1\frac{\Delta u}{\pi}\left\{\frac{x+D}{y^2+(x+D)^2} + K\frac{x-D}{y^2+(x-D)^2} + \sum_{n=1}^{\infty}(MK)^n\left[\frac{x-2nH+D}{y^2+(x-2nH+D)^2} + \frac{x+2nH+D}{y^2+(x+2nH+D)^2} + K\frac{x-2nH-D}{y^2+(x-2nH-D)^2} + \frac{1}{K}\frac{x+2nH-D}{y^2+(x+2nH-D)^2}\right]\right\} \tag{A-3}$$

where

$$K = \frac{\mu_0 - \mu_1}{\mu_0 + \mu_1} \qquad \text{and} \qquad M = \frac{\mu_2 - \mu_1}{\mu_2 + \mu_1}.$$

If the surface $x = 0$ is a free surface, i.e. $\mu_0 = 0$ and $K = -1$, then the displacement u_z at the surface is

$$u_z(0,y) = \frac{\Delta u}{\pi}\left\{\tan^{-1}\left(\frac{y}{D}\right) + \sum_{n=1}^{\infty}(-M)^n\left[\tan^{-1}\frac{y}{2nH+D} - \tan^{-1}\frac{y}{2nH-D}\right]\right\} \qquad (A-4)$$

and the shear stress σ_{yz} is

$$\sigma_{yz}(0,y) = \frac{\Delta u}{\pi}\left\{\frac{D}{y^2+D^2} + \sum_{n=1}^{\infty}(-M)^n\left[\frac{2nH+D}{y^2+(2nH+D)^2} - \frac{2nH-D}{y^2+(2nH-D)^2}\right]\right\}. \qquad (A-5)$$

Elastic Solution, Edge Dislocation

An elastic half space (region 1) with shear modulus μ_1 and Poisson's ratio ν_1 is in welded contact with a second half space (region 2) with shear modulus μ_2 and Poisson's ratio ν_2, as shown in figure 5b. The exact displacements in region 1 due to a single edge dislocation I, lying in region 1 parallel to the z direction, are given by (Mura, 1968)

$$u_x = \Delta u(Af_1 + Bf_2 + f_3)$$
$$u_y = \Delta u(Ag_1 + Bg_2 + g_3) \qquad (A-6)$$

where Δu is the magnitude of the burgers vector,

$$A = (1 - \mu_2/\mu_1)/(1 + \delta_1(\mu_2/\mu_1))$$

$$B = (\delta_2 - \delta_1\mu_2/\mu_1)/(\delta_2 + \mu_2/\mu_1)$$

$$\delta_1 = 3 - 4\nu_1$$

$$\delta_2 = 3 - 4\nu_2$$

$$f_1 = \frac{-1}{2\pi(\delta_1+1)}\left[\sin\phi\left[\theta_2\delta_1 + \frac{2x_2y}{r_2^2} + 2c\left((\delta_1-1)\frac{y}{r_2^2} + \frac{4x_2^2y}{r_2^4} - 4cx_2y/r_2^4\right)\right]\right. \qquad (A-7)$$
$$\left. + \cos\phi\left[\delta_1 \ln r_2 - \frac{2x_2^2}{r_2^2} + 2c\left((\delta_1-1)\frac{x_2}{r_2^2} + \frac{4x_2^3}{r_2^4} + \frac{2c}{r_2^2} - \frac{4cx_2^2}{r_2^4}\right)\right]\right]$$

$$f_2 = \frac{1}{2\pi(\delta_1+1)}\left[-\theta_2\sin\phi + \ln r_2 \cos\phi\right]$$

$$f_3 = \frac{1}{2\pi(\delta_1+1)}\left[\sin\phi[(\delta_1+1)\theta_1 + \frac{2x_1y}{r_1^2}] + \cos\phi[(\delta_1-1)\ln r_1 - \frac{2x_1^2}{r_1^2}]\right]$$

$$g_1 = \frac{1}{2\pi(\delta_1+1)}\left[\sin\phi[\delta_1\ln r_2 + \frac{2x_2^2}{r_2^2} - 2c((3+\delta_1)\frac{x_2}{r_2^2} - \frac{4x_2^3}{r_2^4} - \frac{2c}{r_2^2} + \frac{4cx_2^2}{r_2^4})] + \cos\phi[\delta_1\theta_2 + \frac{2x_2y}{r_2^2} + 2c(\frac{-2y}{r_2^2} + \frac{(\delta_1+1)y}{r_2^2} - \frac{4x_2^2y}{r_2^4} + \frac{4cx_2y}{r_2^4})]\right]$$

$$g_2 = \frac{-1}{2\pi(\delta_1+1)}\left[\ln r_2 \sin\phi + \theta_2\cos\phi\right]$$

$$g_3 = \frac{1}{2\pi(\delta_1+1)}\left[\sin\phi[(1-\delta_1)\ln r_1 - \frac{2x_1^2}{r_1^2}] + \cos\phi[(\delta_1+1)\theta_1 - \frac{2x_1y}{r_1^2}]\right]$$

and ϕ is the dip of the slip plane (branch cut).

A free surface is crudely approximated by placing a second edge dislocation II parallel to dislocation I and on the slip plane of I. The burgers vector is negative that of I so that the slip is everywhere zero except on the planar surface between the two dislocations. The "free surface" is the horizontal plane midway between the two dislocations parallel to the boundary of regions 1 and 2. The displacements at the free surface due to this second dislocation are obtained by replacing x_1, x_2, y, r_1, r_2, and c in the expressions for f_i and g_i ($i = 1,2,3$) with x_1', x_2', y', r_1', r_2', and c' where

$$\begin{aligned} x_1' &= c - H \\ x_2' &= 3H - c \\ y' &= y - 2D\cot\phi \\ c' &= 2H - c \\ r_1' &= (x_1'^2 + y'^2)^{\frac{1}{2}} \\ r_2' &= (x_2'^2 + y'^2)^{\frac{1}{2}} \end{aligned} \qquad \text{(A-8)}$$

forming f_i' and g_i' ($i = 1,2,3$). The total x and y displacements at the free surface are then the sum of those for the two individual dislocations given by (A-6).

Viscoelastic Solution

The correspondence principle and Laplace transform are applied to obtain the time dependent deformation at the free surface when the lower half space, region 2, is replaced by a viscoelastic half space. The shear modulus μ_2 must be replaced by the operator

$$\bar{\mu}(s) = \frac{1}{2}\frac{b_0 + b_1 s}{a_0 + a_1 s}$$

where s is the transform variable and a_0, a_1, b_0, and b_1 are constants in the relation

$$(a_0 + a_1\frac{\partial}{\partial t})\sigma'_{ij} = (b_0 + b_1\frac{\partial}{\partial t})\varepsilon'_{ij} \qquad \text{(A-9)}$$

between the deviatoric shear stress σ'_{ij} and strain ε'_{ij} for a standard linear viscoelastic solid.

In addition, we choose the initial conditions that for the relaxation problem the slip Δu is a Heaviside step function in time. The Laplace transform of this condition is

$$\Delta\bar{u}(s) = \frac{\Delta u}{s}$$

Screw Dislocation

For the case of a screw dislocation with constant slip the expressions $\Delta\bar{u}(s)$ and $\bar{\mu}(s)$ are substituted into the elastic solutions, equations (A-4) and (A-5). Hence, the Laplace transforms of the surface displacement and shear stress are

$$\bar{u}_z(s) = \frac{1}{s}\left[\frac{\Delta u}{\pi}\tan^{-1}\left(\frac{y}{D}\right)\right] + \frac{\Delta u}{\pi}\sum_{n=1}^{\infty}\frac{1}{s}\left[\frac{\mu_1-\bar{\mu}(s)}{\mu_1+\mu(s)}\right]^n\left[\tan^{-1}\left(\frac{y}{2nH+D}\right) - \tan^{-1}\left(\frac{y}{2nH-D}\right)\right] \qquad \text{(A-10)}$$

$$\bar{\sigma}_{yz}(s) = \frac{1}{s}\left[\mu_1\frac{\Delta u}{\pi}\frac{D}{y^2+D^2}\right] + \mu_1\frac{\Delta u}{\pi}\sum_{n=1}^{\infty}\frac{1}{s}\left[\frac{\mu_1-\bar{\mu}(s)}{\mu_1+\mu(s)}\right]^n\left[\frac{2nH+D}{y^2+(2nH+D)^2} - \frac{2nH-D}{y^2+(2nH-D)^2}\right] \qquad \text{(A-11)}$$

Taking the inverse transform L^{-1} of equations (A-10) and (A-11) gives

$$u_z(t) = \frac{\Delta u}{\pi} \tan^{-1}\left(\frac{y}{D}\right) + \frac{\Delta u}{\pi} \sum_{n=1}^{\infty} \left[\tan^{-1}\left(\frac{y}{2nH+D}\right) - \tan^{-1}\left(\frac{y}{2nH-D}\right)\right] F_n(t) \quad t > 0 \qquad \text{(A-12)}$$

$$\sigma_{yz}(t) = \mu_1 \frac{\Delta u}{\pi} \frac{D}{y^2+D^2} + \mu_1 \frac{\Delta u}{\pi} \sum_{n=1}^{\infty} \left[\frac{2nH+D}{y^2+(2nH+D)^2} - \frac{2nH-D}{y^2+(2nH-D)^2}\right] F_n(t) \quad t > 0 \qquad \text{(A-13)}$$

where $F_n(t) = L^{-1}\left[\frac{1}{s}\left(\frac{\mu_1-\bar{\mu}(s)}{\mu_1+\mu(s)}\right)^n\right]$.

It is interesting to note that in equations (A-10) and (A-11) the fundamental time information is contained in $M = \frac{\bar{\mu}(s)-\mu_1}{\mu(s)+\mu_1}$. This is true since M is the only factor containing a modulus of the viscoelastic layer and therefore the only factor containing the transform variable s, except for the 1/s in the initial condition. This inherent separation of time dependence from geometry plus the linearity of the Laplace transform permit the expressions for displacement and shear stress to be obtained from a single evaluation of $F_n(t)$.

Skipping the details, $F_n(t)$ is found to be

$$F_n(t) = \left(\frac{pc}{d}\right)^n - p^n \sum_{k=1}^{n} \frac{n!}{(n-k)!k!}\left(\frac{c}{d}-1\right)^k e^{dt} \sum_{i=0}^{k-1} \frac{(-d\cdot t)^i}{(i)!} \qquad \text{(A-14)}$$

where

$$c = -\frac{2\mu_1 a_0 - b_0}{2\mu_1 a_1 - b_1}$$

$$d = -\frac{2\mu_1 a_0 + b_0}{2\mu_1 a_1 + b_1}$$

$$p = \frac{2\mu_1 a_1 - b_1}{2\mu_1 a_1 + b_1}.$$

Recall now equation (A-9) describing the viscoelastic material

$$a_0\sigma + a_1\dot{\sigma} = b_0\varepsilon + b_1\dot{\varepsilon}.$$

The relaxation function, i.e. the stress function in response to a unit step of displacement H(t) for such a material is (Fung, 1965)

$$\sigma(t) = \frac{b_0}{a_0}\left[1 - \left(1 - \frac{b_1}{b_0}\frac{a_0}{a_1}\right)e^{-t/\tau_\varepsilon}\right]H(t).$$

From this we see that at time t = 0+ the material can be characterized by an initial elastic shear modulus $\mu(0) = \frac{1}{2}b_1/a_1$ and at time infinity by a completely relaxed elastic shear modulus $\mu(\infty) = \frac{1}{2}b_0/a_0$. The characteristic decay time for this purely viscoelastic system is $\tau_\varepsilon = a_1/a_0$.

With this we can write

$$\frac{c}{d} = \frac{1 - \frac{\mu(\infty)}{\mu_1}}{1 - \frac{\mu(0)}{\mu_1}} \cdot \frac{1 + \frac{\mu(0)}{\mu_1}}{1 + \frac{\mu(\infty)}{\mu_1}}$$

$$P = \frac{1 - \frac{\mu(0)}{\mu_1}}{1 + \frac{\mu(0)}{\mu_1}}$$

$$d = -\frac{1}{\tau_\varepsilon}\frac{\left(1 + \frac{\mu(\infty)}{\mu_1}\right)}{\left(1 + \frac{\mu(0)}{\mu_1}\right)}$$

The relaxation time τ_ε can be further expressed in terms of the viscosity of the half space. The differential equation (A-9) describes the two independent mechanical models shown in figure 6. For model A, the relaxation time is given by

$$\tau_\varepsilon = \frac{\eta}{\mu(0)-\mu(\infty)}$$

where η is the viscosity. For model B we have the alternate expression

$$\tau_\varepsilon = \frac{\mu(0)-\mu(\infty)}{\mu^2(0)}$$

The constant d in the exponential time term can now be written as

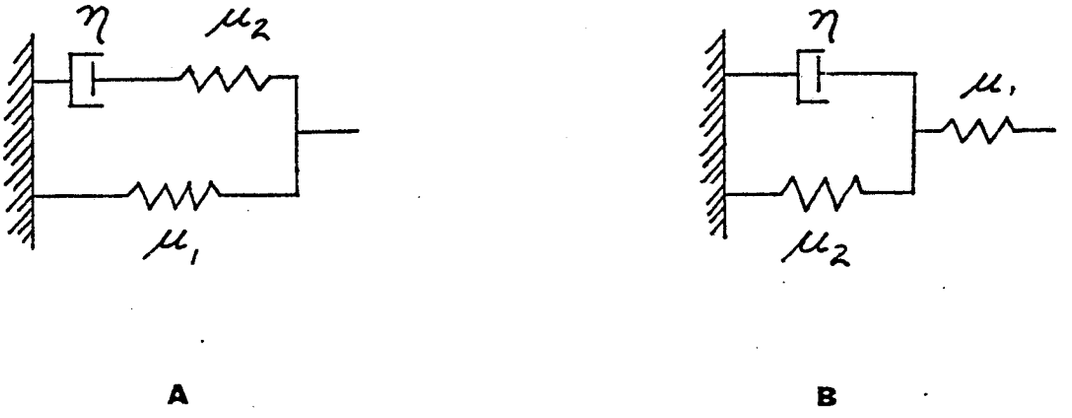

Figure 6. Two independent mechanical models described by the same form of differential equation (A-9).

$$d = -\frac{\mu_1}{\eta}\frac{(1-\frac{\mu(\infty)}{\mu(0)})}{\frac{\mu_1}{\mu(0)}}\frac{(\frac{\mu_1}{\mu(0)}+\frac{\mu(\infty)}{\mu(0)})}{(\frac{\mu_1}{\mu(0)}+1)} \qquad \text{model A}$$

or

$$d = -\frac{\mu_1}{\eta}\frac{\frac{\mu(0)}{\mu_1}}{(1-\frac{\mu(\infty)}{\mu(0)})}\frac{(\frac{\mu_1}{\mu(0)}+\frac{\mu(\infty)}{\mu(0)})}{(\frac{\mu_1}{\mu(0)}+1)} \qquad \text{model B} \qquad \text{(A-15)}$$

Thus, somewhat of an ambiguity exists in interpreting the constant d in terms of mechanical elements like viscosity, unless we know more about the viscoelastic material corresponding to equation (A-9). However, for a moderate range of relaxation, i.e. $2 < \frac{\mu(\infty)}{\mu(0)} < 0.8$, and $1 < \frac{\mu_1}{\mu(0)} < 2$ the expression for d in (A-15) can be summarized as

$$\frac{1}{d} \simeq -\alpha\frac{\eta}{\mu_1} \qquad \text{(A-16)}$$

where α is a numerical constant ($1 < \alpha < 10$) which depends on the values of $\mu(\infty)/\mu(0)$ and $\mu_1/\mu(0)$.

Edge Dislocation

For the edge dislocation with constant slip the expressions $\Delta\bar{u}(s)$ and $\bar{\mu}(s)$ are substituted into the elastic solutions, equation (A-6), yielding the Laplace transforms of the surface displacements

$$u_x(s) = \frac{\Delta u}{s}[\bar{A}(s)(f_1+f_1')+\bar{B}(s)(f_2+f_2')+(f_3+f_3')]$$

$$u_y(s) = \frac{\Delta u}{s}[\bar{A}(s)(g_1+g_1')+\bar{B}(s)(g_2+g_2')+(g_3+g_3')] \qquad \text{(A-16)}$$

where

$$\bar{A}(s) = (1-\bar{\mu}(s)/\mu_1)/(1+\delta_1\bar{\mu}(s)/\mu_1)$$

$$\bar{B}(s) = (\delta_2(s)-\delta_1\bar{\mu}(s)/\mu_1)/(\delta_2(s)+\bar{\mu}(s)/\mu_1)$$

$$\delta_2(s) = 3-4\nu_2(s) = 3-2(3K_2-2\bar{\mu}(s))/(3K_2+\bar{\mu}(s))$$

K_2 = the bulk modulus of region 2,

and f_i, f_i', g_i, and g_i' (i = 1,2,3) are as given earlier for the elastic

case. Taking the inverse transform gives

$$u_x(t) = \Delta u[A(t)(f_1+f_1')+B(t)(f_2+f_2')+(f_3+f_3')]$$

$$u_y(t) = \Delta u[A(t)(g_1+g_1')+B(t)(g_2+g_2')+(g_3+g_3')]$$

As in the screw dislocation problem there is again a separation of time dependence and geometry. Skipping the details we find

$$A(t) = L^{-1}\left(\frac{\bar{A}(s)}{s}\right) = \S\left[\frac{\beta}{\gamma} - \left(\frac{\beta}{\gamma} - 1\right)e^{-\gamma t}\right]$$

$$B(t) = L^{-1}\left(\frac{\bar{B}(s)}{s}\right) = \frac{f}{c} + \frac{ds_1^2+es_1+f}{3as_1^2+2bs_1+c}\, e^{s_1 t} + \frac{ds_2^2+es_2+f}{3as_2^2+2bs_2+c}\, e^{s_2 t} \qquad \text{(A-17)}$$

where

$$\S = (1-\mu(0)/\mu_1)/(1+\delta_1\mu_0/\mu_1)$$

$$\frac{\beta}{\gamma} = \frac{(1-\mu(\infty)/\mu_1)/(1-\mu(0)/\mu_1)}{(1+\delta_1\mu(\infty)/\mu_1)/(1+\delta_1\mu(0)/\mu_1)}$$

$$\gamma = (1+\delta_1\mu(\infty)/\mu_1)/[(1+\delta_1\mu(0)/\mu_1)\tau_\varepsilon]$$

$$a = (3+\mu(0)/\mu_1)(1+3K_2/\mu(0))-4(3K_2/2\mu(0)-1)$$

$$b = [(3+\mu(\infty)/\mu_1)(1+3K_2/\mu(0))-4(3K_2/2\mu(0)-1)]/\tau_\varepsilon + [(3+\mu(0)/\mu_1)(1+3K_2/\mu(\infty))-4(3K_2/2\mu(\infty)-1)]/\tau_\sigma$$

$$c = [(3+\mu(\infty)/\mu_1)(1+3K_2/\mu(\infty))-4(3K_2/2\mu(\infty)-1)]/(\tau_\varepsilon\tau_\sigma)$$

$$d = (3-\delta_1\mu(0)/\mu_1)(1+3K_2/\mu(0))-4(3K_2/2\mu(0)-1)$$

$$e = [(3-\delta_1\mu(\infty)/\mu_1)(1+3K_2/2\mu(0))-4(3K_2/\mu(0)-1)]/\tau_\varepsilon + [(3-\delta_1\mu(0)/\mu_1)(1+3K_2/\mu(\infty))-4(3K_2/2\mu(\infty)-1)]/\tau_\sigma$$

$$f = [(3-\delta_1\mu(\infty)/\mu_1)(1+3K_2/\mu(\infty))-4(3K_2/2\mu(\infty)-1)]/(\tau_\varepsilon\tau_\sigma)$$

$$s_1 = [-b+(b^2-4ac)^{\frac{1}{2}}]/2a$$

$$s_2 = [-b-(b^2-4ac)^{\frac{1}{2}}]/2a$$

References

Chinnery, M.A. and D.B. Jovanovich, Effect of earth layering on earthquake displacement field, Bull Seis. Soc. Am., 62, 6, 1629-1639, 1972.

Chou, Y.T., Screw dislocations in and near lamellar inclusions, Report No. 126, Bain Laboratory, U.S. Steel Research Center, Monroeville, Pa., 1966.

Crittenden, M.D., Jr., Effective viscosity of the earth derived from isostatic loading of Pleistocene Lake Bonneville, J. Geophys. Res., 68, 5517-5530, 1963.

Fung, Y.C., Foundations of Solid Mechanics, Prentice-Hall, Inc., Englewood Cliffs, N. J., 1965.

Kanamori, H., Mode of strain release associated with major earthquakes in Japan, in Annual Review of Earth and Planetary Sciences, vol. 1, edited by F.A. Donath, F.G. Stehli, and G.W. Wetherill, Annual Reviews, Palo Alto, Ca., 1973.

Lee, M-S and J Dundurs, Edge dislocation in a surface layer, Int. Jour. of Eng. Science, 11, 87-94, 1973

Mura, T, The continuum theory of dislocations, in Advances in Materials Research vol. 3, edited by H. Herman, John Wiley and Sons, New York, 1968.

Rybicki,K.,The elastic residual field of a very long strike-slip fault in the presence of a discontinuity, Bull. Seism Soc. Am., 61, 1, 79-92, 1971.

Walcott, R.I., Structure of the earth from glacio-isostatic rebound, in Annual review of Earth and Planetary Sciences, vol. 1, edited by

F.A. Donath, F.G. Stehli, and G.W. Wetherill, Annual Reviews, Palo Alto, Ca., 1973.

CHAPTER 3

MELT SQUIRT IN THE ASTHENOSPHERE

In Chapter 2 we have proposed a simple fault model to explain postseismic deformation accompanying major earthquakes that break through a large fraction of the lithosphere. In our model the source of deformation is viscous relaxation in the asthenosphere. We now extend the study and some observations to say something about actual materials that might be found in the upper mantle and that can produce the observed relaxation.

Figure 1 shows examples of upheaval observed as a function of time at four tide stations following the 1946 Nankaido earthquake. The important point to note for this study is that the characteristic time of relaxation is 3 to 5 years. The transient deformation given by our model, though not a pure decaying exponential, was found to be characterized by a time constant τ given by

$$\tau = \alpha \frac{\eta}{\mu}$$

η is a viscosity of the asthenosphere, and μ is the lithospheric rigidity. The constant α is a strong function of the initial and relaxed shear moduli of the viscoelastic material, which in our model is a standard linear solid. The observations at Nankaido suggest a relaxed shear modulus of about 0.4 to 0.6 times the initial shear modulus. This puts α between about 1 and 10 and gives an effective viscosity of 10^{19} to 10^{20} poise.

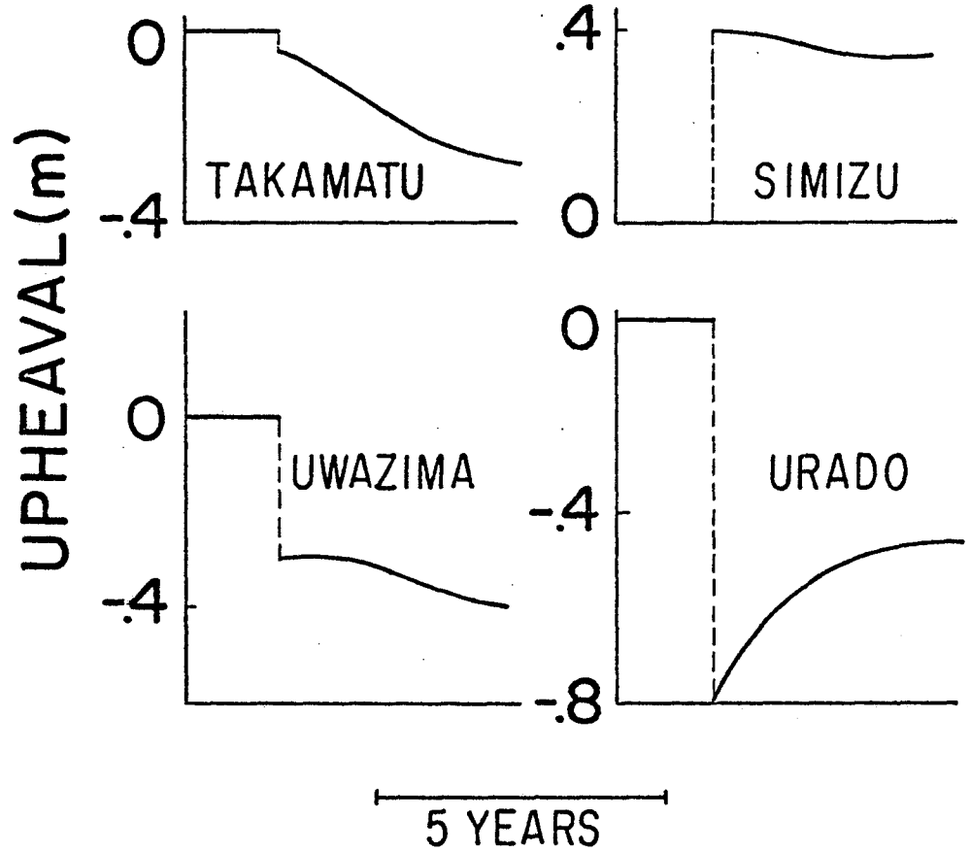

Figure 1. Observed upheaval as a function of time at four tide stations on Shikoku Island, Japan. Dashed lines represent upheaval at the time of the 1946 Nankaido earthquake (after Matuzawa, 1964).

We concluded that the observed postseismic deformation at Nankaido is due to viscous relaxation in the upper mantle. However, the range of viscosities obtained says little about the actual physical mechanisms causing the relaxation.

Partial Melt Mechanisms

The two dimensional model suggests that the spatial extent of largest deformation, particularly at the surface, is roughly proportional to the depth of faulting. At Nankaido the characteristic wavelength of surface deformation is about 50 to 100 km. We expect, then, that the major deformation is confined to within a few wavelengths of the surface--say 100 km or so. If the lithosphere in this area has a thickness of 70 km or less, with a shallow low velocity zone (Kanamori, 1971), then we expect most of the viscous deformation to take place within the low velocity zone.

Seismic, heat flow and volcanic evidence indicate that portions of the upper mantle--in particular, the low velocity zone--may be partially molten (e.g. Anderson and Sammis, 1970; Kanamori, 1970). This suggests, then, that we investigate materials with up to a few percent melt.

Consider, in general, rock systems consisting of pockets of a fluid (melt) enclosed in a matrix of solid rock. To a sufficient approximation the melt can be characterized by a Newtonian viscosity, given by the ratio of shear stress to shear strain rate. In addition, at mantle temperatures the solid material itself might exhibit creep or relaxation in shear. Whether or not the solid has a linear stress-strain rate law depends upon the dominant solid creep mechanism (e.g.

Weertman, 1970; Gordon, 1965). In either case, an effective viscosity can be assigned to the solid, which may or may not be a function of the shear stress.

When a strain field is very quickly applied, the initial response of the system, as a whole, is essentially elastic, roughly describable by a set of instantaneous (i.e. unrelaxed or high frequency) elastic moduli. However, the "viscous" elements in both the liquid and solid phases immediately begin to relax, with time constants proportional to the effective viscosities. For shear stresses on the order of tens of bars or less (as expected at Nankaido) Gordon (1965) and Weertman (1970) predict solid effective viscosities typically much greater than 10^{16} poise. However, the viscosities given by Clark (1966) for melts are generally much less than 10^{12} poise. We expect, then, that when both solid and melt are present the melt will relax much more quickly than the solid, and that on the time scale of fluid relaxation, the solid can be treated as essentially elastic.

By what specific mechanisms, then, can the presence of melt cause relaxation on the time scale observed following the Nankaido earthquake? There are two obvious possibilities. The first is a large-scale viscous flow or diffusion of melt through the porous, solid matrix. The second, is simple shear relaxation within individual pockets of melt.

Flow in Porous Media

Consider first the case of regional flow of the melt phase over large distances. The melt, occurring on grain faces and edges, might form a continuous film throughout the consequently porous mantle rock. As shown in figure 2, the abrupt thrusting of the earthquake causes

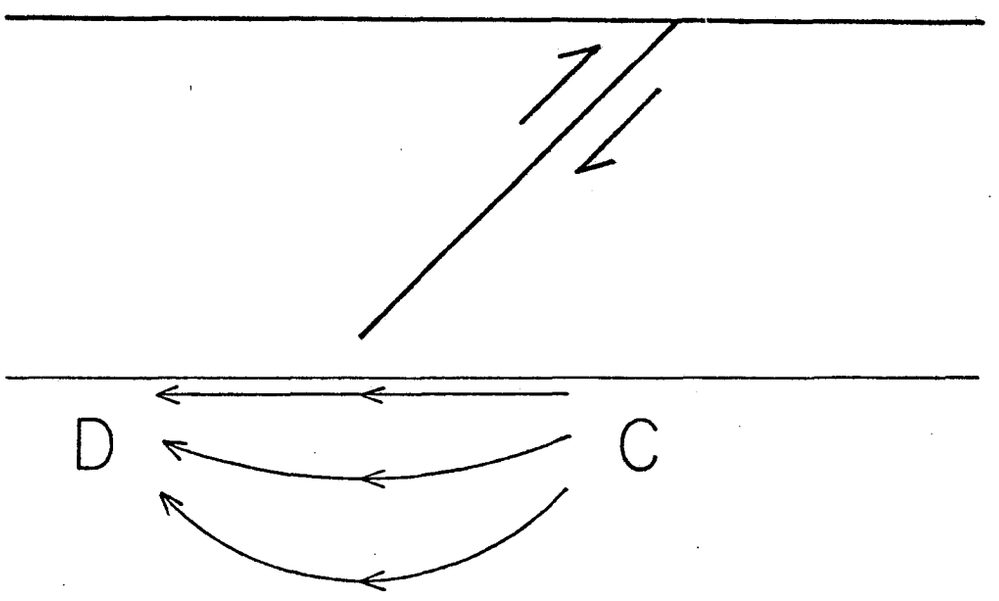

Figure 2. Regional flow. Abrupt thrusting of an earthquake causes regions of compression C and dilation D. As a result viscous fluid in the porous half space diffuses from C toward D.

a region of relative compression (C) and one of relative dilation (D). The solid-melt system has an initial compressibility that depends on the separate compressibilities of the solid and melt phases and on the fraction of melt present. To an extent the pore pressure of the melt resists compression of the system. But, as the melt flows or diffuses away from the region of compression, the pores collapse, the effective compressibility increases, and the system appears to relax. With this model the decay time, neglecting chemical and further melting effects, is simply the liquid diffusion time (e.g. Nur and Booker, 1972) given by

$$\tau = L^2\eta\beta/4k' \qquad (2)$$

where L is a characteristic length, η is the melt viscosity, β is the effective compressibility, and k' is the intrinsic permeability. In laboratory measurements rocks with as much as 10 percent porosity seldom have permeabilities greater than 100 millidarcys (md). Therefore, for the rocks considered here, with only a few percent melt, 100 md should be a high estimate for permeability. Using melt viscosities of 10^3 to 10^{12} poise (Clark, 1966) and a length scale appropriate for Nankaido of 50 km, the time constant comes out to be 10^3 to 10^{15} years--3 to 15 orders of magnitude larger than the observed time. Hence, regional flow of melt such as this is much too slow to account for the observed postseismic deformation.

Shear Relaxation

Consider next the melt on grain faces to be in the form of discrete, unconnected inclusions within the solid matrix, as suggested, for example, by Walsh and shown schematically in figure 3. In this case

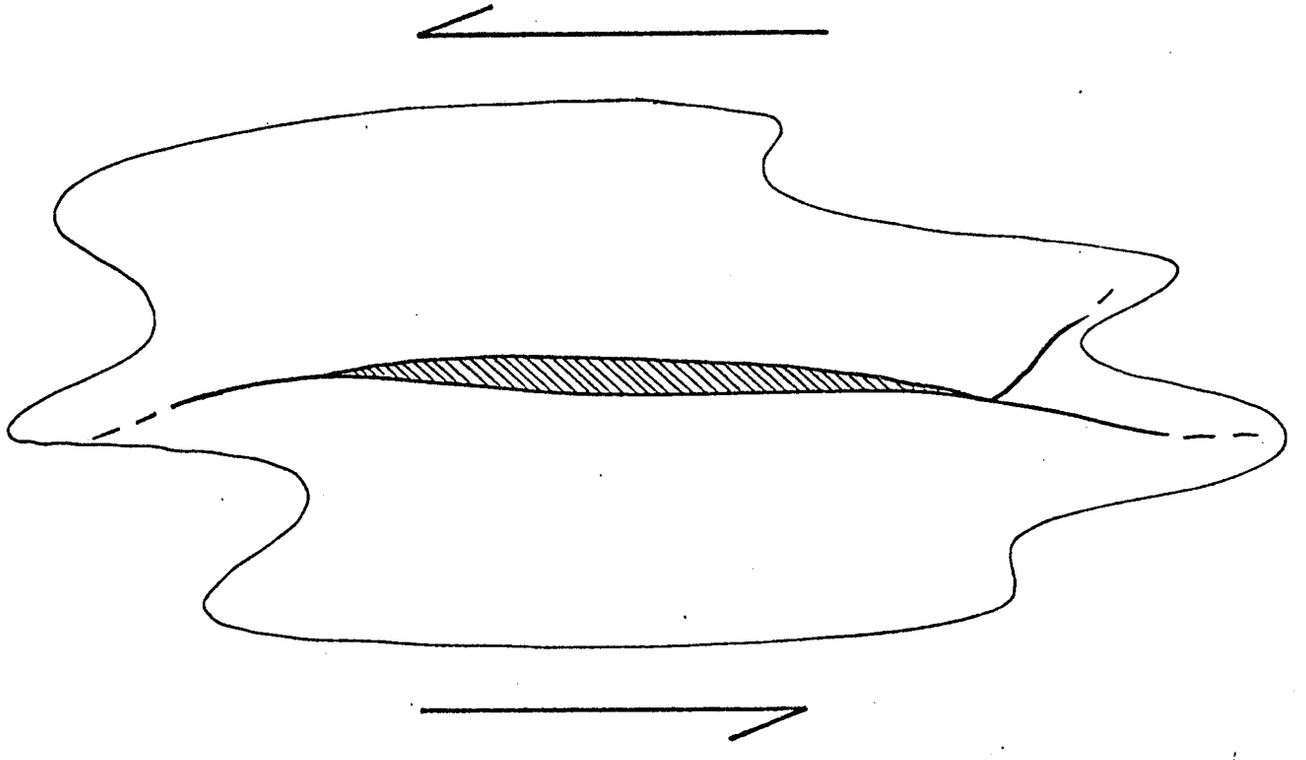

Figure 3. Viscous cracks. Viscous shear flow within flat, "penny shaped" pockets of melt relaxes components of shear stress parallel to the plane of the crack.

the relaxation mechanism is simple shearing within the weak viscous pockets--not really a flow. Walsh (1969) has solved for the mechanical response to sinusoidal oscillations of such a system consisting of flat ellipsoidal or "penny-shaped" viscous pockets within an otherwise elastic solid. His results yield, for the composite, an effective bulk modulus approximately equal to the bulk modulus of the solid. However, the effective rigidity is dramatically reduced by the viscous inclusions and is strongly dependent on viscosity and frequency.

Nur (1971) has shown that low porosity fluid saturated rocks in the laboratory do behave as predicted by the Walsh theory for viscosities ranging over 13 orders of magnitude. Comparing the theoretical results with actual seismic attenuation and velocity data, Solomon (1972) infers a value of 10^8 poise and Nur (1971), a range of 10^6 to 10^{12} poise for the viscosity of melt in the low velocity zone over North America.

In an analogous way to Walsh we solved for the quasi-static relaxation of the same system. The effective shear modulus of an elastic matrix with elastic penny-shaped inclusions is given by Walsh (1969). The shear stress σ and shear strain ε of the elastic inclusion are related by

$$\sigma = 2\mu\varepsilon \tag{3}$$

where μ is the elastic shear modulus. If, on the other hand, the inclusions are viscous then the stress-strain law is

$$\sigma = 2\eta \frac{\partial \varepsilon}{\partial t} \tag{4}$$

where η is the viscosity. Taking the Laplace transform of (4) gives

$$\bar{\sigma} = 2(\eta s)\varepsilon \tag{5}$$

where s is the Laplace transform variable. Comparing (4) and (5) we see that the transformed viscous problem is identical to the elastic problem if the shear modulus is replaced by the operator (ηs). Hence, we take Walsh's expression for the effective shear modulus of the elastic composite and everywhere replace the shear modulus of the inclusions by ηs. This gives the transformed Laplace operator $\bar{\mu}(s)$ corresponding to the effective modulus of the viscous-elastic composite. Assuming that the relaxation time τ will satisfy the condition

$$\tau > \frac{\eta}{\mu_1} \tag{6}$$

where η is the melt viscosity and μ_1 is the matrix rigidity, the effective transformed modulus $\bar{\mu}(s)$ can be written as

$$\bar{\mu}(s) = \frac{5(\eta s + a\mu_1)}{5\frac{\eta s}{\mu_1}(2c+5a)} \tag{7}$$

where c is the melt concentration. The constant a is given by

$$a = \frac{3\pi\alpha}{4}\frac{3k_1+2\mu_1}{3k_1+4\mu_1} \tag{8}$$

where k_1 and μ_1 are the bulk and shear moduli respectively of the matrix and α is the ratio of minor axis to major axis of the ellipsoidal inclusion. A step function in strain, then, results in a relaxation time τ of

$$\tau = \frac{\eta}{\mu_1}\frac{5}{2c+5a} \tag{9}$$

If we consider the concentration range $10^{-1} < c < 10^{-6}$, aspect ratio $10^{-1} < \alpha < 10^{-6}$, and shear modulus $\mu_1 \simeq 10^6$ bar (which include the values used by Nur (1971) and Solomon (1972) to explain seismic data) and use the decay time for Nankaido, this gives melt with viscosities of 10^{14} to 10^{19} poise. This is about 6 to 11 orders of

greater than the viscosities found in Solomon's analysis and is much higher than we expect for magma (Clark, 1966).

This indicates that simple shear relaxation in flat pockets, while consistent with losses on a seismic time scale, is much too rapid to account for the longer postseismic relaxation.

Melt Squirt

The two mechanisms just considered give wide bounds on the relaxation times possible from partially melted rock, but fail to account for postseismic deformation lasting only a few years. Long distance flow can decay over periods approaching the age of the earth, while the Walsh-type flat viscous cracks relax in shear on a seismic time scale. Clearly the 3 to 5 year recovery at Nankaido lies between these two cases. We need to find a reasonable intermediate model--one that can account for a seismic attenuation and low velocity zone, and that can subsequently relax on a time scale of several years.

Such a model is shown schematically in figure 4. Two or more flat inclusions of melt, oriented in different directions, are connected. This could correspond to melt on two adjacent faces of a single grain, giving a crack length equal to a grain diameter or less—or the melt might be a continuous film over many grains.

Two widely separately time constants are possible. Components of shear stress oriented parallel to the flat cracks relax quickly, on a seismic time scale, by simple shearing of the melt. In this sense the model is identical to the flat viscous cracks described by Walsh. However, cracks oriented parallel to the principal stresses as shown in figure 5 behave quite differently. Melt squirts out of

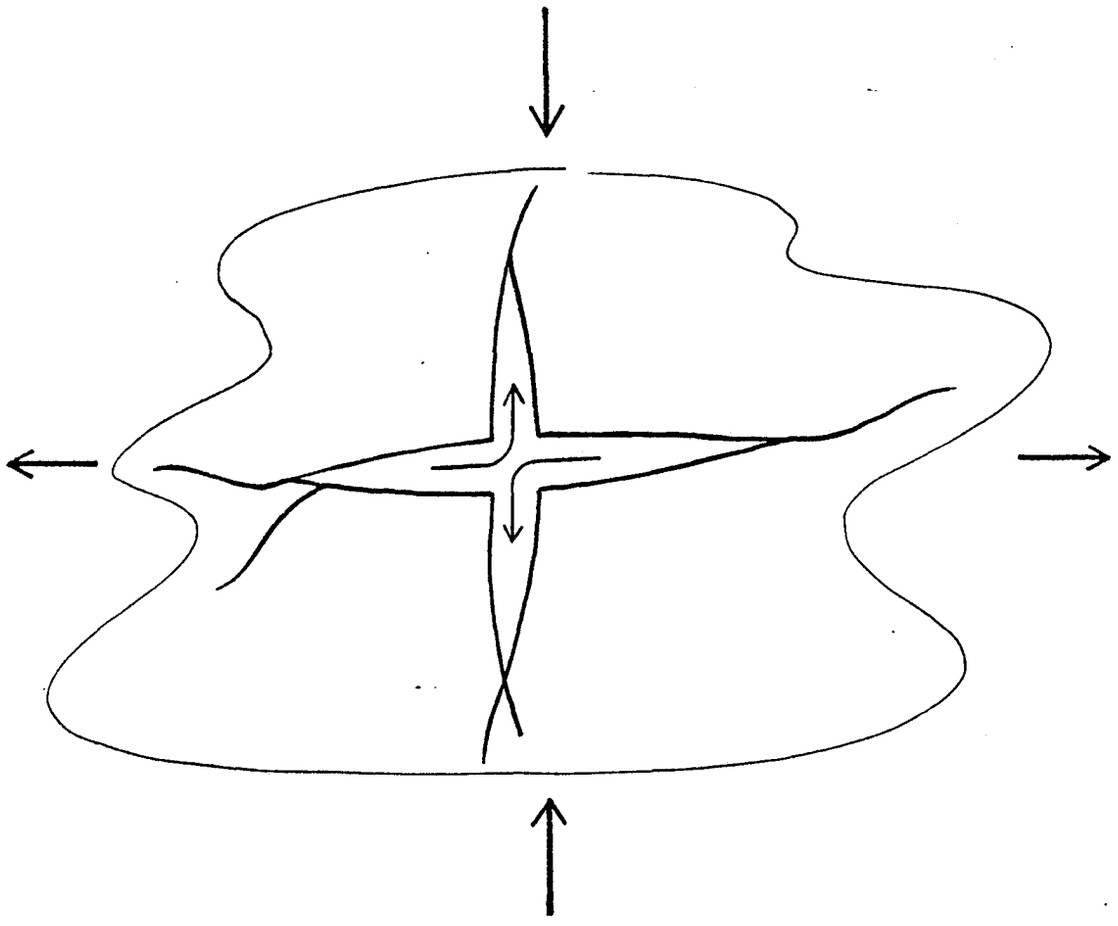

Figure 4. Melt squirt. When two or more cracks at different orientations are connected, applied stress can cause melt to flow from one crack to another.

the horizontal crack, which lies normal to the greatest compression, and into the vertical crack, which is normal to the least compression. In this case actual flow is required between cracks with a relaxation time much longer than for the simple shear relaxation. The length of the flow path is, however, very short compared to the regional flow, so that this process is much faster.

Recognizing that this is an extreme case of fluid diffusion in a porous solid, the flow time constant can again be estimated from (2):

$$\tau = \frac{L^2 \eta \beta}{4k'}$$

Since melt is assumed to form on grain faces, an estimate of permeability can be obtained from flow between parallel plates. The permeability of a unit area channel between plates with separation h is proportional to h^2. An isotropic rock with porosity c has an area fraction of pores on any plane also equal to c, with an average of one-third of the pore "channels" aligned in any given direction. This gives a rock permeability of

$$k' = \frac{c}{3} \cdot h^2 \tag{10}$$

Since the actual flow channels are tortuous and irregular, and not all pores are connected, this is probably an upper limit. Finally, since $\alpha = h/L$, the relaxation time is

$$\tau \simeq \frac{\eta \beta}{\alpha^2 c} \tag{11}$$

Because this model also responds as the Walsh viscous cracks, the same parameters that successfully explain seismic data should also account for the postseismic time scale. Nur (1971) suggests values of $\eta \simeq 10^7$ poise, $\alpha = 10^{-5}$ and $c = 10^{-4}$ for a good fit to seismic data

for the low velocity zone. These give a postseismic relaxation time of $\tau = 10^9$ sec. Solomon (1972) proposes two layers to fit two observed seismic attenuation peaks with $c = 10^{-2}$, $\eta = 10^8$ poise and $\alpha = 10^{-2}$, 10^{-5}. In the relaxation model these give characteristic times of 10^2 sec and 10^8 sec. The 10^2 sec relaxation process would be part of the long period seismic signal indistinguishable from the seismic displacements.

The computed decay times of 10^8 to 10^9 sec agree remarkably well with the 10^8 relaxation time observed at Nankaido. Although the estimate of permeability (10) is high, the Nankaido area appears to have a larger concentration of melt than the average low velocity zone represented by the seismic data from which the values for α and c were obtained. Velocity and attenuation studies (Aki, 1968; Kanamori, 1970) indicate as much as 2 percent soft or melted material and an extremely low Q (80) beneath parts of Japan, whereas Solomon (1972) and Nur (1971) found only 10^{-2} to 1 percent melt. Therefore we conclude that this model provides a reasonable mechanism to account for the transient deformation at Nankaido as well as seismic attenuation in the low velocity zone.

Conclusion

The interpretation of the seismic low velocity zone as a region of partially molten rock is now widely accepted. The existence of partially molten rock explains the occurrence of basaltic volcanism, serves as a mechanically soft zone for plate tectonics, and is also generally consistent with observed low Q and large negative gradients of velocity with depth. It is therefore logical that we consider the

same region as a zone of relaxation responsible for transient deformation following large earthquakes on plate boundaries.

Table 1 summarizes the results of three partial melt models that were examined to explain the 3 to 5 year relaxation time of deformation following the 1946 Nankaido earthquake. Simple shear relaxation in flat viscous cracks takes place on the order of seconds and is much too rapid; regional flow over tens of kilometers takes thousands to billions of years and is much too slow. But the squirt of melt between pockets on the order of a grain size combines simple viscous shearing with very short distance diffusion for periods on the order of years. It is extremely fortunate that the relaxation time constants for the three models are so different, allowing a clear distinction between them.

We conclude that if a molten phase is present then a reasonable mechanism for transient deformation in the upper mantle is small scale flow of partial melt as illustrated by the melt squirt model. The presence of the viscous fluid broadens the relaxation spectrum so that two widely separated types of time constants are possible. Simple shear relaxation parallel to cracks happens very quickly, on a seismic time scale. This is exactly the behavior described by Walsh's theory for flat viscous cracks. On the other hand, melt squirt, or flow from cracks of one orientation to another, is much slower. The same values of viscosity, aspect ratio and concentration needed to explain seismic attenuation and velocity data with the Walsh theory are also compatible with the Nankaido data using the melt squirt model.

MECHANISM	VISCOUS CRACKS	REGIONAL FLOW	MELT SQUIRT
RELAXATION TIME	10^{-2}–10^{3} sec	$>10^{3}$ yr	3–5 yr
CONCLUSION	TOO FAST	TOO SLOW	OK

Table 1. Relaxation with melt phase. Melt squirt can explain time scale of postseismic deformation. Simple shearing in flat cracks is too fast; large scale flow is too slow.

References

Aki, K., Seismological evidences for the existence of soft thin layers in the upper mantle under Japan, J. Geophys. Res., 73(2), 585-594, 1968.

Anderson, D.L. and C. Sammis, Partial melting in the upper mantle, Phys. Earth Planet. Interiors, 3, 41-50, 1970.

Clark, S.P., Jr., ed., Handbook of Physical Constants, Geological Soc. of Amer., Inc., New York, 1966.

Gordon, R.B., Diffusion creep in the earth's mantle, J. Geophys. Res., 70, (10), 2413-2418, 1965.

Kanamori, H., Mantle beneath the Japanese arc, Phys. Earth Planet. Interiors, 3, 475-483, 1970.

Kanamori, H., Great earthquakes at island arcs and the lithosphere, Tectonophysics, 12, 187-198, 1971.

Matuzawa, T., Study of Earthquakes, Uno Shoten, Tokyo, Japan, 1964.

Nur, A., Viscous phase in rocks and the low-velocity zone, J. Geophys. Res., 75(5), 1270-1277, 1971.

Nur, A and J. Booker, Aftershocks caused by pore fluid flow?, Science, 175, 885-887, 1972.

Solomon, S.C., Seismic-wave attenuation and partial melting in the upper mantle of North America, J. Geophys. Res., 77(8), 1483-1502, 1972.

Walsh, J.B., A new analysis of attenuation in partially melted rock, J. Geophys. Res., 74, 4333, 1969.

Weertman, J., The creep strength of the earth's mantle, Reviews of Geophysics and Space Physics, 8(1), 145, 1970.

CHAPTER 4

THE MECHANICS OF STRAIN ACCUMULATION AND RELEASE ON A STRIKE-SLIP FAULT

Mechanical models for various aspects of strain accumulation and release on the San Andreas fault have been presented by a number of authors (e.g. Scholz and Fitch, 1969; Savage and Burford, 1970; Turcotte and Spence, 1974; Rundle and Jackson, 1976). However, despite their common simplicity, the models predict fundamentally different rates and scales of strain accumulation, because of ad hoc model assumptions made in lieu of reliable data.

In order to resolve some of these differences we examine the basic mechanics of an earthquake cycle on a strike-slip system. The goal is not to develop a particular model of plate interaction but to see how much we can learn with the fewest model assumptions. In the first section to follow we derive an expression for the mean stress on a two-dimensional fault in terms of the total slip on the fault and the boundary conditions far away. The main features of strain change during an earthquake cycle are discussed for both stress and displacement boundary conditions. In the next sections the results are extended to three dimensions and are used to evaluate some published models of strain accumulation along the San Andreas fault. Finally some simple relations between slip rate and strain rate are discussed with respect to observed creep on the San Andreas.

To begin, we approximate the lithosphere in the region of the fault as a linear elastic slab as shown in figure 1. Elastic behavior over time scales up to at least several major earthquake recurrence times (10^2 to 10^4 years) is consistent with analyses of glacial rebound and lithospheric flexure (Walcott, 1973) as well as our intuitive concept of plate tectonics. However, localized deviations from linear elasticity may occur in the shallow crust due to dilatancy or pore fluid flow.

The upper plate surface is stress-free. On the lower surface we assume rate-dependent viscous shear tractions that are negligibly small during much of the earthquake cycle, but which may be substantial during episodes of rapid strain release.

There are many sources of stress in the lithosphere (e.g. Turcotte and Oxburgh, 1973). Driving mechanisms include a gravitational push at ocean ridges and a pull at subduction zones. In addition asthenospheric tractions integrated over the entire plate area might contribute a net drive or drag on the plate even though we have assumed small tractions locally. Other sources accounting for stress gradients within the lithosphere, though not necessarily providing a net drive or drag include membrane stress, thermal stress and overburden stresses. For the system in figure 1 we assume that the net effect of the distant driving force is to apply a nearly uniform shear stress $\sigma_{yz} = \sigma_0$. At the fault plane, $y = 0$, the shear stress σ_{yz} can vary significantly with x and z resulting from variations in fault displacement and frictional resistance stresses. However, for a system in equilibrium the mean of σ_{zy} at $y = 0$ must equal σ_0 during periods when the viscous shear tractions from below are negligible.

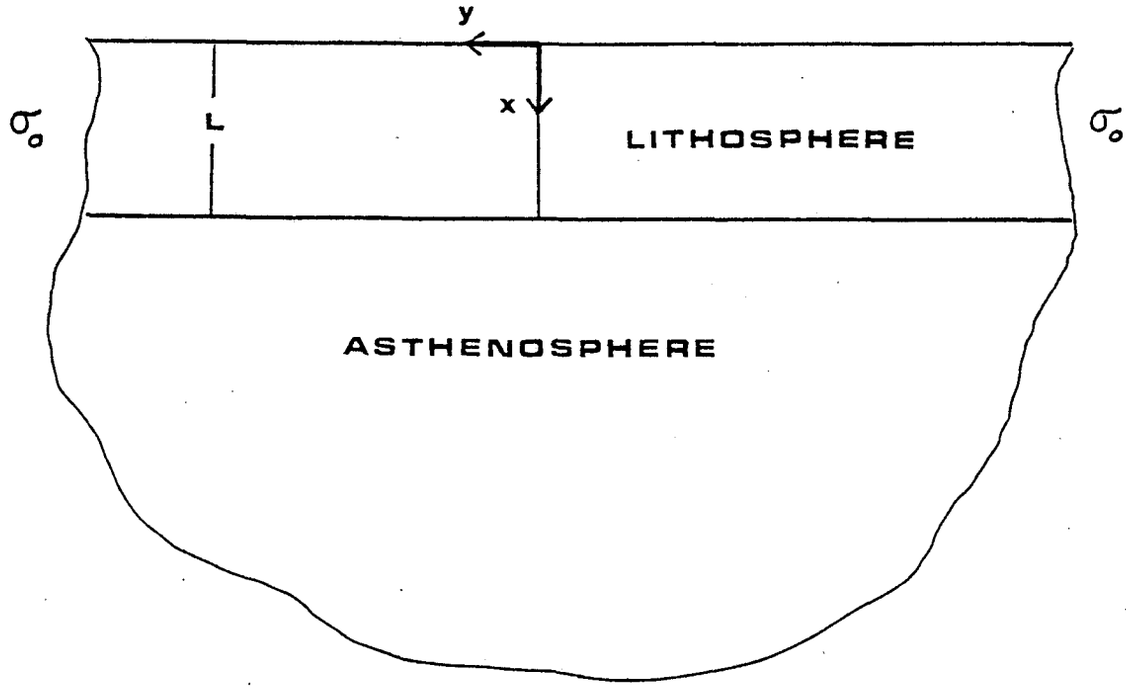

Figure 1. Simple mechanical model of the earth's crust and upper mantle suggested by plate tectonics and isostatic rebound: A relatively elastic lithosphere over a weaker ductile asthenosphere.

In two dimensions, assuming no variation with z, the equilibrium of stresses can be written simply as

$$\frac{1}{L}\int_0^L \sigma_{zy}dx = \sigma_0 \qquad (1)$$

along any vertical section of the plate. At distances from the fault greater than L, the variations in σ_{zy} about the mean die out by Saint-Venant's principle so that $\sigma_{zy}(x) \simeq \sigma_0$. Shorter wavelength variations of σ_{zy} on the fault will die out even faster.

Boundary Conditions in the Two-Dimensional Problem

To investigate the boundary conditions in the two dimensional system we can use the Betti-Rayleigh reciprocity theorem to find a relation between the applied stress σ_0 at $|y| > L$, the displacement $U(x,y)$ at $|y| > L$ and the fault slip $\Delta u(x) = U(x,0^+) - U(x,0^-)$. The theorem states that for a body acted upon separately by two sets of tractions, the work done by the first set of tractions acting through the displacements produced by the second set of tractions is equal to the work done by the second set of tractions acting through the displacements due to the first set of tractions. To apply the theorem consider the two sets of tractions shown in figure 2. The system on the left is loaded at the sides by uniform stresses σ_0 and on the fault faces by variable resistance stresses $\sigma_f(x)$. The resulting displacements are the relative slip $\Delta u(x)$ on the fault and a fairly uniform displacement $\pm U_0$ at the sides. The system on the right has identical stresses σ_0 applied to both the sides and the fault faces, resulting in $U(x) = 0$ on the fault and $\pm U_0'$ at sides. Applying the theorem we can write

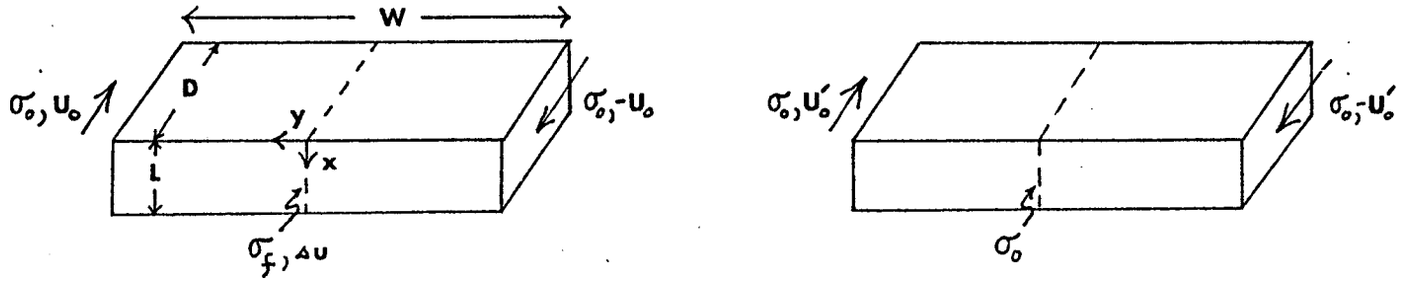

Figure 2. Applying the reciprocity theorem to an elastic plate in shear. On the left only the fault strength σ_f is applied to the fault face, resulting in some fault slip. On the right the laterally applied shear σ_o is also applied to the fault to prevent slip.

$$2\sigma_0 U_0 \dot{L}D - \sigma_0 D\int_0^L \Delta u(x)dx = 2\sigma_0 U_d \dot{L}D \qquad (2)$$

By noting that $2U_d = W\sigma_0/\mu$ where μ is the plate shear modulus we can rearrange (2):

$$W\frac{\sigma_0}{\mu} = 2U_0 - \frac{1}{L}\int_0^L \Delta u(x)dx \qquad (3)$$

Defining $\Delta U_0 = 2U_0$ and $\Delta\bar{u} = \frac{1}{L}\int_0^L \Delta u dx$, (3) becomes

$$\sigma_0 = \frac{\mu}{W}(\Delta U_0 - \Delta\bar{u}) \qquad (4)$$

Equation (4) is an extremely simple relation between the relative plate displacement at $y = \pm W$, the average fault slip $\Delta\bar{u}$ and the mean or applied stress σ_0. Nothing has been assumed about fault material properties or the details of seismic or aseismic creep. Differentiating with respect to time we obtain:

$$\dot{\sigma}_0 = \frac{\mu}{W}(\Delta\dot{U}_0 - \dot{\Delta\bar{u}}) \qquad (5)$$

The simple interpretation of (5) is that if the gross plate speed $\Delta\dot{U}_0$ exceeds the fault slip rate $\dot{\Delta\bar{u}}$ because of frictional resistance or locked portions of the fault, then the mean stress in the plate grows. The mean stress is relieved when the fault slip rate $\dot{\Delta\bar{u}}$ exceeds $\Delta\dot{U}_0$.

To find the effect of different boundary conditions we can apply equations (4) and (5) to a hypothetical major earthquake cycle. Figure 3 shows schematically strain accumulation and release with a constant stress boundary condition. We pick as a reference state a point in time after a major earthquake and any resulting postseismic relaxation, as represented in figure 3a. We assume nothing about the distribution of stress or slip on the fault at this time other than the mean stress must equal σ_0 because of the constant stress boundary

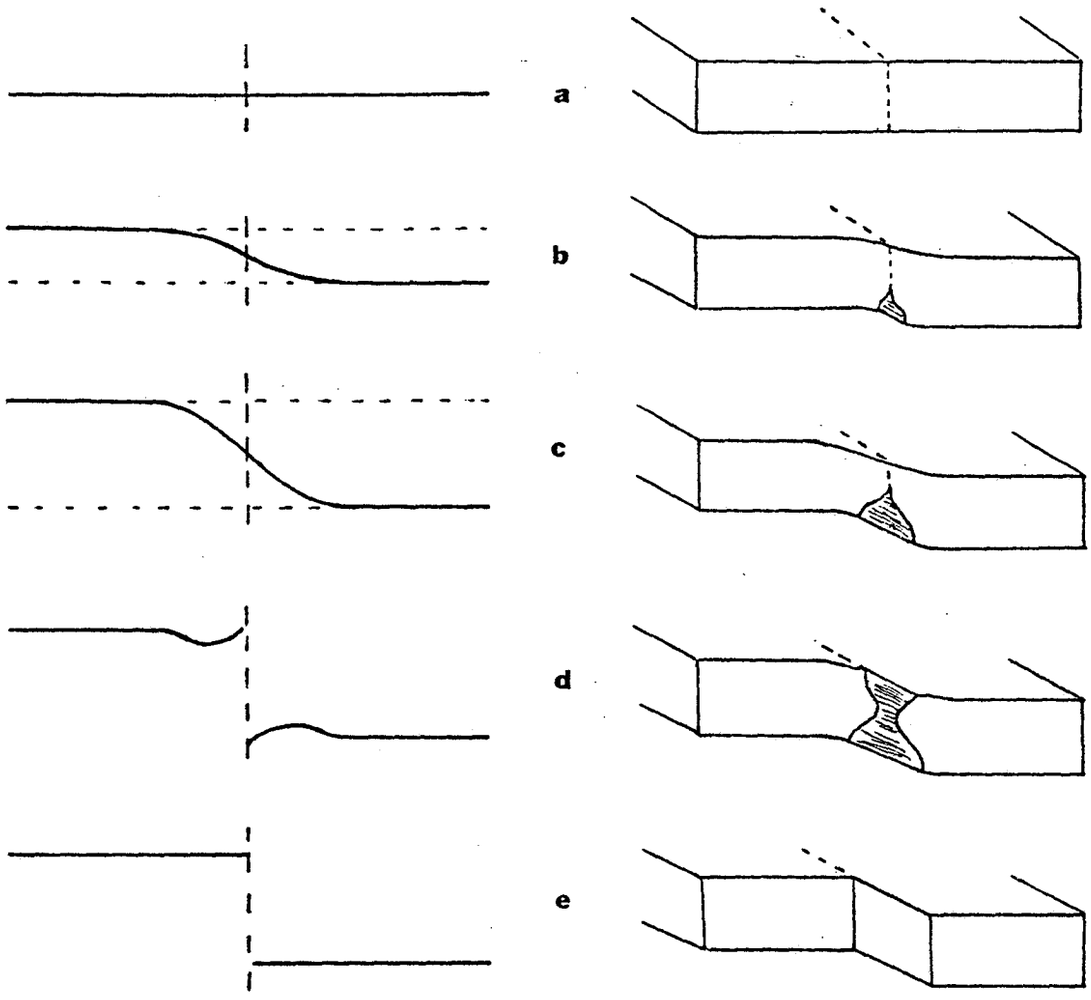

Figure 3. A hypothetical earthquake cycle with constant stress boundary conditions. Fault slip is shown schematically on the right. Corresponding surface displacement is on the left.

condition. If aseismic fault slip takes place somewhere below the surface (presumably below the brittle seismic layer in California), surface strain accumulates as shown in 3b. The width of the zone of strain accumulation along the fault is approximately the depth of the slip zone. The change in slope of the reference line at the fault trace is exactly twice the change in shear strain ε_{yz} at the surface. Although the mean stress remains fixed, the local stress is generally relieved in the slipped regions and concentrated elsewhere on the fault. Hence the stress at the fault trace is increased by $\sigma_{yz} = 2\mu\varepsilon_{yz}$. Below the surface little can be said about the details of the stress concentration unless the shape of the slip is known. However, since stress tends to be largest at the tips of slip zones, the surface stress is probably not the maximum stress.

Outside the zone of strain accumulation the stress deviations die out, and the reference line flattens reflecting the constant stress σ_0. The net offset of the reference line represents rigid block displacement of the two plates outside the zone of strain accumulation. From equation (4) we see that if σ_0 stays constant, any increment of plate displacement ΔU_0 must be exactly equal to the average fault slip $\Delta\bar{u}$. Hence the reference line offset equals the net fault slip that has occurred since the reference state.

As the buried slip continues to grow the net plate offset and the near-surface stress on the fault will also grow, as in 3c. The width of the zone of strain accumulation may increase or decrease depending on the depth of slip.

If a major earthquake occurs, like the 1906 San Francisco event, a substantial amount of near-surface fault displacement takes place

as shown in 3d. If the only mode of shallow fault slip is through major earthquakes as with most of the 1906 break and the 1857 Fort Tejon break (Kerry Sieh, pers. commun.) then the seismic displacement must equal the net plate displacement for the earthquake cycle. Any net slip deficiency over the cycle must be taken up by other faults in the plate or result in permanent deformation. Along the San Andreas fault in California we observe that coseismic slip, whether from large or small earthquakes, is confined to the upper 15 to 20 km of the crust. Therefore the abrupt surface strain change should be confined to within 10 to 20 km of the fault. This is a general result of the elastic theory of dislocations (e.g. Kasahara, 1958; Chinnery, 1961; Walsh, 1969) for the case of constant mean stress σ_0.

In general the sum of the seismic slip plus preseismic slip will not be constant with depth, but should reflect a slip-deficient region near the base of the seismic slip zone. This results because the preseismic slip must taper upward and the seismic slip must taper downward in order to avoid infinite stresses. This slip deficiency has to be made up as a postseismic adjustment in order to return the slip and stress to the reference state. A second source of postseismic adjustment involves the asthenosphere. If we assume a somewhat viscous or viscoelastic asthenosphere, then the abrupt seismic motion resembles slip in a half space more than slip in a plate. As the viscous tractions relax the system becomes more platelike and surface strain changes may occur as predicted in Chapter 2. In addition a post-seismic increment of net plate offset should appear equal to the seismic plus postseismic contributions to $\Delta\bar{u}$ as predicted by equation (4).

The offset is identically zero for a given slip in a half space but is finite in a plate.

As a second example we consider a hypothetical earthquake cycle with constant plate velocity, as shown in figure 4. Once again a reference state (4a) is chosen after a major earthquake and any resulting postseismic adjustment. As the plates proceed to move past each other a net offset appears in the reference line. If no slip occurs anywhere with depth a uniform strain field develops with respect to the reference (fig. 4b), with the change in uniform stress given by equation (4), $\Delta\sigma_0 = \frac{\mu}{W}\Delta U_0$. If slip does appear a zone of anomalously high strain develops along the fault as in the previous example. Away from the fault the uniform shear persists corresponding to a mean stress $\Delta\sigma_0 = \frac{\mu}{W}(\Delta U_0 - \Delta\bar{u})$. As long as any portion of the fault remains locked $(\Delta U_0 - \Delta\bar{u})$ will always be positive resulting in a stress increase. At the fault trace the slope of the reference line is a direct measure of the near-surface stress and strain increase, as in the previous example. However, this time the near-surface stress is the sum of the stress concentration due to relaxation deeper on the fault plus the increase in mean stress.

If a major earthquake occurs, near-surface slip will change the strain field near the fault and a slip deficient zone is again expected at depth (fig. 4d). Postseismic slip adjustment is required to return to the reference state of stress and strain (fig. 4e). In addition, the asthenospheric relaxation must also be considered. With the displacement boundary conditions, ΔU_0 will not change significantly during the few minutes of seismic rupture. If the plate-asthenosphere system responds like a half space during seismic slip, then the coseismic

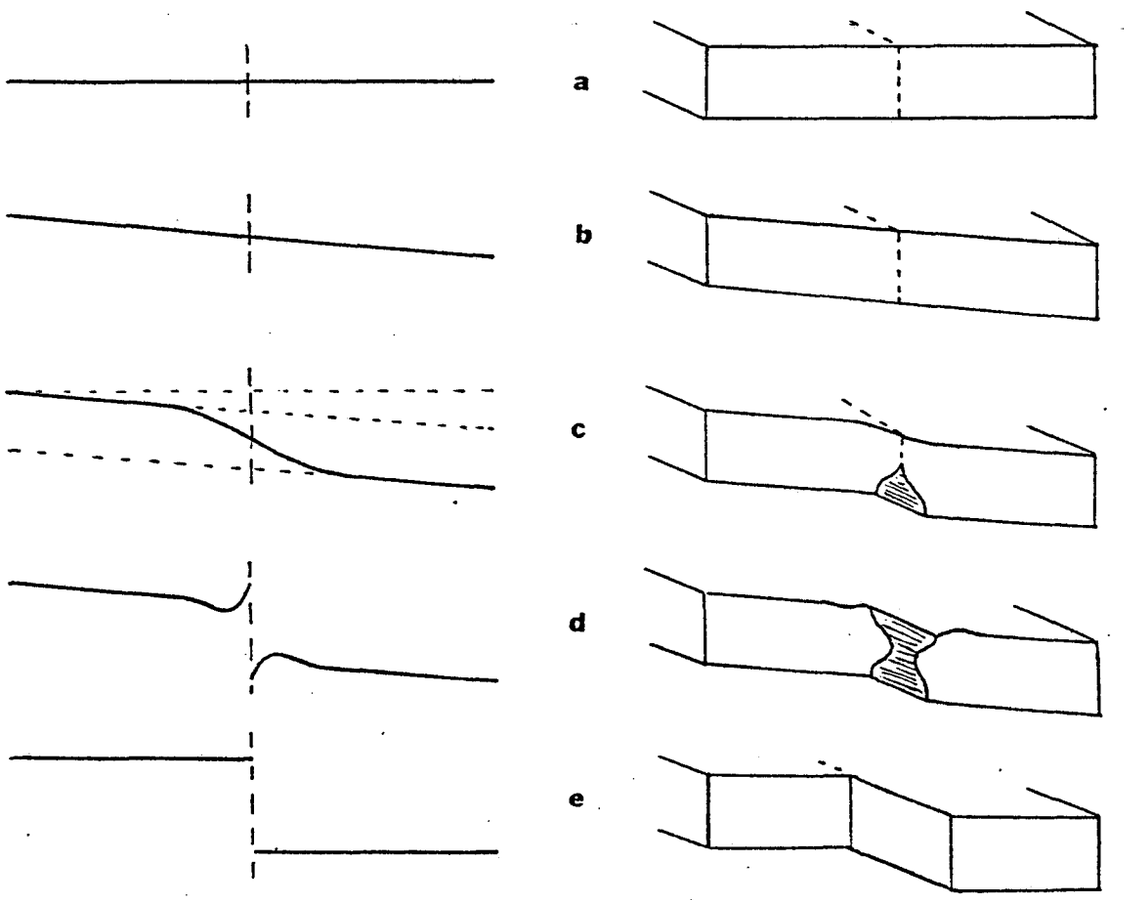

Figure 4. A hypothetical earthquake cycle with displacement boundary conditions.

contribution to $\Delta\bar{u}$ is zero because of the infinite-plate (half space) thickness. Hence, the reference line retains a nonzero slope. However, during postseismic relaxation the system becomes more platelike, and the reference line must flatten to the reference state, showing only a rigid block displacement.

The Effect of Three Dimensions

In order to bring the previous two-dimensional discussions into perspective we consider the role of boundary conditions in a three-dimensional plate geometry. Figure 5 shows a simplified version of the San Andreas fault in California. The shaded portions of the fault represent regions that slip only during major earthquakes (e.g. 1906 break to the north, 1857 to the south); unshaded portions presumably slide stably or with minor seismicity between earthquakes in order to accommodate net relative plate motion. For simplicity bends in the fault and slip on nearby faults are ignored, and the locked and active zones are shown to be of comparable length q.

During much of the earthquake cycle the slip and stress on the fault face are highly variable with position. Vertical variations in slip result in stress variations about the local mean, as discussed earlier, which smooth out away from the fault over distances comparable to the vertical wavelength. Likewise, variations in slip horizontally along the fault define a second wavelength of variation comparable to the zone length q. Hence during most of the earthquake cycle when asthenospheric stresses are small we should expect a fairly broad zone of width q along the fault within which the accumulated stress and strain vary significantly as we move from locked to slipping regions.

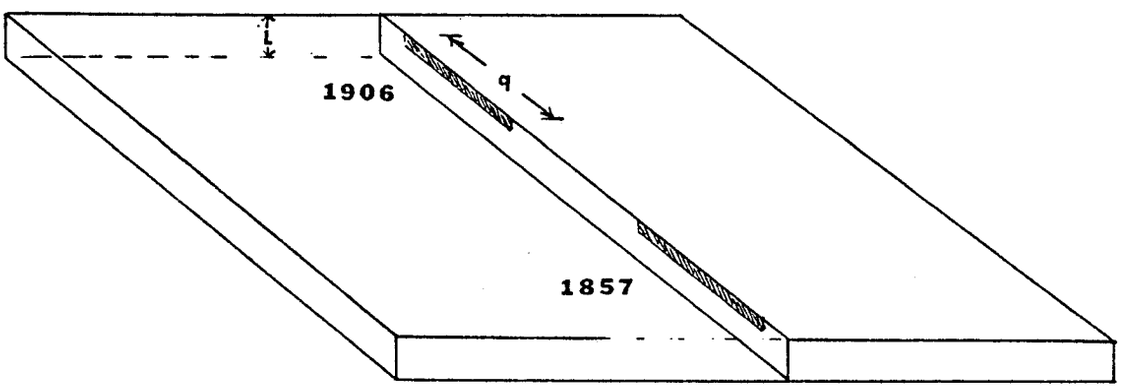

Figure 5. Simplified elastic plate model of the lithosphere in California. The San Andreas fault is modeled by a straight, vertical plate boundary. The regions represent currently locked portions of the fault approximately coinciding with the 1857 and 1906 earthquake ruptures.

This conclusion, a result of Saint-Venant's principle, has a bearing on the previous two-dimensional analyses. Because the length of each locked region and the length of the active region between are at least several times the plate thickness and more than 10 times the earthquake rupture depth, a two-dimensional description of each section alone has some validity within say, q/2 of the fault. However we are not free to choose arbitrarily stress vs. displacement boundary conditions. If, as Savage (1975) suggests, the mean stress σ_0 is constant in time, then figure 3 applies, and strain changes should be confined to less than a plate thickness from the fault. However equation (5) demands that for $\dot{\sigma} = 0$ the plate speed $\Delta\dot{U}_0$ must equal $\Delta\dot{\bar{u}}$. Since $\Delta\dot{\bar{u}}$ is highly variable with time on the locked zone the plate speed must also vary with time away from the fault. In contrast, the adjacent unlocked portion of the fault would very likely have constant slip rate $\Delta\dot{\bar{u}}$ under constant stress resulting in a constant plate speed. This discrepancy in plate speeds cannot be accommodated without strain accumulation at large distances from the fault. We conclude that the constant stress condition is not likely to hold in three dimensions if adjacent regions of the fault have significantly different slip behavior.

A more reasonable starting place is to note that at a distance $\sim q$ away from the fault strain perturbations in space and time due to slip differences on the fault should be essentially zero. The motion at $\sim q$ should be steady, consistent with our intuitive notion of plate tectonics. Closer to the fault at $\sim q/2$ the displacement field may be less steady, but a two-dimensional description of each section becomes fairly good. If the plate speed is constant at q/2, then the analysis

in figure 4 requires uniform shear strain accumulation and release out to distances ±q/2 from locked portions of the fault. If the plate speed is not constant at ±q/2 then the variation in speed is itself an indication of strain change at ±q/2.

It is clear that neither a constant stress nor constant velocity boundary condition is rigorously valid for a two-dimensional approximation of a 3-D fault geometry. A constant stress near the fault implies an infinitely soft boundary; a constant velocity implies infinite rigidity. The important point is that only a constant stress condition in two dimensions can completely eliminate changes in the strain field at distances from the fault greater than the plate thickness. It appears that two-dimensional analyses can be quite useful to predict or interpret strain accumulation, but a variable stress or nearly constant velocity boundary condition must be used. Accumulation and release of strain is expected out to distances comparable with the fault length (i.e. out to the limits of the 2-D analysis).

Discussion of Some Published Models

Until recently Reid's (1910) suggestion that accumulated strain is released during seismic fault slip has been taken quite literally. For example, Scholz and Fitch (1969), noting that coseismic strain along the San Andreas dies away at distances from the fault comparable to the rupture depth, argued that all accumulated strain must also die out just as rapidly. They correctly stated that if most of the hundreds of kilometers of relative plate motion that has occurred along the San Andreas are to be accommodated along a single fault, then the strain accumulated must somehow be released. Since they saw

no mechanism to release strain beyond a few tens of kilometers from the fault, they argued that no strain can accumulate there. What they neglected to consider was the influence of slip deeper on the plate boundary during the earthquake cycle.

Observations of pre- and postseismic crustal deformation, as reviewed in Chapter 1, were perhaps the first real clue that the rebound process was more involved. To explain these observations Scholz (1972) attributed all transient crustal deformation to aseismic fault slip. However, a rather complex pattern of slip was required, including substantial backslip, to fit the observations at Nankaido (see Chap. 1). Nur and Mavko (1974) suggested the simple alternative explanation that the Nankaido postseismic transient was due to viscous relaxation in the asthenosphere (see Chap. 2).

It seems likely that both viscous relaxation and aseismic slip should occur after major earthquakes. As mentioned earlier, shallow strike-slip earthquakes require substantial slip adjustment near the bottom of the rupture to accommodate the net plate offset. Deeper ruptures that break through the entire lithosphere might in principle require less slip adjustment. A similar statement would apply to major thrust-type earthquakes. In contrast the viscous component of adjustment occurs as the earthquake stress field relaxes in the asthenosphere, and the surface strain evolves from a half space to plate response to faulting. For shallow earthquakes a small viscous adjustment is expected, since the stresses fall off quickly with distance below the rupture. Deep earthquakes interact much more with the asthenosphere and produce a larger relaxation.

Turcotte and Spence (1974) propose the two-dimensional strike-slip fault model shown in figure 6. The model is essentially that described in figure 3 of this chapter with the added assumptions that the lower plate surface is stress-free throughout the earthquake cycle, and that the portions of the fault that slip aseismically are also stress-free. The resulting earthquake cycle can be described in terms of equation (4). Figure 6a shows the reference state of zero stress and strain at a point in time following a major earthquake and any subsequent relaxation. As the plates move past each other slip occurs at depth as shown in 6b. The mean stress increases and is concentrated entirely in the locked portion of the fault. The exact form of the displacement field is given by (eq. (4), Turcotte and Spence, 1974):

$$U = A\ \mathrm{Re}\left\{\ln\left[\frac{\sin(\frac{\pi z}{2L}) + \sqrt{\sin^2(\frac{\pi z}{2L}) - \sin^2(\frac{\pi a}{2L})}}{\sin(\frac{\pi a}{2L})}\right]\right\} \tag{6}$$

where $z = x + iy$, L is the plate thickness, and a is the depth of the locked zone. Far from the fault the displacement (6) reduces to:

$$U \simeq A[\frac{\pi y}{2L} - \ln \sin(\frac{\pi a}{2L})] \tag{7}$$

Equation (7) shows as we derived earlier that away from the fault, perturbations due to variations in slip die out, and the strain field is uniform shear. By defining $U = U_0$ at $y = W$, equation (7) can be rewritten as

$$\frac{A\pi\mu}{2L} = \frac{\mu}{W}(\Delta U_0 + 2A \ln \sin(\frac{\pi a}{2L})) \tag{8}$$

Comparing (8) with (4) we see that the mean stress is $\sigma_0 = \frac{A\pi\mu}{2L}$ or $A = \frac{2L\sigma_0}{\pi\mu}$, and the average slip is

$$\Delta\bar{u} = -2A \ln \sin(\frac{\pi a}{2L}) = \frac{-4L\sigma_0}{\pi\mu} \ln \sin(\frac{\pi a}{2L})$$

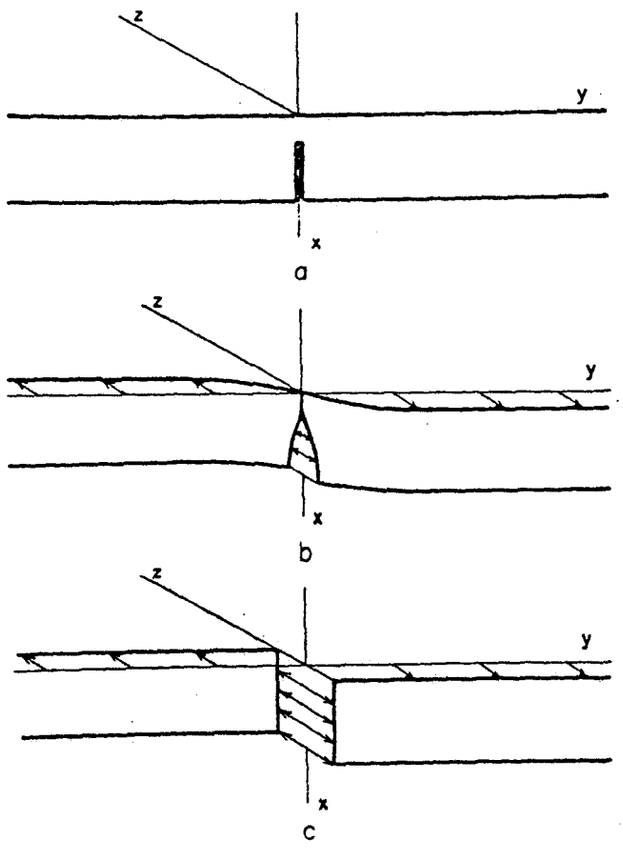

Figure 6. Accumulation and release of strain in a plate with a fault locked to a finite depth. (a) No displacements, (b) displacements with fault locked near surface, and (c) displacements after failure of the fault (after Turcotte and Spence, 1974).

When the failure stress is reached on the locked fault, an earthquake will occur, and subsequent postseismic adjustment returns the fault to its original state of zero stress and strain, as shown in figure 6c.

Turcotte and Spence (1974) extend these results qualitatively to three dimensions. Because the mean stress on the fault varies during the seismic cycle a nearly uniform strain field proportional to the mean stress accumulates and is released out to distances from the fault comparable with the fault length (i.e. out to distances where a two-dimensional description is still valid).

Savage (1975) criticizes the two-dimensional model of Turcotte and Spence based on comparisons of preseismic, coseismic, and postseismic slip. Figure 7a shows fault slip and stress as a function of depth on the fault. U_1 is the displacement (half the relative fault slip) and σ_1 is the stress on the fault at the end of the strain accumulation phase. (The stress singularity is due to the assumption of a perfectly locked, stress-free crack. A more realistic model can be found, but should not change the basic conclusions of the analysis.) To estimate the seismic slip, Savage solves for the displacement that completely cancels the preseismic stress concentration on the locked fault. This displacement (half the relative fault slip) is plotted as U_2 in figure 7a. As we will see below, the Turcotte-Spence model now requires an enormous amount of postseismic slip both at the surface and at depth to achieve the stress-free state shown in figure 6c.

As a modification Savage suggests that a constant stress boundary condition is more appropriate. In this case, a nonzero strength is required either on the unlocked fault or in the asthenosphere. The near-surface stress is seismically released and transferred downward,

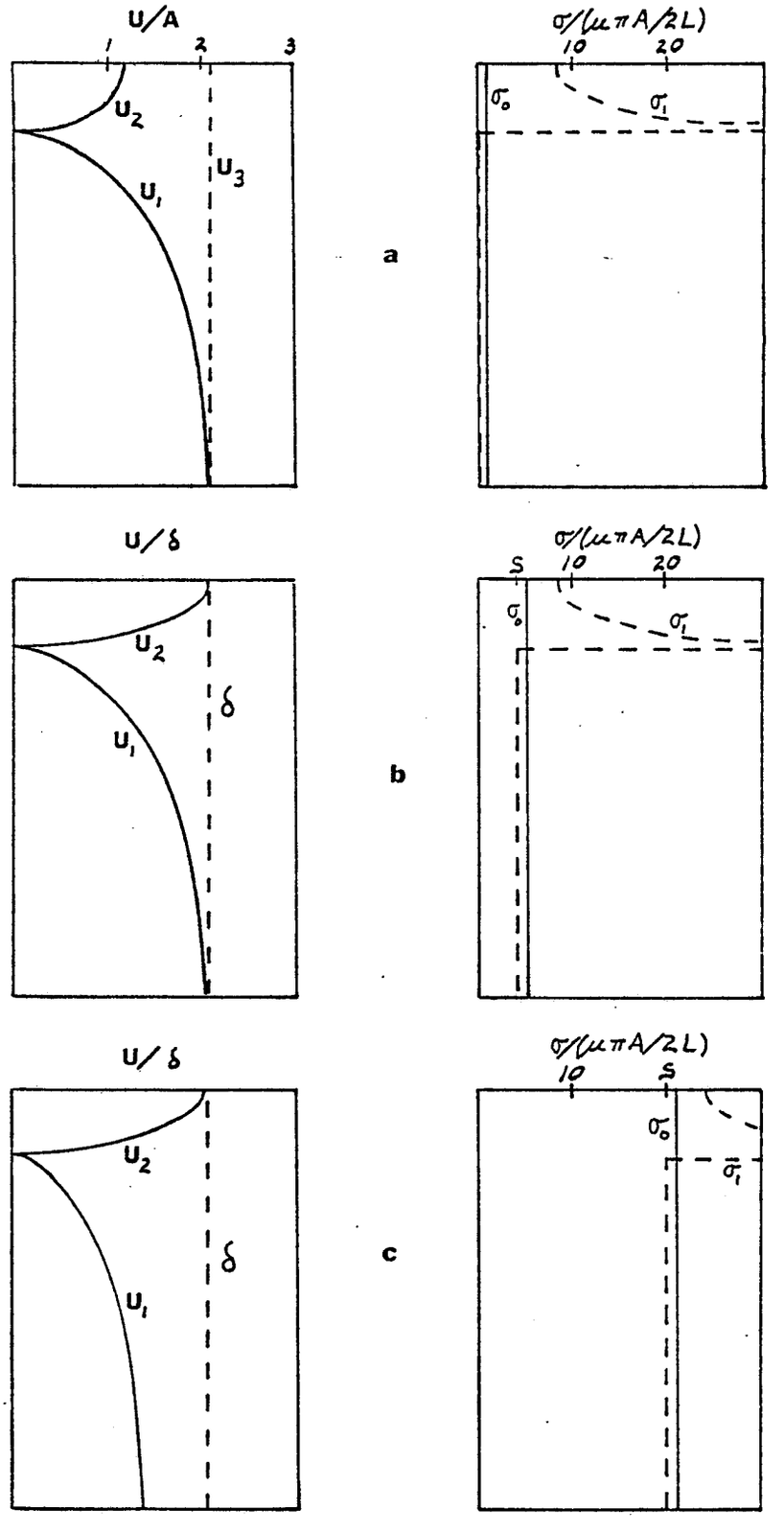

Figure 7. Fault slip and stress as a function of depth on the fault.

keeping the total load on the vertical section constant. By not requiring complete stress relaxation, postseismic slip is necessary only to remove slip deficiencies. Savage suggests the final slip state shown as U_3 in figure 7a. As shown earlier, an obvious consequence of the constant stress boundary condition is that in two dimensions strain accumulation and release is confined to within a few tens of kilometers of the fault.

In light of our previous analysis neither version of the model seems entirely appropriate for the San Andreas fault. Besides requiring enormous afterslip, the Turcotte and Spence model ignores viscous interaction with the asthenosphere, even during the seismic and post-seismic phases. This might not change significantly the expected postseismic surface deformation in California because of the shallow depth of seismicity. However Lachenbruch and Sass (1973) point out that the lack of a localized heat flow anomaly along the San Andreas strongly suggests a broad zone of viscous shearing below the seismogenic zone. This could include viscous shearing due to the asthenosphere as well as permanent inelastic deformation of the lithosphere itself. Neither the Turcotte and Spence model nor ours allows for the latter possibility. Brune (1974) suggests that the very broad observed anomaly might just as well be due to heat generated over the entire depth of the fault in the lithosphere. This would imply a time averaged stress of less than 200 bars for the upper 20 km of the fault, and a larger value of about 500 bars below. In either case a substantial strength is required on either the deep fault or in the asthenosphere, at least during portions of the seismic cycle.

A second problem concerns the relation between plate motion and preseismic, coseismic and postseismic slip. Savage's suggestion of a nonzero final stress reduces the required amount of postseismic slip. However as shown in figure 7a, substantial postseismic surface slip is still required to catch up with the bottom of the plate. Such surface slip has not been observed following either the 1857 or 1906 breaks.

If, in addition to the postseismic stress recommended by Savage, we require a nonzero preseismic stress deep on the fault, a larger relative coseismic slip is possible. Consider the case of a constant creep strengh S below the seismic zone. The preseismic displacement field is obtained by superimposing a uniform shear field given by

$$u = \frac{S}{\mu} y$$

onto the stress-free solution given by equation (6). Away from the fault the total displacement reduces to

$$U \simeq (\frac{A\pi}{2L} + \frac{S}{\mu})y - A \ln \sin(\frac{\pi a}{2L}) \qquad (9)$$

Comparing equation (9) with equation (4) we obtain the mean stress $\sigma_0 = \frac{A\pi\mu}{2L} + S$ or $A = \frac{2L}{\pi\mu}(\sigma_0 - S)$. Hence, for the same amount of preseismic slip the mean stress is increase by S. The increased coseismic displacement (half the relative fault slip) that will cancel the stress on the locked fault is obtained by adding the displacement

$$U \simeq \frac{Sa}{\mu}\sqrt{1-(\frac{x}{a})^2} \qquad (10)$$

which corresponds to a uniform stress drop S, to the displacement calculated by Savage. The coseismic surface displacement (for the case $a/L = 0.15$) is given by:

$$U \simeq 1.17A + \frac{Sa}{\mu} \tag{11}$$

A simple condition we can impose to find S is that during an earthquake cycle the total slip everywhere on the fault must equal the net plate offset. According to equation (4) this is equivalent to requiring that the net stress change over one full cycle be precisely zero. If we artificially start the system at a state of zero stress and strain, then equation (9) gives the plate displacement measured at y for the preseismic slip shown in figure 7a. If the seismic and postseismic slip smooth the displacement everywhere on the fault to some value δ, then the postseismic mean stress is proportional to the difference between the plate offset and fault slip:

$$\sigma_0 = \frac{\mu}{y}\left[\left(\frac{A\pi}{2L} + \frac{S}{\mu}\right)y - A \ln \sin\left(\frac{\pi a}{2L}\right) - \delta\right] \tag{12}$$

For the case of zero creep strength and postseismic stress, given by Turcotte and Spence, the total fault displacement (from equation 12) must be

$$\delta = A\left(\frac{\pi y}{2L} - \ln \sin \frac{\pi a}{2L}\right) \tag{13}$$

which gives $\delta = 6.17A$ for $a/L = 0.15$ and $y/L = 3$. This is a factor of 5 greater than the maximum coseismic slip and a factor of 3 greater than the preseismic slip shown in figure 7a. Savage's suggestion that the slip only catch up with the bottom of the plate or $\delta = 2.13A$ for $a/L = 0.15$, $y/L = 3$, gives a mean stress after postseismic adjustment of

$$\sigma_0 = \frac{\mu}{y}\, 4.04A + S \tag{14}$$

This value is somewhat larger than the preseismic creep strength S, which means that the strength must vary in a repeatable fashion during

the earthquake cycle. The net plate offset that must now be added during each cycle to repeat the process is $\delta = 2.13A$. An alternative is to assume that following postseismic adjustment the mean stress on the fault equals the preseismic creep strength--that is, the strength stays constant. Substituting this condition into equation (12) gives the same total fault slip $\delta = 6.17A$ as the stress-free case. This still requires a very large postseismic slip at depth. However, with a nonzero creep strength, the coseismic slip is larger and the required postseismic surface slip is reduced.

The magnitude of the stresses and slip can be estimated for an earthquake like the 1906 San Francisco event, assuming 5 m of surface offset and a rupture length of 15 km. To solve for the value of S that gives no postseismic surface slip we simply equate the coseismic slip given by equation (11) with the required value of δ. For the two alternative values of slip we obtain:

$$S = \begin{cases} 5\,\dfrac{\mu A}{a} & \delta = 6.17A \\ \text{for} & \\ \dfrac{\mu A}{a} & \delta = 2.13A \end{cases} \tag{15}$$

Setting $2\delta = 5$ m we obtain

$$A = \begin{cases} 0.4 & \delta = 6.17A \\ \text{for} & \\ 1.2 & \delta = 2.13A \end{cases} \tag{16}$$

Combining (15) and (16) and taking $\mu = 5 \cdot 10^5$ bars, S becomes

$$S = \begin{cases} 68 \text{ bars}, & \delta = 6.17A \\ 37 \text{ bars}, & \delta = 2.13A \end{cases}$$

The mean stress drop is equal to the average preseismic stress on the locked fault:

$$\Delta\sigma \simeq \frac{\pi\mu A}{2a} + S = \begin{cases} 89 \text{ bars}, & \delta = 6.17A \\ 98 \text{ bars}, & \delta = 2.13A \end{cases}$$

Figure 7 shows the stress and slip for these two cases for comparison with the stress-free fault. The case with $\delta = 2.13A$ (fig. 7b) requires the smallest postseismic slip at depth, but the creep strength must vary over the course of the cycle. The case with $\delta = 6.17A$ requires a very large postseismic slip at depth, but the creep strength is constant. At present we cannot resolve the appropriate model.

The differences between the Turcotte and Spence and the Savage versions of the model can be summarized in terms of boundary conditions. Savage prefers a constant stress condition, which in two dimensions confines strain accumulation close to the fault. We have already seen that this type of boundary condition is not compatible with a three-dimensional model. On the other hand, Turcotte and Spence favor a displacement boundary condition which gives a variable mean stress. We have proposed a modification which changes the strength distribution on the fault, but retains the displacement boundary condition. Estimates of the mean stress variation can be obtained from equation (4) for the 1906 San Francisco earthquake cycle. Using equations (8) and (16) the preseismic value of $\Delta\bar{u}$ is given by

$$\Delta\bar{u} = -2A \ln \sin\left(\frac{\pi a}{2L}\right) = \begin{cases} 1.2 \text{ m}, & \delta = 6.17A \\ 3.4 \text{ m}, & \delta = 2.13A \end{cases}$$

The postseismic value of $\Delta\bar{u}$, assuming the slip smooths to 5 m everywhere, is $\Delta\bar{u} = 5$ m. If the postseismic slip takes place quickly, the plate offset ΔU_0 is essentially unchanged. Assuming a fault break $q = 400$ km long, the two-dimensional description is limited to no more than about 200 km on each side of the fault. Therefore equation (4) predicts

a stress variation between the pre- and postseismic phases of

$$\Delta\sigma_0 \simeq \begin{cases} \frac{5m-1.2m}{4\cdot 10^5 m} = 4.7 \text{ bars}, & \delta = 6.17A \\ \frac{5m-3.4m}{4\cdot 10^5 m} = \quad 2 \text{ bars}, & \delta = 2.13A \end{cases}$$

corresponding to a strain change of

$$\varepsilon \simeq \begin{cases} 9\cdot 10^{-6}, & \delta = 6.17A \\ 4\cdot 10^{-6}, & \delta = 2.13A \end{cases}$$

Aseismic Slip Rates

Our previous analysis showed that the surface deformation more than a plate thickness from the fault is a direct measure of (1) the relative plate offset, (2) changes in the mean stress on the fault, and (3) the total fault slip. Unfortunately no observations of the far field deformation exist for faults like the San Andreas. Closer to the fault where most measurements are made the deformation is a function of both the far field boundary conditions and the details of slip on the fault itself. Since little is known about either the boundary conditions or the precise nature of slip and material properties at depth, there is considerable uncertainty in interpreting measurements of strain accumulation.

In this section we explore some general relations between the rate of fault slip at depth and strain accumulation at the surface. Since we assume very little about the distribution of strength on the fault many details about the spatial distribution of strain cannot be predicted. However we find that the time behavior of observations allows a good guess of the plate boundary conditions and the nature of stress drop that accompanies slip. The discussion applies to long

periods of strain accumulation after postseismic relaxation, if any, is complete. The system is presumably in a state of steady strain buildup.

In general the stress on a fault like that in figure 1 will be highly variable with position. The average stress will equal the far field applied stress σ_0 during periods when the asthenospheric tractions are zero, and is linearly related to the average fault slip $\Delta\bar{u}$ by equation (4). Variations of stress about the mean are linearly related to variations in fault slip and can be thought of as the deformational stress or dislocation stress σ_D. For aseismic motion inertial terms will be absent, and the local stress will be in equilibrium with the creep strength S wherever sliding occurs:

$$\sigma_0 + \sigma_D - S = 0 \tag{17}$$

Consider first the case where the relative slip rate $\Delta\dot{u}(x,z)$ is everywhere constant in time, though variable in space, during the period of strain accumulation. Since σ_D is a linear function of $\Delta u(x,z)$, $\dot{\sigma}_D$ must also be constant in time, and not identically zero unless $\Delta\dot{u}$ is identically zero. Likewise by equation (5) $\dot{\sigma}_0$ will be constant (or zero) for either a constant stress or constant plate speed boundary condition. Therefore the surface strain rate, regardless of spatial distribution will be constant in time as long as the lithosphere behaves linearly. In fact the only way to obtain constant strain rates at arbitrary surface locations is to have constant or zero slip rates at depth, and constant plate displacement rates far from the fault. Therefore a constant rate of deformation at a number of stations is a strong indication of constant slip rates.

The relation between strain rate and stress depends on the fault creep law. If the creep strength S is an arbitrary function of position and a monotonic increasing function of the slip rate $\Delta\dot{u}(x,z)$, then in principle we can solve for $\Delta\dot{u}$ as a function of S. Using equation (17) we can write

$$\Delta\dot{u} = f(x,z,S) = f(x,z,\sigma_0+\sigma_D) \tag{18}$$

For $\Delta\dot{u}$ to be constant in time equation (18) requires that $\dot{\sigma}_0 + \dot{\sigma}_D = 0$ wherever slip is occurring. $\dot{\sigma}_0$ is constant in space by definition. Consequently $\dot{\sigma}_D$, the rate of stress drop on slipping portions of the fault, must be constant in space and in time as long as the slip rate $\Delta\dot{u}$ is constant. If instead, S is a simple function of position, independent of slip rate, then by equation (17), the sum $(\dot{\sigma}_0 + \dot{\sigma}_D)$ must be zero. Again this implies that $\dot{\sigma}_D$ be constant in space and time for $\Delta\dot{u}$ constant.

If S is a more complicated function of slip rate or time, say exhibiting an upper yield or softening, then it is difficult to predict exactly the stress change $\dot{\sigma}_D$. However, the long-term behavior, averaged over several episodes of yielding and stress release, can very likely be approximated as fluctuations about some mean strength. If this mean strength is constant during much of the phase of strain accumulation or is monotonically related to the time averaged slip rate, then the time averaged stress drop $\dot{\sigma}_D$ should be constant in space and time if the average slip rate is constant in time.

As an example we approximate the locked portion of the San Andreas fault as a two-dimensional fault similar to that in figure 6. The fault is locked to depth a. Below the locked zone slip occurs with

an unknown spatial distribution of rates, but the rates appear to be constant in time. If the creep strength S (or its long-term average) varies arbitrarily with depth but is constant or monotonic with slip rate, then the rate of stress drop $\dot{\sigma}_D$ is constant in space and time below depth a. The changing displacement field that will give a constant stress drop over the lower portion of fault is exactly that given by the time derivative of equation (6), with $\dot{A} = 2L\dot{\sigma}_D/\pi\mu$. That is, the change of stress and deformation is the same as for a stress-free fault surface with the same distribution of locked portions. For a fault with a/L = 0.15 as in our previous examples the slip rate at the plate bottom is

$$\Delta\dot{u} \simeq 4.3\dot{A} \tag{19}$$

The relative plate speed measured at y = ±3L is given by

$$\Delta\dot{U}_0 \simeq 12.3\dot{A} \tag{20}$$

The strain rate at the fault trace is

$$\frac{1}{2}\frac{\partial}{\partial y}\dot{U} \simeq 3.4\dot{A}/L \tag{21}$$

We can determine $\dot{A}$ from a measurement of any one of the quantities in (19), (20) or (21) and consequently solve for the remainder of the deformation field. The northern locked portion of the San Andreas around San Francisco is difficult to describe with the model since active slip on the Hayward and Calaveras faults complicates the strain field (Thatcher, 1975b). Nevertheless an approximate fit can be tried using a strain rate of $0.17 \pm 0.04 \times 10^{-6}$ yr^{-1} (from 1938-61) measured on the Point Reyes-Petaluma triangulation arc where the region most approximates a locked plate boundary (Thatcher, 1975b). Equating with equation (21) we obtain $\dot{A} \simeq 0.5$. This gives a relative plate

speed of ∿6 cm/yr. This value of plate speed is higher than either the ∿5.5 cm/yr determined by Atwater and Molnar (1973), the 3.7 ± 3 cm/yr determined by Sieh (pers. commun., 1977), or the 3.2 ± 5 cm/yr reported by Savage and Burford (1973). The most likely explanation is that the strain rate of 0.17×10^{-6} is due to both slip at depth and the complicated pattern of fault slip to the southeast in the San Francisco Bay area, and is therefore greater than might be expected along a more two-dimensional section of the fault. Turcotte and Spence (1974) performed a similar calculation using an even larger value of strain rate measured south of San Francisco.

Several points can be made with this example. If the creep strength stays constant while the slip rate is constant, regardless of other details of the strength law, then the mean stress must increase linearly with time. This is true because the plate speed, equation (20), is constant and is greater than the slip rate, equation (19). In contrast, if a constant mean stress boundary condition is imposed, as suggested by Savage (1975) then an observed constant slip rate requires that the creep strength decrease linearly with time as the fault slips. From equation (9) the strength must change precisely as $\dot{S} = -\pi\mu\dot{A}/2L$. Although we cannot eliminate this possibility, such a precise relation does not seem likely to occur. Similarly a creep strength that is constant or monotonic increasing with slip rate must result in a decaying slip rate if the mean stress is kept constant.

It should be added that a constant stress drop analysis like this requires a slight modification to be strictly valid. In general a slip distribution that results in a uniform stress drop will cause stress singularities just outside the slip. This concentration would

probably result in a broadening of the slip zone which would eliminate the singularities but may slightly increase the observed rate of strain accumulation.

A direct example of a nearly constant observed slip rate is the active region of the San Andreas fault between San Juan Batista and Cholame. Figure 8a shows a smoothed record of 22 years of creep at the Cinega Winery near the northern end of the active region. Although the detailed record (fig. 8b) is episodic, the long-term rate is remarkably constant at $\sim$1.2 cm/yr. In general the active portion of the San Andreas has slipped fairly uniformly in time for the last several decades, with the greatest rates of 2.5 to 3.1 cm/yr near the center and tapering to zero at each of the locked ends (Sieh, pers. commun., 1977).

If the constancy of the surface slip is indicative of similar deeper slip, then the previous discussion applies. A constant stress boundary condition implies that the average creep strength is decreasing linearly with time. However, we see no reason for the material properties to change systematically in this way. On the other hand a constant long-term creep strength, allowing for repeatable fluctuations associated with local yielding, implies a velocity boundary condition and a small gradual increase in mean stress on the fault.

We can estimate the relation between fault creep rate and plate speed using the simple model in figure 9a. The central portion of the fault with length q_1 is slipping uniformly in time. The strength on the slipping portion is unknown but is assumed to be constant in time. At each end a portion of fault with length q_2 is locked to depth a. The deformation along the locked portions is roughly two dimensional

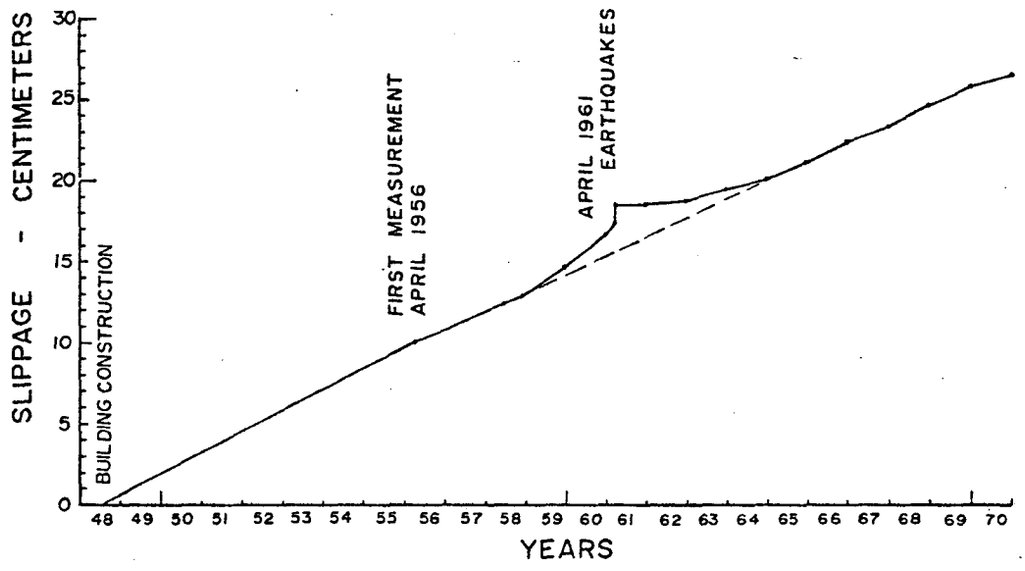

a.

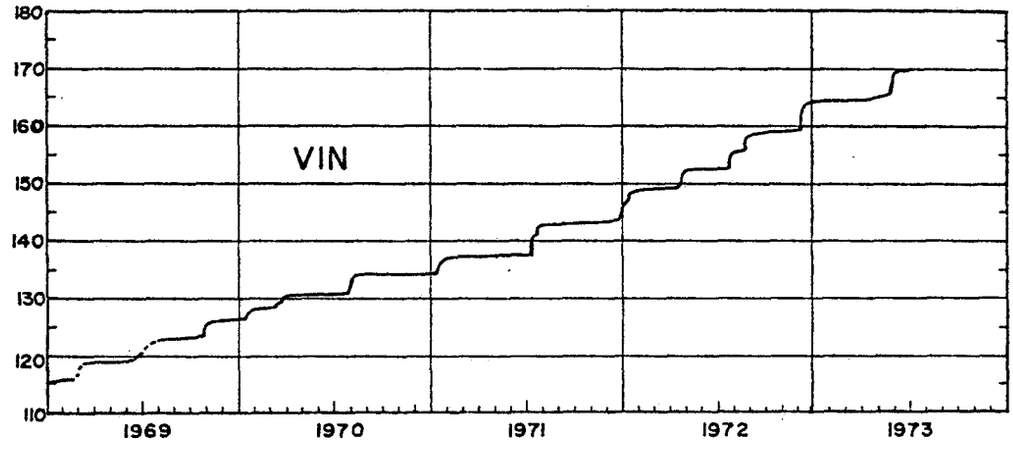

b.

Figure 8. (a) Fault slippage at Cienega Winery (VIN) 1948-1972, (b) Fault creep slippage (millimeters) since 1958 at VIN, 1969-1973. (after Nason, 1973)

as in figure 6 and the displacement is given by the time derivative of equation (6). Beyond $\sim L$ from the fault the deformation reduces to:

$$\dot{U} \simeq \dot{A}_2 \frac{\pi y}{2L} - \dot{A}_2 \ln \sin \frac{\pi a}{2L} \tag{22}$$

where $A_2 = \frac{2L\sigma_2}{\pi\mu}$ and σ_2 is the mean stress acting on the locked portion of fault. Hence, away from the locked fault the effect of the deep slip is the same as replacing the locked fault with a uniformly slipping fault with slip rate $-\dot{A}_2 \ln \sin \frac{\pi a}{2L}$.

Throughout much of the central active region, the fault is insensitive to the exact distribution of stress and slip on the locked portions of fault, as long as q_1 is several times longer than L. Hence the description of creep on this section is approximately reduced to the two-dimensional plane stress problem shown in figure 9b with the partially locked portions of fault replaced with the equivalent uniform slip inferred from equation (22). The solution of Turcotte and Spence (1974), given by equation (6) for the strike-slip system in figure 6 is equivalent to the antiplane deformation of an infinite row of coplanar cracks, each of length 2a and separated by 2(L-a). By simply multiplying equation (6) by $1/(1+\nu)$ where ν is Poisson's ratio the solution for plane stress shearing of the infinite row of cracks is obtained. Using this solution to approximate the system in figure 9b is equivalent to assuming that the average stress and displacement behavior at great distances away along the fault are somewhat similar to that in California. Using this modified form of equation (7), the plate speed $\Delta\dot{U}_0$ at $y \simeq q_1$ resulting from shearing becomes

$$\Delta\dot{U}_0 \simeq \dot{A}_1 \frac{2}{1+\nu}\left[\frac{\pi q_1}{q_1+q_2} - \ln \sin \frac{\pi q_2}{2(q_1+q_2)}\right] - 2\dot{A}_2 \ln \sin \frac{\pi a}{2L} \tag{23}$$

where $A_1 = (q_1+q_2)\sigma_1/\pi\mu$, σ_1 is the mean shear stress across the entire

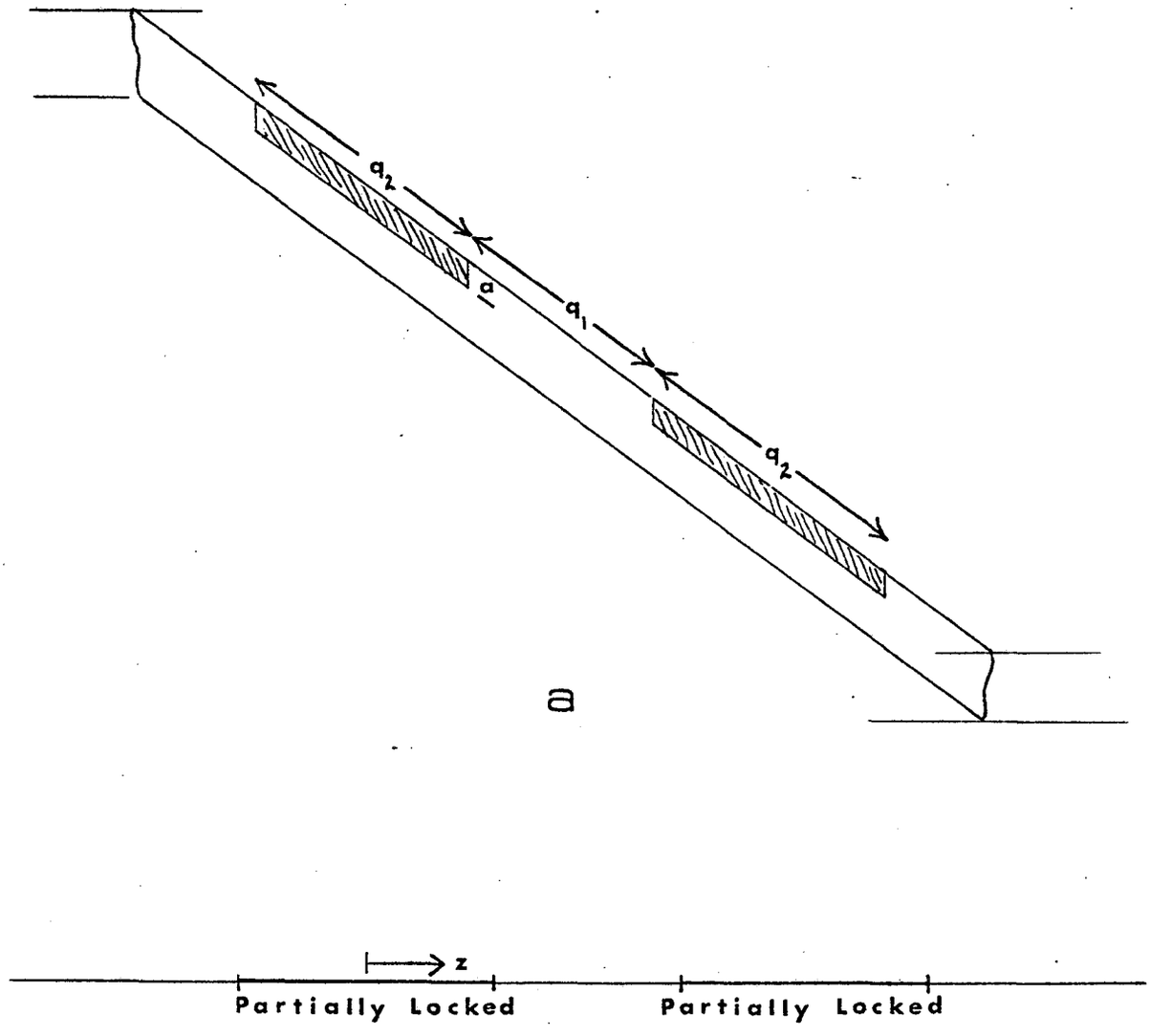

Figure 9. (a) Simplified San Andreas fault model similar to figure 5. (b) Map view of fault model showing active and partially locked portions of fault for plane stress calculation of fault creep.

system, and the last term in (23) is added to correct for the partial slip on the locked portions of the fault. The average stress σ_2 across the locked portions of fault is related to the mean stress σ_1 across the entire system by a simple weighted average:

$$\sigma_2 \simeq \left(\frac{q_1+q_2}{q_2}\right)\sigma_1$$

which is equivalent to assuring that the entire load integrated over the plate away from the fault is equal to the stress integrated over the fault face. Hence A_1 and A_2 are related by

$$A_2 = \frac{2L}{q_2} A_1$$

Solving for $\dot{A}_1$ in equation (23) gives

$$\dot{A}_1 = \frac{\Delta\dot{U}_0}{2\frac{1}{(1+\nu)}\left[\frac{\pi q_1}{q_1+q_2} - \ln \sin \frac{\pi q_2}{2(q_1+q_2)}\right] - \frac{4L}{q_2} \ln \sin\frac{\pi a}{2L}} \tag{24}$$

Finally the slip rate $\Delta\dot{u}$ on the active portion of fault is given by the plane stress form of equation (6) plus the correction for effective slip on the locked portions:

$$\Delta\dot{U} = \frac{2\dot{A}_1}{(1+\nu)} \ln\left[\frac{\sin\frac{\pi z}{q_1+q_2} + \sqrt{\sin^2\left(\frac{\pi z}{q_1+q_2}\right) - \sin^2\left(\frac{\pi q_2}{2(q_1+q_2)}\right)}}{\sin\frac{\pi q_2}{2(q_1+q_2)}}\right] - 4\dot{A}_1 \frac{L}{q_2} \ln \sin\frac{\pi a}{2L} \tag{25}$$

where z is distance along the trace of the fault as shown in figure 9b. To estimate the creep rate in the active region of central California we set a = 15 km, L = 100 km, q_2 = 400 km, and q_1 = 300 km. (Approximately 100 km is added to the length of the active San Andreas from San Juan Batista to Cholame to include the extra compliance due to slip on the Hayward and Calaveras faults.) Substituting into equation (25) this gives

$$\Delta\dot{u} \simeq 0.7\ \Delta\dot{U}_0$$

for the maximum creep which is near the center of the active region. Away from the center the rate should taper to zero at the locked ends of the fault.

Kerry Sieh (pers. commun., 1977) has determined that the long-term slip rate (over many earthquake cycles) for much of the San Andreas fault is about 3.4 to 4.0 cm/yr based on geologic evidence. Sieh also reports a maximum creep rate for the last several decades of 2.5 to 3.2 cm/yr. Using $\Delta\dot{U}_0$ = 3.4–4.0 cm/yr in equation (26) gives a maximum creep rate of $\Delta\dot{u}$ = 2.4–2.8 cm/yr. The good agreement between theory and observation is perhaps fortuitous given the crude calculation. Nevertheless a number of points can be made. During steady strain accumulation the average slip rate anywhere on the fault should be less than the plate speed as long as substantial portions of the fault are locked. This is the same conclusion drawn by comparing equations (19) and (20) for a two-dimensional fault. The locked portions of fault and the elastic strength of the plate resist motion on slipping portions, even if the creep strength on the slipping portions is zero. As a result, a slip deficiency accumulates over this part of the earthquake cycle which must be made up when an earthquake relieves the locked ends. Sieh (pers. commun.) has indicated that the 1857 break may have extended as far as half way through the present active region of the fault. This may have made up for at least part of the deficiency from the previous cycle. In general, a period of accelerated creep is expected on the active region after seismic release of the locked ends. No evidence for or against this accelerated creep has been reported for central California immediately after either the 1857 or

1906 earthquakes. However, the same form of adjustment can explain the postseismic slip at depth following the 1906 break (Thatcher, 1975a).

A final comment concerns precursory slip. In figure 7 the preseismic slip is plotted as u_1 for a range of fault creep strengths. In each case the slip tapers to zero at the locked portion of fault, just as in our present discussion of surface creep. This is an intuitively reasonable result for any elastic material. The important point is that before the locked portion is released seismically, the deep slip cannot everywhere catch up with the net plate offset, regardless of the creep strength. Any episode of precursory slip or instability at depth can be interpreted as a reduction in creep strength. Consequently, even if the instability is perfect and the creep strength drops to zero, the slip deficiencies at depth cannot be completely made up in preseismic slip. Seismic evidence in California indicates that the deep slip is not corrected during earthquakes. Therefore we would always expect at least some postseismic slip after major earthquakes on previously locked portions of fault.

Conclusion

We have examined some simple aspects of stress and strain accumulation along a strike-slip plate boundary. In two dimensions a constant stress boundary condition confines all strain changes during an earthquake cycle to within a few tens of kilometers of the fault. In contrast, a constant plate speed boundary condition results in a small but varying component of uniform shear out to great distances from the fault. Along the major active and locked regions of the San Andreas

fault a two-dimensional analysis has some validity. However, the three dimensionality of the system determines the boundary conditions for the two-dimensional approximations. It appears that when adjacent portions of the fault vary from smoothly slipping to locked behavior, each section alone is best described by constant plate rate boundary condition. This suggests that shear strains on the order of $4\text{-}9 \times 10^{-6}$ accumulated and were released out to distances of hundreds of kilometers during the 1906 San Francisco earthquake cycle.

Using this type of analysis we have proposed a modification to the Turcotte and Spence (1974) model of the San Andreas. By adding a nonzero creep strength at depth on the fault a larger stress accumulates on the locked portions, allowing a greater coseismic surface slip. This can eliminate the need for postseismic surface slip to accommodate the net plate offset. The magnitude of creep strength depends on a number of factors. If the seismic surface slip is assumed to just equal the accumulated preseismic slip at the bottom of the plate, then a minimum preseismic creep strength of about 37 bars is needed to account for 5 m of surface slip during an event like the 1906 San Francisco earthquake. However, this implies that the creep strength at the beginning of strain accumulation is greater than it is just before an earthquake. On the other hand, if the creep strength is constant during the entire period of strain accumulation, a creep strength of at least 68 bars is required, and the seismic slip is greater than the preseismic slip at the bottom of the plate.

References

Atwater, T. and P. Molnar, Relative motion of the Pacific and North American plates deduced from sea-floor spreading in the Atlantic, Indian and South Pacific oceans, in Proc. Conf. Tectonic Problems of the San Andreas Fault, p. 136, Stanford University Press, 1973.

Brune, J.N., Current status of understanding quasi-permanent fields associated with earthquakes, EOS, 55, 9, 820-827, 1974.

Chinnery, M. S., The deformation of the ground around surface faults, Bull., Seismol., Soc. Amer., 51, 355-372, 1961.

Kasahara, K., Physical condition of earthquake faults as deduced from geodetic data, Bull. Earthquake Res. Inst. Tokyo Univ., 36, 455-464, 1958.

Lachenbruch, A. H. and J. H. Sass, Thermo-mechanical aspects of the San Andreas fault system, in Proc. Conf. Tectonic Problems of the San Andreas Fault, p. 192, Stanford University Press, 1973.

Nason, R. D., Fault creep and earthquakes on the San Andreas fault, in Proc. Conf. Tectonic Problems of the San Andreas Fault, p. 275, Stanford University Press, 1973.

Nur, A. and G. Mavko, Postseismic viscoelastic rebound, Science, 183, 4121, 204-206, 1974.

Reid, H. F., The mechanics of the earthquake, in: The California Earthquake of April 18, 1906. Rept. State Earthquake Invest. Comm., Carnegie Inst., Washington, D. C., 1910.

Rundle, J. B. and D. D. Jackson, Can a unique model of the San Andreas fault be found from geodetic triangulation data?, EOS, 57, 12, 1012, 1976.

Savage, J. C., Comment on 'An analysis of strain accumulation on a strike slip fault', by D.L. Turcotte and D.A. Spence, J. Geophys. Res., 80, 29, 4111-4114, 1975.

Savage, J.C. and R. O. Burford, Accumulation of tectonic strain in California, Bull. Seismol. Soc. Amer., 60, 6, 1877-1896, 1970.

Savage, J. C. and R. O. Burford, Geodetic determination of relative plate motion in central California, J. Geophys. Res., 78, 5, 832-845, 1973.

Scholz, C. H., Crustal movements in tectonic areas, in: E. F. Savarensky and T. Rikitake (editors) Forerunners of Strong Earthquakes, Tectonophysics, 14(3/4), 201-217, 1972.

Scholz, C. H. and T. J. Fitch, Strain accumulation along the San Andreas fault, J. Geophys. Res., 74, 27, 6649-6666, 1969.

Thatcher, W., Strain accumulation and release mechanism of the 1906 San Francisco earthquake, J. Geophys. Res., 80, 35,4862-4872, 1975a.

Thatcher, W.,Strain accumulation on the northern San Andreas fault zone since 1906, J. Geophys. Res., 80, 35, 4873-4880, 1975b.

Turcotte, D. L. and E. R. Oxburgh, Mid-plate tectonics, Nature, 244, 5415, 337-339, 1973.

Turcotte, D. L. and D. A. Spence, An analysis of strain accumulation on a strike slip fault, J. Geophys. Res., 79, 29, 4407-4412, 1974.

Walcott, R. I., Structure of the earth from glacio-isostatic rebound, in Annual Review of Earth and Planetary Sciences, vol. 1, edited by F. A. Donath, F. G. Stehli and G. W. Wetherill, Annual Reviews, Palo Alto, Ca., 1973.

Walsh, J. B., Dip angle of faults as calculated from surface deformation, J. Geophys. Res., 74, 2070-2080/1969.

PART II: THE EFFECT OF CRACKS ON WAVE PROPAGATION IN ROCKS

CHAPTER 5

THE EFFECT OF NON-ELLIPTICAL CRACKS ON THE COMPRESSIBILITY OF ROCKS

Introduction

The mechanical behavior of rocks depends strongly upon the geometry of pore space. In particular, long narrow cracks, ranging from microcracks to joints and fractures, can drastically reduce the effective moduli of a rock system. The closing of microcracks, for example, can account for the typically observed increase in modulus with increasing confining pressure below several kilobars (e.g. Birch, 1960; Brace, 1965; Simmons and others, 1974). Similarly, Nur (1971) attributed the directional dependence of seismic velocity in nonhydrostatically stressed samples to the anisotropic closure of cracks.

Theoretical models for the mechanical behavior of rocks containing cracks and pores have been presented by a number of authors. Many of these models incorporate the solution for the deformation of the individual cracks under applied stress. Consequently only two-dimensional elliptical cracks and three-dimensional ellipsoidal cracks were considered (e.g. Eshelby, 1957; Walsh, 1965a; O'Connell and Budiansky, 1974; Kuster and Tolsoz, 1974), since solutions for more realistic crack shapes are generally not available in closed form. The choice of elliptical shapes has several important consequences, particularly for very thin cracks. Under increasing hydrostatic compression the crack length remains constant and stress singularities appear at the blunted crack tips. Berg (1965) has shown that at sufficiently high pressure the thin elliptical crack abruptly closes, making contact

simultaneously over the entire crack surface. Since the compressibility is a function of crack length and aspect ratio it is not clear which of the calculated effects are real or just artifacts of the assumed elliptic shape.

Both visual inspection and common sense suggest that almost no cracks in situ are ellipsoidal cavities. We expect that instead typical cracks are irregular in shape, possessing in particular a wide range of edge configurations. Cracks may terminate with blunt edges, such as the ellipsoidal case, or with very fine edges such as at a contact of two slightly irregular parallel surfaces. The compliance to stress of the latter cracks may be quite different from ellipsoidal ones, leading to a different overall compressibility of the rock. It is therefore important to determine the elastic response of a rock with nonellipsoidal cracks, and compare the results with the ellipsoidal case.

In this chapter we examine the influence of a broad class of non-elliptical, two-dimensional cracks on the effective compressibility of (dry) rocks. In the first section that follows we compute the deformation of an almost arbitrarily shaped thin crack using the well-developed theory of elastic dislocations. A particularly simple set of closed form polynomial solutions is obtained in a manner similar to Delameter (1974). In the second section the effective compressibility is computed as a function of crack deformation. The general case as well as specific examples are presented. The remainder of the chapter gives a discussion of the model in comparison with the elliptical crack results, including the interpretation of a typical stress-strain curve.

Calculation of Crack Deformation Under Hydrostatic Pressure

We approximate the rock as an isotropic elastic solid containing a distribution of randomly oriented (dry) cracks or pores of the type shown schematically in figure 1. For mathematical convenience the pores are treated as two dimensional cracks in plane strain, and the separate pores are assumed not to interact. Furthermore, only flat planar cracks are considered, with aspect ratio $\alpha << 1$ (where $\alpha = b/c$, and c and b are the half length and maximum half-width of the crack). By limiting our study to flat, two dimensional cracks we can easily solve for the crack deformation under varying hydrostatic pressure by applying two dimensional elastic dislocation theory. (See for example, Bilby and Eshelby 1968).

The problem of opening a crack under tension is conceptually simpler and more conveniently posed than crack closing under pressure. Therefore, in the derivation of crack closure that follows we first close the crack with a large confining pressure and then study the crack shape as the stress is relaxed. For hydrostatic stress the crack shape is path independent (ie. a simple function of applied stress), so that the crack closing problem is exactly equivalent to the opening problem.

Consider a thin crack of shape $U_0(x)$ and length $2c_o$ (figure 1) where $U_o(x)$ and dU_o/dx are continuous, smooth functions of x. (We define these as the reference state of zero stress and strain regardless of the stress history leading to the formation of U_o.) In our analysis we will emphasize non-blunted cracks with tapered ends such

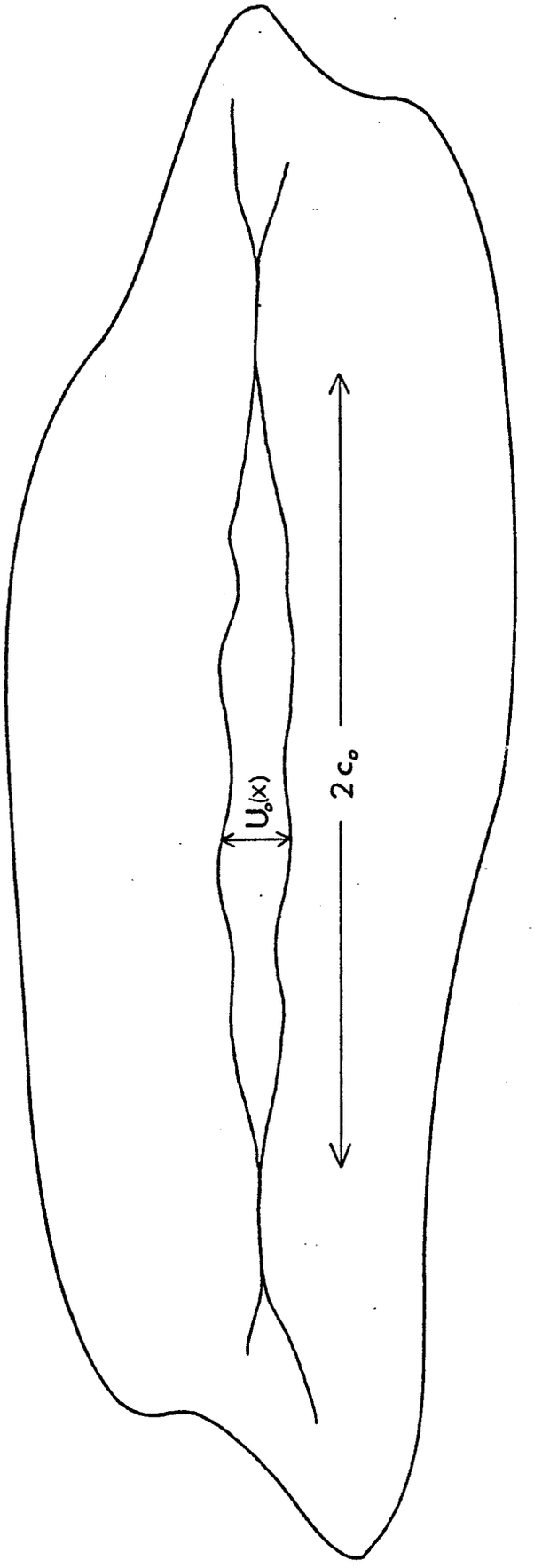

Figure 1. A flat two-dimensional crack with tapered ends. The width, given by $U_o(x)$, is shown exagerated.

that $\frac{dU_o(\pm c_o)}{dx} = 0$. The effect of these cracks will be compared specifically with elliptical cracks for which solutions already exist (eg. Walsh 1965, Berg 1965).

Imagine that a hydrostatic stress -P (stress is defined as positive in tension) is applied so that the crack is just closed. The strain field is a superposition of the uniform hydrostatic strain and the pertubation due to the closed crack. This perturbation is just the strain field due to a continuous distribution to infinitesimal elastic edge dislocations with density function

$$B_o(x) = \frac{d}{dx} U_o(x) \tag{1}$$

Likewise, the stress field is given by

$$\sigma_{ij} = -P'\delta_{ij} + \sigma_{ij}^{c}$$

where σ_{ij}^{c} is the stress due to the closed crack. In particular the normal stress on the plane $y = 0$ is

$$\sigma_o(x) = -P'(x) + \sigma_o^{c}(x)$$

where

$$\sigma_o^{c}(x) = \frac{\mu}{2\pi(1-\nu)} \int_{-c_o}^{c_o} \frac{B_o(z)}{x-z}\, dz \tag{2}$$

(eg. Bilbly and Eshelby, 1968). Here, μ is the intrinsic shear modulus of the rock material and ν is Poisson's ratio. Because $U_o(x)$ is smooth and $B_o(\pm c_o) = 0$, the stresses are finite everywhere including the crack tips and $\sigma_o^{c} \to 0$ very far from the crack.

If the hydrostatic stress is now slightly relaxed by an amount τ (which is equivalent to superimposing a tension τ), the crack will

begin to reopen over a region $-c<x<c$ where $c \leq c_o$, with shapes $U(x,P)$ where $P = (P'-\tau)$. (We have assumed for simplicity that the original crack is symmetric, ie $U_o(x)$ is an even function of x. This assures that the deformed crack at any value of $P \geq 0$ is also symmetric.) The crack opening $U(x,P)$ at this point can be thought of as a new distribution of infinitesimal elastic edge dislocations with density function

$$B(x,P) = - \frac{\partial U(x,P)}{\partial x} \tag{3}$$

The problem of finding the deformed crack shape reduces to finding the distribution of dislocations $B(x,P)$ subject to the conditions that the opened crack faces are stress free, ie.,

$$\sigma_o + \tau + \sigma^c = 0, \qquad |x| \leq c \tag{4}$$

where σ^c is the stress due to the crack opening dislocations:

$$\sigma^c = \frac{\mu}{2\pi(1-\nu)} \int_{-c}^{c} \frac{B(z,P)}{x-z}\, dz \tag{5}$$

and $U(x,P) = B(x,P) = 0$ for $|x| \geq c$. The density function $B(x,P)$ is found by solving the integral equation obtained by combining (4) and (5).

$$\int_{-c}^{c} \frac{B(z,P)}{x-z}\, dz = - \frac{2\pi(1-\nu)}{\mu} [\sigma_o{}^c(x)-P] \qquad |x| \leq c \tag{6}$$

where the right hand side of (6) is a known function of the original

crack shape $U_o(x)$, and the applied hydrostatic pressure P. The condition that a solution to equation (6) exist with finite stresses everywhere is given by

$$\int_{-c}^{c} \frac{\sigma_o^c(x)-P}{\sqrt{c^2-x^2}}\,dx = 0$$

(See Muskhelishvili 1953, p. 256).

Using the integral (B-3 Appendix B), this becomes

$$P = \frac{1}{\pi}\int_{-c}^{c} \frac{\sigma_o^c(x)}{\sqrt{c^2-x^2}}\,dx \qquad (7)$$

$$= \frac{\mu}{2\pi^2(1-\nu)}\int_{-c}^{c}\frac{1}{\sqrt{c^2-x^2}}\int_{-c_o}^{c_o}\frac{\frac{dU_o(z)}{dz}}{x-z}\,dz\,dx$$

For a given original crack shape U_o with length $2c_o$, equation (7) gives a relation between the applied hydrostatic pressure P and the reduced length c. We will see with some numerical examples in a later section that for cracks with tapered ends (ie. no stress singularities) crack closing from hydrostatic stress is accompanied by crack shortening.

The solution of equation (6) is given by:

$$B(x,P) = \frac{2(1-\nu)}{\pi\mu}\sqrt{c^2-x^2}\int_{-c}^{c}\frac{\sigma_o^c(z)-P}{(x-z)\sqrt{c^2-z^2}}\,dz \qquad |x| < c \qquad (8)$$

(see Muskhelishvili, 1953, p. 257) where c is given by equation (7). The actual crack shape is found by integrating $-B(x,P)$:

$$U(x,P) = \frac{-2(1-\nu)}{\pi\mu}\int_{-c}^{x}\sqrt{c^2-t^2}\int_{-c}^{c}\frac{\sigma_o^c(z)-P}{(t-z)\sqrt{c^2-z^2}}\,dz \qquad |x| < c \qquad (9)$$

Equations (8) and (9) can be slightly simplified by dropping P (or

adding any constant) from the integrand since

$$\int_{-c}^{c} \frac{dz}{(t-z)\sqrt{c^2-z^2}} = 0, \qquad |t| < |c|$$

Hence, the shape U(x,P) is determined by (9), once half length c is specified.

The normal stress on the plane y = o is xero over range $|x| < c$, but for $|x| > c$ is given by

$$\sigma = \sigma_o^c - P + \sigma^c \tag{10}$$

Substituting for σ_o^c and σ^c from equations (2) and (5) this gives

$$\sigma = -P + \frac{\mu}{2\pi(1-\nu)} \int_{-c_o}^{c_o} \frac{B_o(z) + B(z,P)}{x-z}\, dz \qquad |x| > c$$

or (11)

$$\sigma = -P + \frac{\mu}{2\pi(1-\nu)} \int_{-c_o}^{c_o} \frac{\partial}{\partial z} \frac{[U_o(z) - U(z,P)]}{x-z}\, dz \quad |x| > c$$

where $B(x,P) = U(x,P) = 0$ for $c \leq |x| \leq c_o$.

It should be pointed out that equations (7), (9), and (11) are strictly valid only for single, isolated cracks. As we will see in a later section certain cracks make contact at their centers before completely closing, forming two adjacent cracks. In this case, (7), (9) and (11) apply only before the center makes contact. More general expressions for the multiple crack case are given in appendix A.

Levels of applied stress outside of the range $-P' \leq \sigma \leq 0$ (ie., outside the range $0 \leq P \leq P'$) where $-P'$ is the closing stress (or P' is the closing pressure) require additional care. Crack deformation in tension with respect to the reference state of stress cannot be found unless additional information is given for the stress or strength in the plane $y = o$ for $|x| > c_o$. On the other hand, calculation of the stress and strain fields for levels of compression greater than the crack closing pressure, ie. $P > P'$, are straight forward. The strain field for continued hydrostatic loading after crack closure is the superposition of the uniform hydrostatic strain due to P and the strain due to the distribution of dislocations $B_o(x)$. Likewise the stress field is given by $\sigma_{ij} = -P\delta_{ij} + \sigma_{ij}^c$ where σ_{ij}^c is the stress due to the closed crack. In particular the normal stress on the plane $y = o$ is

$$\sigma_o(x) = -P + \sigma_o^c(x)$$

where σ_o^c is given by equation (2).

Expressions (2) - (11) can be quite difficult to evaluate for arbitrary crack shapes, usually requiring numerical solution. However, a broad class of analytic solutions can almost trivially by found when polynomials are used to express U_o and σ_o^c. In particular, the properties of Chebyshev polynomials simplify considerably the necessary integral relations. Such closed form solutions are useful to quickly assess the effects of various crack features on the properties of rocks. In the remainder of this section a specific method of polynomial solution of the crack problem is didcussed; and two simple illustrative examples of crack closure are presented.

When the crack shape $U_o(x)$ is smooth with tapered ends and continuous derivative $B_o(x)$, the corresponding $\sigma_o^c(x)$, given by equation (2), is continuous and finite over the interval $-c_o \leq x \leq c_o$. We can therefore approximate σ_o^c to arbitrary accuracy over this interval by a polynomial of sufficiently large degree n:

$$\sigma_o{}^c(x) \simeq R_n(x) = \sum_{k=0}^{n} r_k x^k \qquad |x| \leq c_o \tag{12}$$

Where the r_k are constants. (For simplicity we once again assume symmetric cracks.) For computational purposes this polynomial form for $\sigma_o^c(x)$ is a convenient starting point for generating crack solutions, (as well as for other dislocation applications like fault slip). However, it is often necessary or desirable to start with a prescribed crack shape $U_o(x)$. In this case the function σ_o^c can be obtained from equation (2) using a numerical Hilbert transform. Alternatively, the shape $U_o(x)$ can be approximated with some convenient form like

$$U_o(x) \simeq \sqrt{c^2-x^2}\, S_m(x)$$

where $S_m(x)$ is an even polynomial such that the derivative $B_o(\pm C_o) = 0$. The Hilbert transform, equation (2), can then easily be found using equation (16).

With the polynomial form, equation (12), in hand, the relation between applied pressure and crack length, equation (7), becomes

$$P = \frac{1}{\pi} \sum_{\substack{k=0 \\ \text{even}}}^{n} r_k c^k \gamma_k \tag{13}$$

where the constants γ_k are given in Appendix B. Similarly the expression (8) for B(x,p) becomes

$$B(x,P) = \frac{-2(1-\nu)}{\mu}\sqrt{1-\left(\frac{x}{c}\right)^2}\sum_{k=2}^{n} b_n U_{n-1}\left(\frac{x}{c}\right) \qquad |x| \leq c \tag{14}$$

where the $U_n(x)$ are Chebyshev polynomials of the second kind (Hochstrasser, 1964) and the constants b_n are defined in Appendix B. Finally the crack shape U(x,P) is found by integrating equation (14):

$$U(x,P) = \frac{2(1-\nu)}{\mu}\int_{-c}^{x}\sqrt{1-\left(\frac{t}{c}\right)^2}\sum_{\substack{k=2\\ \text{even}}}^{n} b_n U_{n-1}\left(\frac{t}{c}\right)dt \qquad |x| \leq c \tag{15}$$

In order to find the normal stress on $y = 0$ outside of the crack opening this expression for B is substituted into (5) and (10):

$$\sigma = \sigma_o^c - P - \frac{1}{\pi}\int_{-c}^{c}\frac{\sqrt{1-\left(\frac{z}{c}\right)^2}}{x-z}\sum_{\substack{k=2\\ \text{even}}}^{n} b_n U_{n-1}\left(\frac{z}{c}\right)dz \qquad |x| > c \tag{16}$$

The last term in (16) is given by

$$\operatorname{sgn}(x)\left[\sqrt{\left(\frac{x}{c}\right)^2-1}\sum_{\substack{k=2\\ \text{even}}}^{n} b_n U_{n-1}\left(\frac{x}{c}\right) - Q(x)\right] \qquad |x| > c$$

where Q(x) is an polynomial obtained by expanding $\sqrt{(x/c)-1}$ as a polynomial in x, multiplying term by term with $\Sigma b_n U_{n-1}(x/c)$, and discarding all negative powers of x (Muskhelishvilli, 1953, p. 253). The same technique is used to find $\sigma_o^c(x)$ for $|x|>c_o$.

To illustrate some important features of nonsingular crack closure two simple crack shapes are now computed. Consider a crack of the form

$$U_o(x) = 2b[1 - (\frac{x}{c_o})^2]^{3/2} \tag{17}$$

where c_o is the crack half length and b is the maximum half width. From equation (2) the stress $\sigma_o^c(x)$ is computed:

$$\sigma_o{}^c(x) = -\frac{3\mu b}{\pi(1-\nu)c_o} \int_{-c_o}^{c_o} \frac{z}{c} \frac{\sqrt{1-(z/c_o)^2}}{x-z} dz$$

Integrals of this form can be evaluated by expressing the polynomial factor in the integrand in terms of Chebyshev polynomials U_n and using equation (B-5) (see Appendix B).

Hence σ_o^c becomes

$$\sigma_o{}^c(x) = \frac{-3\mu b}{2(1-\nu)c_o} [2(\frac{x}{c_o})^2 - 1] \qquad |x| \leq c$$

which is of the convenient polynomial form given by equation (12). Substituting this expression into (13) we obtain the relation between applied pressure P and crack length c:

$$P = \frac{-3\mu b}{2(1-\nu)c_o} [(\frac{c}{c_o})^2 - 1]$$

or

$$c = c_o[1 - \frac{2(1-\nu)c_o}{3\mu b} P]^{1/2} \tag{18}$$

Finally, the deformed crack shape is obtained from equation (15):

$$U(x,P) = 2b(\frac{c}{c_o})^3[1 - (\frac{x}{c})^2]^{3/2} \qquad |x| \leq c \tag{19}$$

From (19) we see that at crack closure , ie., $U \to 0$, the crack length $c \to 0$. Substituting $c = 0$ into (18) we obtain the closing pressure P':

$$P' = \frac{3\mu b}{2(1-\nu)c_o} = \frac{3}{4(1-\nu^2)}\alpha_o E$$

where σ_o is the original aspect ratio b/c and E is Young's modulus This is consistent with the usual rule of thumb that the crack closing pressure is numerically $\sim\alpha_o E$. The exact numerical factor will vary with the crack shape. In comparison, Berg (1965) found that the pressure required to close an elliptical crack of aspect ratio α_o is

$$P_e' = \frac{1}{2(1-\nu^2)}\alpha_o E$$

The ratio of tapered crack closing stress to elliptic crack closing stress for identical aspect ratios is

$$\frac{P'}{P_e'} = \frac{3}{2}$$

Hence, the tapered crack is stiffer than an elliptic crack of the same dimensions, in terms of the closing stress.

The stress on $y = 0$ outside the crack is computed from equation (16):

$$\sigma = \begin{cases} -P'2\left(\frac{c}{c_o}\right)\left(\frac{x}{c_o}\right)\mathrm{sgn}(x)\sqrt{\left(\frac{x}{c}\right)^2-1} & c \le |x| \le c_o \\ -P'2\left(\frac{x}{c_o}\right)\mathrm{sgn}(x)\left[\left(\frac{c}{c_o}\right)\sqrt{\left(\frac{x}{c}\right)^2-1}-\sqrt{\left(\frac{x}{c_o}\right)^2-1}\right] & |x| \ge c_o \end{cases}$$

where -P' is the closing stress.

Figure 2a shows the crack shape, equation (19), plotted for

several levels of applied stress. The most prominant feature of the deformation is the crack shortening accompanying closing. For example, the inner contour (2a) shows the crack at .75 the closing pressure. In this case the crack width is reduced to ~.1 the original width while the crack length is reduced by a half. The relative changes in width and length are described by the aspect ratio α , where $\alpha = U(0,P)/c$ and is obtained from equations (18) and (19):

$$\alpha = \alpha_o \left(\frac{c}{c_o}\right)^2$$

$$= \alpha_o \left(1 - \frac{P}{P'}\right)$$

Here α_o is the original aspect ratio. As suggested by the figure, α decreases (the crack gets flatter) with increasing pressure. Although both U(0,P) and c approach zero with closing, their ratio also goes to zero.

A major consequence of the crack shortening under pressure is the elimination of stress singularities at the crack tips, which occur for example with an infinitesimally thin elliptical crack. Bounded stress concentrations, however, do appear, Figure 2b shows the normal stress on the plane $y = 0$ plotted for several levels of applied stress. For all open cracks the stress over $-c < x < c$ is zero as expected for free surfaces. Over the range $c < x < c_o$, the stress rapidly increases to a peak compressive stress at the original crack tip, greater than the applied pressure. For $|x| > c_o$, the stress falls off and assymptotically approaches the applied stress far from the crack. In each case the stress is quite non-uniform over the closed portions of the crack. This differs substantially from the case of an elliptical crack

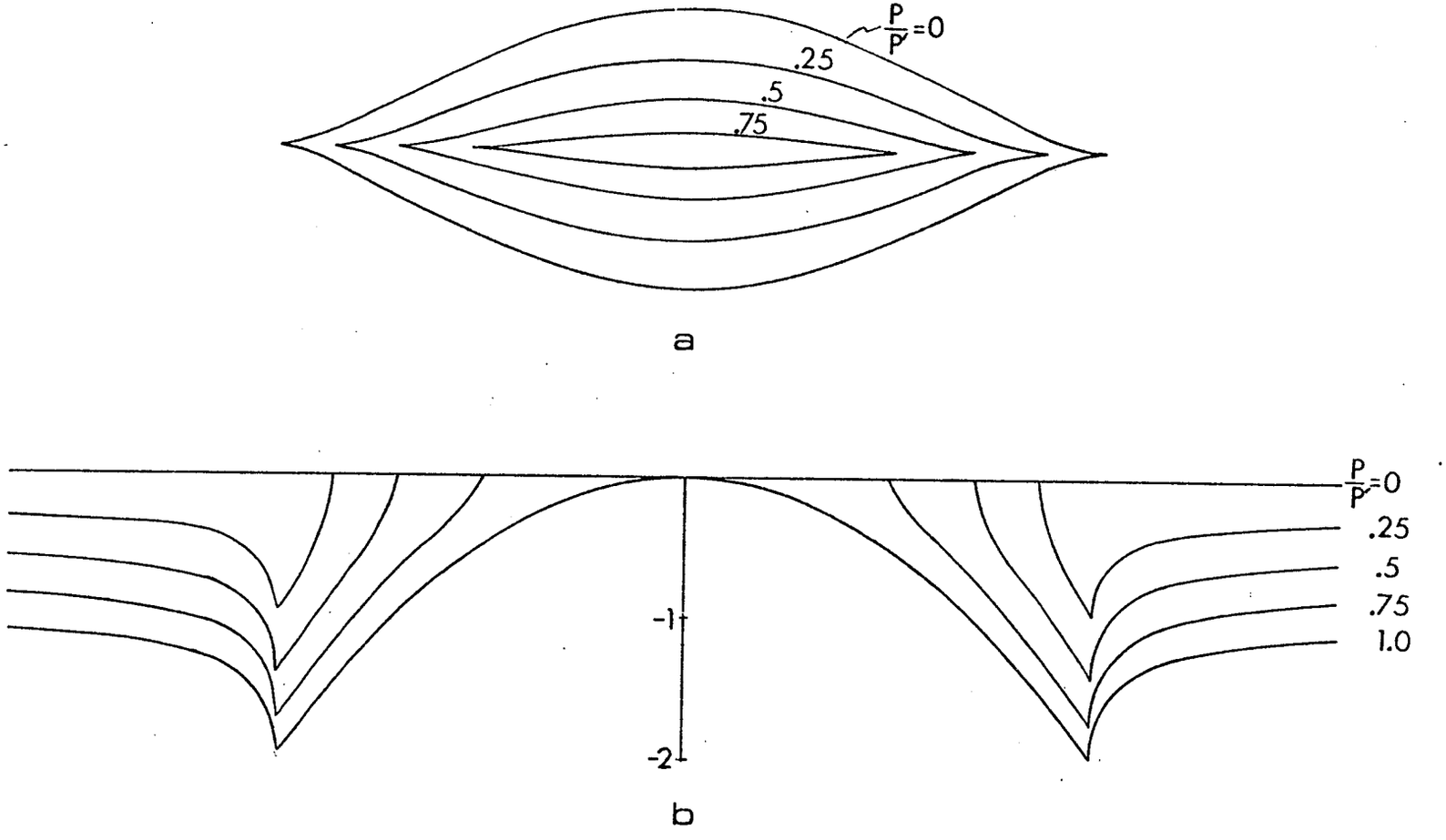

Figure 2. (a) The deformation of a simple crack under several values of applied pressure P. (b) The normal stress in the plane of the crack for the same values of applied pressure.

which does not shorten under pressure. The elliptical crack closes suddenly and uniformly over its whole length at the closing pressure, and the stress over the closed crack is uniform (Berg, 1965).

As a second example consider a crack with shape

$$U_o(x) = 2b[1 - .3(\frac{x}{c_o})^2 - 1.3(\frac{x}{c_o})^4]\sqrt{1-(\frac{x}{c_o})^2}$$

where c_o is the crack half length and b is the maximum crack half width. The dislocation stress corresponding to the closed crack is obtained from equation (2):

$$\sigma_o{}^c(x) = \frac{-10\mu b}{41(1-\nu)c_o}[27(\frac{x}{c_o})^4 - 12(\frac{x}{c_o})^2 + \frac{33}{8}]$$

which is once again in the convenient polynomial form given by equation (12). The relation between applied stress and crack length is given by

$$P = \frac{-\mu b}{(1-\nu)c_o}\frac{10}{41}[\frac{81}{8}(\frac{c}{c_o})^4 - 6(\frac{c}{c_o})^2 - \frac{33}{8}] \qquad (20)$$

Finally, the deformed crack shape is

$$U = \left[\frac{-2b}{41c_o}\ 54(\frac{x}{c_o})^4 + [27(\frac{c}{c_o})^2-40](\frac{x}{c_o})^2 + [-81(\frac{c}{c_o})^4 + 40(\frac{c}{c_o})^2]\right]\sqrt{c^2-x^2} \qquad (21)$$

Figure 3 shows the crack shape, equation (21), plotted for several levels of applied stress. Once again the crack shortens as it closes, although the shortening is slower than in the previous example. In addition, as the applied pressure increases the crack faces touch in the center, forming two adjacent cracks, before completely closing.

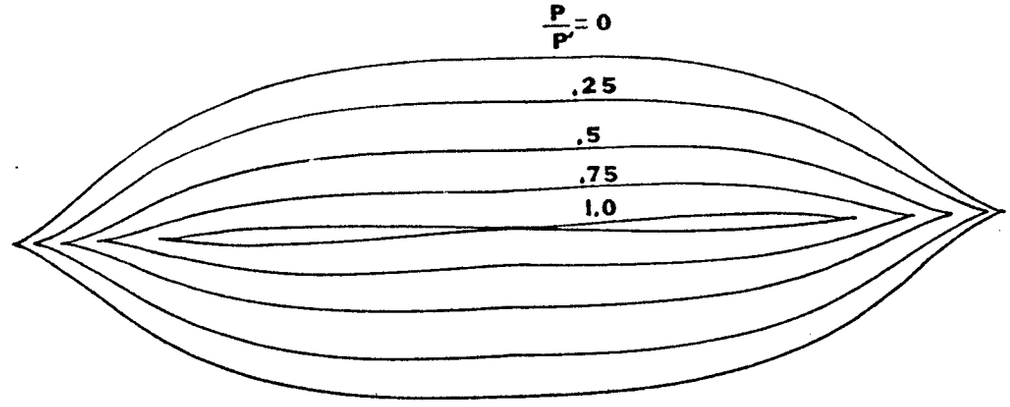

Figure 3. The deformation of a tapered crack which makes contact in its center before completely closing.

The overall crack width at this stage is obtained by setting $x = 0$ in the expression for U in (21) and equating $U = 0$, giving $c = .7c_o$. Using this value in equation (20) the applied pressure causing initial contact is:

$$P' = \frac{1.12\mu b}{(1-\nu)c_o}$$

Deformation beyond initial contact cannot be described with the single-crack expressions (20) and (21). The multiple crack theory outlined in Appendix A can, in principle, be used to extend the results. However, the simple solutions made possbile for single cracks by the Chebyshev polynomials are no longer available. Nevertheless, we expect qualitatively, that the normal stress on the closed portions of the crack will increase from zero at the crack tips to peak stress concentrations at the center as well as the original crack tips with a fall off to the applied stress far from the crack. The central contact should result in an abrupt stiffening of the crack and rock at the contact stress.

Calculation of Bulk Modulus

To find the effective bulk modulus of the porous rock we follow the example of Walsh (1965b) and Jaeger and Cook (1969) and use the Betti-Rayleigh reciprocity theorem. The theorem states that for an elastic body acted upon separately by two sets of tractions, the work done by the first set of tractions acting through the displacements produced by the second set of tractions is equal to the work done by the second set of tractions acting through the displacements produced by the first set of tractions.

To apply the reciprocity theorem, consider the two sets of tractions shown in figure 4. The rock with volume V has a distribution of N non-interacting flat cracks of the type shown in the figure. The system on the left is loaded by an externally applied stress - δP resulting in crack deformation $\delta U(x)$. The crack faces are stress free. (The deformation $\delta U(x)$ is an incremental change in crack shape defined as positive in opening and is given by $\delta U(x) = \delta P \cdot \partial U(x,P)/\partial P)$. The system on the right has the same uniform stress $-\delta P$ applied to both the external surface and the crack faces. In this case the system, at least externally, behaves like a solid block without cracks. Applying the reciprocity theorem we can write

$$\delta P \cdot \frac{\delta P}{K} = \delta P \cdot \frac{\delta P}{K'} + \delta P \sum_{i=1}^{N} d_i \int_{-c_i}^{c_i} \delta U_i(x)\,dx$$

where V is the volume of the rock sample, K is the intrinsic bulk modulus of rock material, K' is the effective bulk modulus of the porous rock and d_i is the crack length into the page of the i^{th} crack. The summation is over all cracks in the rock. Rearranging the equation we obtain

$$\frac{1}{K'} = \frac{1}{K} - \frac{1}{V} \sum_{i=1}^{N} d_i \int_{-c_i}^{c_i} \frac{\delta U_i}{\delta P}\,dx$$

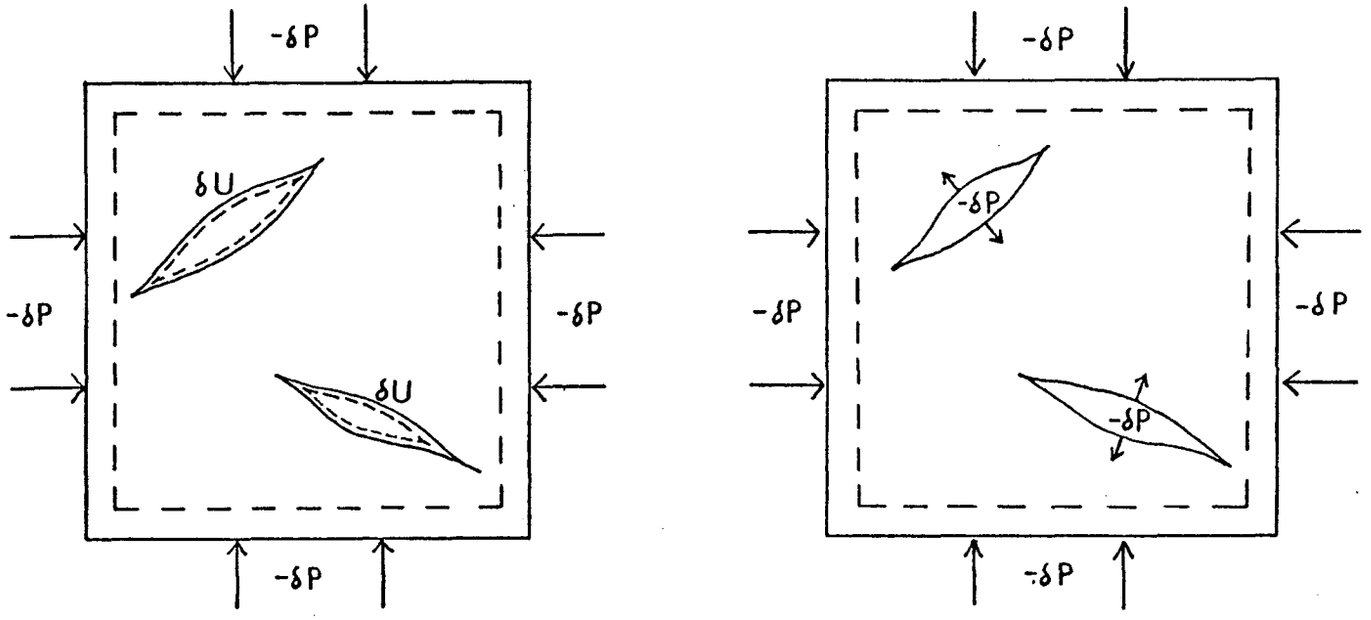

Figure 4. Two sets of applied stresses and the resulting displacements on a rock with a distribution of cracks.

which gives the effective compressibility (equal to the inverse effective bulk modulus) in terms of the crack deformation δU, as found in the previous section. In the limit as $\delta P \to 0$, the effective compressibility becomes:

$$\frac{1}{K'} = \frac{1}{K} - \frac{1}{V} \sum_{i=1}^{N} d_i \int_{-c_i}^{c_i} \frac{\partial U_i(x)}{\partial P} dx \tag{22}$$

Since $U(x,P) = 0$ at $x = \pm c$, the derivative can be taken outside the integral. Hence (22) can be written:

$$\frac{1}{K'} = \frac{1}{K} - \sum_{i=1}^{N} \frac{d_i}{V} \frac{d}{dP} \int_{-c_i}^{c_i} U(x,P)dx \tag{23}$$

As an example, consider the case of a rock containing a distribution of N identical cracks of the form given by equation (17) and plotted in figure 2. To find the compressibility at some level of applied stress P, we compute the derivative

$$\frac{\partial U}{\partial P} = \frac{\partial U/\partial c}{dP/dc}$$

where P and U are given by equations (18) and (19). Therefore:

$$\frac{\partial U}{\partial P} = - \frac{2c(1-\nu)}{\mu} \sqrt{1-\left(\frac{x}{c}\right)^2}$$

Substituting into (23) the compressibility becomes

$$\frac{1}{K'} = \frac{1}{K} + \frac{N}{V} \frac{(1-\nu)}{\mu} \pi c^2 d$$

Or expressing μ in terms of K:

$$\frac{1}{K'} = \frac{1}{K} \left(1 + \frac{2\pi}{3} \frac{(1-\nu^2)}{(1-2\nu)} \frac{Nc^2 d}{V}\right) \tag{24}$$

The effective compressibility given by (24) is a function only of the crack dimensions c and d, and the number of cracks N. In fact this result is exactly the same as for an elliptical two dimensional crack in plane strain with the same dimensions (See for example Walsh, 1965a and Jaeger and Cook, 1969, p. 315). The generality of this result is shown as follows.

Suppose that the rock contains a distribution of non-interacting, arbitrarily shaped flat, non-singular cracks with dimensions c and d. Using equation (3) we can write:

$$\frac{\partial U(x,P)}{\partial P} = -\int_{-c}^{x} \frac{\partial B(z,P)}{\partial P}\, dz - \frac{\partial c}{\partial P} \cdot B(-c,P) \tag{25}$$

$$= \int_{-c}^{x} \frac{\partial B(z,P)}{\partial P}\, dz$$

since $B(\pm c,P) = 0$. It can be shown (Appendix C) for arbitrary (symmetric) flat, tapered cracks that

$$\frac{\partial B}{\partial P} = -\frac{2(1-\nu)}{\pi\mu} \frac{x}{\sqrt{c^2-x^2}} \tag{26}$$

Therefore, substituting (26) into (25) we obtain

$$\frac{\partial U(x,P)}{\partial P} = \frac{-2(1-\nu)}{\mu} \sqrt{c^2-x^2} \tag{27}$$

Finally, using (27) in (22) the compressibility can be written

$$\frac{1}{K'} = \frac{1}{K} + \frac{\pi(1-\nu)}{\mu} \frac{Nc^2d}{V}$$

or expressing μ in terms of ν and K:

$$\frac{1}{K'} = \frac{1}{K}\left(1 + \frac{2\pi}{3} \frac{(1-\nu^2)}{(1-2\nu)} \frac{Nc^2d}{V}\right) \tag{28}$$

Once again the compressibility given by (28) for an arbitrary shape is exactly the same as for a distribution of flat 2-D elliptical cracks in plane strain with the same dimensions. This is a remarkable result which says that although different crack shapes deform and shorten differently under varying levels of hydrostatic stress, the overall compressibility at any given value of stress is independent of crack shape (assuming flat symmetric, non-interacting, non singular, 2-D cracks). Hence, any convenient crack shape, including the ellipse can be used for computing the compressibility in terms of the crack dimensions. However as a consequence, nothing about crack shape can be inferred from the compressibility at a single value of pressure.

DISCUSSION

The derivation of effective compressibility in the previous section is based upon the calculated incremental volumetric strain $d\varepsilon$ resulting from infinitesimal excursions of stress $d\sigma$ about a given hydrostatic load, ie,

$$d\sigma = K' d\varepsilon \tag{29}$$

Such excursions might result, for example, from passing a wave through a statically loaded sample; the incremental modulus would ideally be the local slope of the quasi-static stress-strain loading curve. However, in practice the agreement between static and dynamic modulus is often poor.

To trace out the entire stress-strain curve we substitute the crack dependent effective bulk modulus into equation (29) and integrate:

$$\int_0^{\varepsilon} d\varepsilon = \varepsilon = \frac{1}{K} \int_0^{-P} \left(1 + \frac{2\pi}{3} \frac{(1-\nu^2)}{(1-2\nu)} \sum_i^N \frac{c_i^2 d_i}{V}\right) d\sigma \tag{30}$$

An essential feature of the pennyshaped crack or 2-D elliptical crack model considered by Walsh (1965a) is that while a given crack is open, its length c is independent of stress. Hence over any interval of stress in which no cracks close, the integrand of (30) is a constant and stress-strain relation is linear. If we generalize to non-elliptical shapes, but constrain the crack length to be constant the stress-strain relation remains linear. When the increasing applied pressure reaches the closing pressure of one or a set of elliptical cracks (the closing pressure is determined by the shape and aspect ratio) those cracks suddenly stop contributing to the summation in (30) and the compressibility takes a discontinuous jump. The jump will be small if only one of many cracks close at a time. Hence a distribution of elliptical cracks can give an approximately "continuous" compressibility. In fact with this model the only way to achieve a smoothly varying compressibility is to have a smooth distribution of aspect ratios.

Non-singular cracks, on the other hand, change length with varying stress. Hence, the integrand in (30) is not constant and the stress-strain curve is not linear. Consider, for example, a rock with N identical cracks of the type given by equation (18). Substituting into (30) and integrating we obtain:

$$\varepsilon = \frac{-P}{K} - \frac{\beta}{K} P + \frac{\beta}{2KP'} P^2 \qquad P \leq P' \tag{31}$$

where

$$\beta = \frac{2\pi(1-\nu^2)}{3V(1-2\nu)} N d c_o^2$$

The first term in (31) is just the intrinsic linear compressibility of the rock material. The second term, also linear, makes the rock more compliant and is equivalent to the effect of a distribution of elliptical

cracks of the same original dimensions. The last term makes the rock less compliant and is due to the crack shortening; ie. the modulus at a given pressure depends only on the crack length, so that the crack shortening causes stiffening. Equation (31) is plotted in figure 5 and compared with the linear intrinsic and equivalent elliptical crack curves. At very low stresses, the quadratic term is negligible so the stress-strain curve follows the elliptical crack curve. At larger pressures the quadratic term becomes significant, and the curve deviates substantially from the elliptic crack line. At P'_e the equivalent elliptic cracks close causing an abrupt change in slope of the elliptic curve. If no other cracks were present, the new slope would be the same as the intrinsic. Above P'_e the tapered crack curve continues smoothly to P' where the tapered cracks just close. The slope at P' is equal to the intrinsic slope. Hence there is no abrupt change in modulus at crack closure.

The exact shape of the stress strain curve will differ for different crack shapes. However for any tapered crack we expect the curve to be nonlinear and to take on smoothly the intrinsic slope at crack closure. As a result interpretation or prediction of features like porosity and modulus under varying confining pressure will depend upon the specific crack model chosen. Furthermore the inversion of velocity or modulus data to obtain crack distributions (Simmons et al. 1974, Toksöz et al, 1976) is inherently non-unique.

Under nonhydrostatic conditions cracks under shear, whether partially or totally closed, may undergo frictional sliding at contact points and crack tips. Since the normal stress varies continuously over the crack faces in contact, the frictional stress will also vary. The spatial extent of sliding will depend on the levelof applied shear.

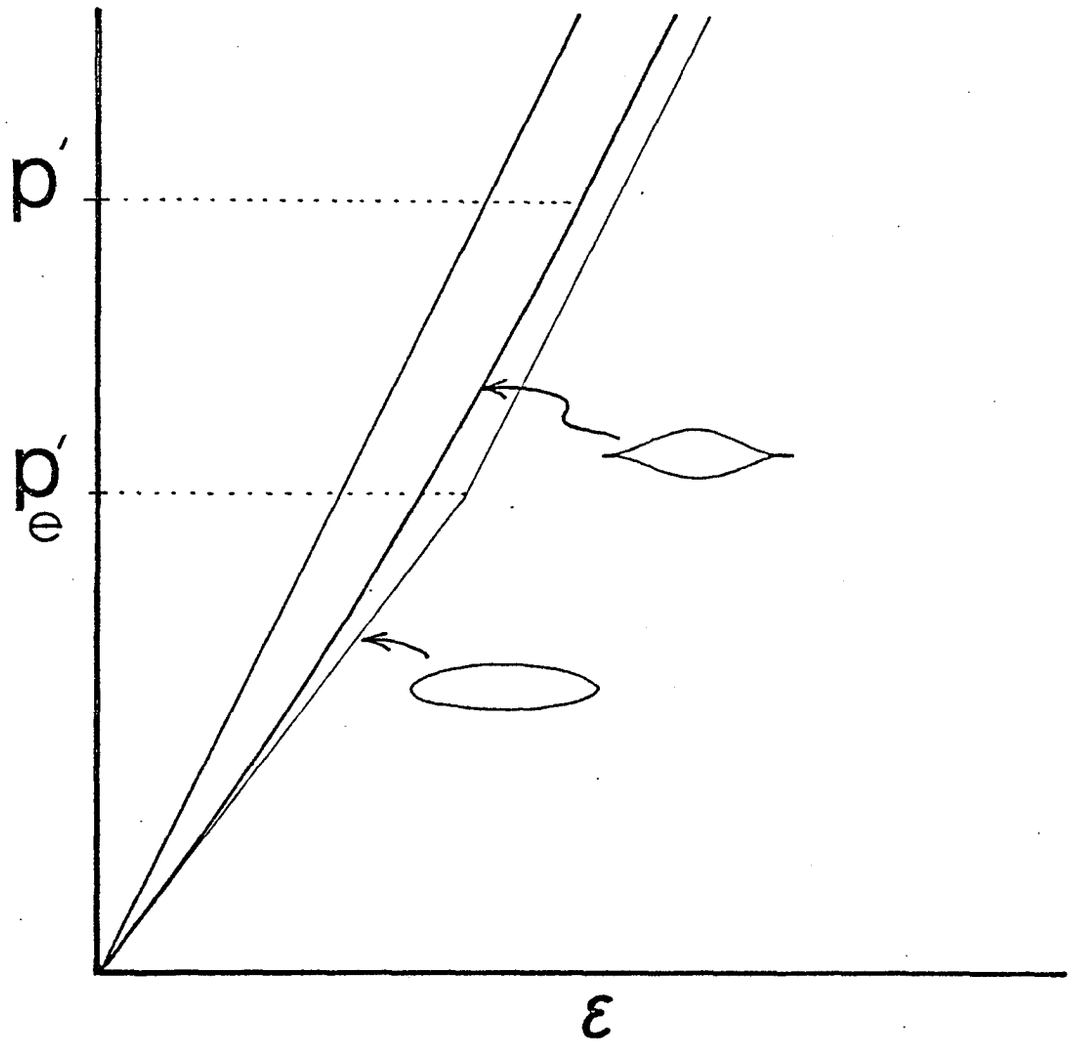

Figure 5. Applied pressure vs. volumetric strain for a rock with a distribution of cracks. The upper curve is for the uncracked rock. The middle curve is for a distribution of identical tapered cracks. The lower curve is for a distribution of identical elliptical cracks with unstressed dimensions equal to those of the unstressed tapered cracks.

Again this differs from the elliptical crack which has frictional sliding only after the crack is completely closed. After closure the frictional stress is uniform across the crack since the normal stress is uniform. For either crack model frictional sliding will produce hysteresis in the stress-strain curve and dissipation of mechanical energy.

The importance of the non elliptic crack model is not only in interpreting the bulk modulus of rock, but also for predicting the closure of cracks with depth in the earth's crust (e.g. Brace, 1975), and the flow of fluids in the cracks. Elliptical cracks close abruptly at confining pressures P_c of the order $P_c = \alpha E$ (e.g. Berg, 1965), where α is the aspect ratio and E is Young's modulus. Consequently it is often suggested that fine cracks cannot exist at depth within the crust, as they are totally closed due to confinement.

This conclusion becomes less obvious when we consider the more realistic non elliptic cracks. Their closure is gradual, and the pressure or depth of closure depends on their unstrained initial shape. It is conceivable for example that some cracks such as joint with somewhat irregular surfaces may never close completely under confining pressure. Instead, only portions of the cracks may close, leaving irregular cavities which are very rigid. Therefore so long as rock in the crust is brittle and sufficiently strong, it should be able to support some connected porosity, to depth of perhaps several kilometers. Finally, the fluid pressure in an elliptic crack, induced by compression of the rock is uniform throughout the crack (Eshelby, 1957). Consequently no flow is induced. Any other crack shape however will produce nonuniform compression, with subsequent fluid flow. Although the magnitude of such flow is not yet clear, it may play a role in attenuation of seismic waves in rock (Mavko and

Nur, 1977). Such an effect does not exist in elliptic cracks.

Conclusion

We have used dislocation theory to study the deformation of rock with flat non elliptical cracks under hydrostatic stress. The general expression for crack shape as a function of pressure has been developed in terms of a triple integral involving the original crack shape and the applied stress. Evaluation of these integrals is particularly simple when the original crack shape is appropriately described in terms of polynomials.

The most prominent feature of the deformation of tapered cracks under compression is crack shortening. A consequence of the shortening is the elimination of stress singularities at crack tips. However bounded stress concentrations do occur. The normal stress on the closed portions of the cracks increases rapidly but continuously from zero at the open face to a peak value at the original crack tip. In contrast a thin elliptic crack simply flattens under compression. The length stays constant until at sufficiently high pressure the crack abruptly closes, making contact simultaneously over the entire crack surface. The stress concentration is unbounded outside the crack tips, and after closure the normal stress is exactly uniform over the closed crack faces.

The compressibility of a rock containing a distribution of arbitrarily shaped flat tapered cracks is exactly the same as for a distribution of flat elliptical cracks with the same lengths. Therefore at a given value of pressure the compressibility is independent of the (2-D) crack model chosen. Consequently nothing about crack shape can be inferred from the compressibility at a single value of pressure. However, at different confining pressures the varying length causes the modulus to vary. As a result interpretation or prediction of features like porosity and modulus

under varying load will depend on the specific crack model chosen.

APPENDIX A

The multiple crack case can be treated following Muskhelishvili (1953, p. 256). Consider a set of coplanar thin cracks with tapered ends, each of the type treated separately in the text of this paper. The original shape of the i^{th} crack is U_{io} with tips at a_{io}, b_{io} as shown in figure A-1. If the hydrostatic stress -P' is applied large enough to close all of the cracks, the normal stress on the plane y = 0 is

$$\sigma_o(x) = -P' + \sigma_o^C(x)$$

where

$$\sigma_o^C(x) = \frac{\mu}{2\pi(1-\nu)} \sum_{i=1}^{N} \int_{a_i}^{b_i} \frac{B_{io}(z)dz}{x-z} \qquad \text{(A-1)}$$

and

$$B_{io}(x) = \frac{d}{dx} U_{io}(x) \qquad \text{(A-2)}$$

If the compression is relaxed to $P < P'$ some of the cracks will reopen over the range $a_i < x < b_i$, where $a_i > a_{oi}$ and $b_i < b_{oi}$, with shape $U_i(x,P)$. The crack opening $U_i(x,P)$ corresponds to a distribution of infinitesimal elastic edge dislocations with density function

$$B_i(x,P) = -\frac{\partial}{\partial x} U(x,P) \qquad \text{(A-3)}$$

The integral equation for B_i expressing the condition of stress-free crack faces is

$$\sum_{i=1}^{N} \int_{a_i}^{b_i} \frac{B_i(z,P)}{x-z}\, dz = \frac{-2\pi(1-\nu)}{\mu} [\sigma_o^C(x)-P] \qquad \text{(A-4)}$$

$$a_i \leq x \leq b_i, \quad i=1,2,3,\ldots.N$$

The conditions that a solution to (A-4) exist with finite stresses everywhere

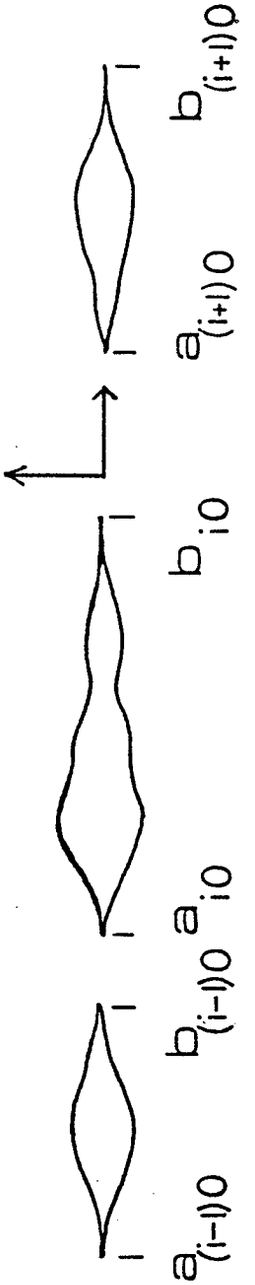

Figure A-1. A set of flat two dimensional coplanar cracks with tapered ends.

is given by:

$$\sum_{i=1}^{N} \int_{a_i}^{b_i} \frac{x^k[\sigma_o{}^c(x)-P]dx}{\left[\prod_{j=1}^{N}(x-a_j)(b_j-x)\right]^{1/2}} = 0 \qquad k = 0,1,2,\ldots,N-1 \tag{A-5}$$

The solution of equation (A-4) is given by:

$$B(x,P) = \frac{2(1-\nu)}{\pi\mu}\left[\prod_{j=1}^{N}(x-a_j)(b_j-x)\right]^{1/2} \sum_{i=1}^{N} \int_{a_i}^{b_i} \frac{\sigma_o{}^c(z) - P}{(x-z)\left[\prod_{j=1}^{N}(z-a_j)(b_j-z)\right]} dz \tag{A-6}$$

$$a_i \leq x \leq b_i \qquad i = 1,2,3,\ldots,N$$

The actual crack shapes are found by integrating $-B(x,P)$:

$$U_i(x,P) = -\int_{a_i}^{x} B(z,P)dz$$

APPENDIX B

Given the polynomial form, equation (12), the expressions for crack length, equation (13) and B(x,P) equation (14) are found as follows. Substituting (12) into (7):

$$P = \frac{1}{\pi} \int_{-c}^{c} \sum_{\substack{k=0 \\ \text{even}}}^{n} \frac{r_k x^k}{\sqrt{c^2-x^2}}\, dx \tag{B-1}$$

or setting $z = x/c$

$$P = \frac{1}{\pi} \sum_{\substack{k=0 \\ \text{even}}}^{n} r_k c^k \int_{-1}^{1} \frac{z^k}{\sqrt{1-z^2}}\, dz = \frac{1}{\pi} \sum_{\substack{k=0 \\ \text{even}}}^{n} r_k c^k \gamma_k \tag{B-2}$$

The integral in (B-2) is given by

$$\gamma_k = \int_{-1}^{1} \frac{}{\sqrt{1-z^2}}\, dz = \begin{cases} \pi & k = 0 \\ 0 & k = 1,3,5,\ldots \\ \frac{k-1}{k} \cdot \frac{k-3}{k-2} \cdots \frac{1}{2}\,\pi & k = 2,4,6,\ldots \end{cases} \tag{B-3}$$

Similarly, substituting (12) into (8) B(x,P) becomes

$$B(x,P) = \frac{2(1-\nu)}{\pi\mu}\sqrt{c^2-x^2} \int_{-c}^{c} \frac{R_n(z) - P}{(x-z)\sqrt{c^2-z^2}}\, dz \qquad |x| \leq c$$

or setting $t = x/c$

$$B(x,P) = \frac{2(1-\nu)}{\pi\mu}\sqrt{1-\left(\frac{x}{c}\right)^2} \int_{-1}^{1} \frac{R_n(ct) - P}{\left(\frac{x}{c} - t\right)\sqrt{1-t^2}}\, dt \qquad |x| \leq c$$

By expanding the polynomial $R_n(ct)$ in terms of Chebyshev polynomials of the first kind, $T_n(t)$:

$$R_n(ct) = \sum_{\substack{k=0 \\ \text{even}}}^{n} b_n T_n(t) \qquad |t| \leq 1 \tag{B-4}$$

the expression B(x,P) can be written as

$$B(x,P) = \frac{2(1-\nu)}{\pi\mu}\sqrt{1-(\frac{x}{c})^2}\left[\sum_{\substack{k=2\\ \text{even}}}^{n} b_n \int_{-1}^{1} \frac{T_n(t)dt}{(\frac{x}{c}-t)\sqrt{1-t^2}} + (b_o - P)\int_{-1}^{1} \frac{dt}{(\frac{x}{c}-t)\sqrt{1-t^2}}\right] \qquad |x| \leq c$$

But

$$\int_{-1}^{1} \frac{T_n(t)dt}{(z-t)\sqrt{1-t^2}} = \begin{cases} -\pi U_{n-1}(z) & n \geq 1 \\ 0 & n = 0 \end{cases} \qquad |z| \leq 1 \qquad \text{(B-5)}$$

$$\int_{-1}^{1} \frac{\sqrt{1-t^2}\, U_{n-1}(t)dt}{z-t} = \pi T_n(z) \qquad |z| \leq 1$$

where the $U_n(x)$ are Chebyshev polynomials of the second kind (Hochstrasser, 1964). Hence B(x,P) becomes simply

$$B(x,P) = \frac{-2(1-\nu)}{\mu}\sqrt{1-(\frac{x}{c})^2}\sum_{\substack{k=2\\ \text{even}}}^{n} b_n U_{n-1}(\frac{x}{c}) \qquad |x| \leq c \qquad \text{(B-6)}$$

APPENDIX C

The independence of compressibility on crack shape is shown as follows. Through algebraic manipulation it can be shown that for symmetric tapered cracks the solution given by equation (8) is equivalent to

$$B(x,P) = \frac{2(1-\nu)}{\pi\mu} \frac{1}{\sqrt{c^2-x^2}} \int_{-c}^{c} \frac{[\sigma_o{}^c(z)-P]\sqrt{c^2-z^2}}{x-z}\, dz \qquad \text{(C-1)}$$

Differentiating we obtain

$$\frac{\partial B}{\partial P} = \frac{2(1-\nu)}{\pi\mu} \left[\frac{-c(\partial c/\partial P)}{(c^2-x^2)^{3/2}} \int_{-c}^{c} \frac{[\sigma_o{}^c(z)-P]\sqrt{c^2-z^2}}{x-z}\, dz \right.$$

$$\left. - \frac{1}{\sqrt{c^2-x^2}} \int_{-c}^{c} \frac{\sqrt{c^2-z^2}}{x-z}\, dz + \frac{\partial c/\partial P}{\sqrt{c^2-x^2}} \int_{-c}^{c} \frac{(\sigma_o{}^c(z)-P)c}{(x-z)\sqrt{c^2-z^2}}\, dz \right]$$

Using both (8) and (C-1) this can be written:

$$\frac{\partial B}{\partial P} = \frac{-c}{c^2-x^2} B(x,P) \frac{\partial c}{\partial P} - \frac{2(1-\nu)}{\pi\mu\sqrt{c^2-x^2}} \int_{-c}^{c} \frac{\sqrt{c^2-z^2}}{x-z} + \frac{c}{c^2-x^2} B(x,P) \frac{\partial c}{\partial P}$$

$$= \frac{-2(1-\nu)}{\pi\mu\sqrt{c^2-x^2}} \int_{-c}^{c} \frac{\sqrt{c^2-z^2}}{x-z}\, dz \qquad \text{(C-2)}$$

The integral in (C-2) can be evaluated to give

$$\frac{\partial B}{\partial P} = \frac{-2(1-\nu)}{\pi\mu} \frac{x}{\sqrt{c^2-x^2}} \qquad |x| < c \qquad \text{(C-3)}$$

References

Berg, C.A., Deformation of fine cracks under high pressure and shear, J. Geophys. Res., 70, 14, 3447, 1965.

Bilby, B.A. and J.D. Eshelby, Dislocations and the theory of fracture, in Fracture An Advanced Treatise, edited by H. Liebowitz, Vol. II, p. 99, Academic Press, New York, 1968.

Birch, F., The velocity of compressional waves in rocks to 10 kilobars, J. Geophys. Res., 65, 1083, 1960.

Brace, W.F., Some new measurements of linear compressibility of rocks, J. Geophys. Res., 70, 391, 1965.

Brace, W.F., Dilatancy related electrical resistivity changes in rocks, Pure and Applied Geophysics, 113, 207-217, 1975.

Delameter, W.R., Weakening of elastic solids by arrays of cracks, Ph.D. Dissertation, Dept. of Applied Mechanics, Stanford University, 1974.

Eshelby, J.D., The determination of the elastic field of an ellipsoidal inclusion, and related problems, Proc. Roy. Soc. London, A, 241, 376, 1957.

Hochstrasser, U.W., Orthogonal polynominals, in Handbook of Mathematical Functions, edited by M. Abramowitz and I.A. Stegun, p. 771, Dover Publications, Inc., New York, 1964.

Jaeger, J.C. and N.G.W. Cook, Fundamentals of Rock Mechanics, Methuen & Co. Ltd., 1969.

Kuster, G.T. and M.N. Toksöz, Velocity and attenuation of seismic waves in two-phase media: part I. Theoretical formulations, Geophysics, 39, 5, 587, 1974.

Mavko, G.M. and A.M. Nur, Wave attenuation in partially saturated rocks, in review for Geophysics, 1977.

Muskhelishvili, N.I., Singular Integral Equations, edited by J.R.M. Radok, P. Noordhoff Ltd., Groningen, Holland, 1953.

Nur, A., Effects of stress on velocity anisotropy in rock with cracks, J. Geophys. Res., 76, 8, 2022, 1971.

O'Connell, R.J., and B. Budiansky, Seismic velocities in dry and saturated cracked solids, J. Geophys. Res., 79, 35, 5412, 1974.

Simmons, G., R.W. Siegfried II, and M. Feves, Differential strain analysis: a new method for examining cracks in rocks, J. Geophys. Res., 79, 29, 4383, 1974.

Toksöz, M.N., C.H. Cheng, and A. Timur, Velocities of seismic waves in porous rocks, Geophysics, 41, 4, 621, 1976.

Walsh, J.B., The effect of cracks on the compressibility of rock, J. Geophys. Res., 70, 2, 381, 1965a.

Walsh, J.B., The effect of cracks on the uniaxial elastic compression of rocks, J. Geophys. Res., 70, 2, 399, 1965b.

CHAPTER 6

WAVE ATTENUATION IN PARTIALLY SATURATED ROCKS

The velocity and attenuation of seismic waves in crustal materials are strongly dependent upon pore fluid content and the details of pore geometry. The degree of wave interaction with fluids is in general determined by the shape, and hence compliance, of the pores within the solid matrix of mineral grains. Rocks with flatter pores are more sensitive to the details of the fluid and its ability to support or transmit compressional and shear loads; rounder, more rigid pores are less sensitive to the presence of fluids. In the low frequency limit pore fluids influence the system through their density, compressibility, and distinct lack of rigidity; at higher frequencies viscous and inertial interactions are introduced.

This dependence of velocity and attenuation on pore geometry and fluid properties can, in principle, serve as a diagnostic of material structure both in situ and in the laboratory. Nur (1971) and Solomon (1972), using equations from Walsh (1969), made estimates of upper mantle partial melt configuration from the velocities of teleseismic compressional and shear waves. Related experimental work on the dependence of velocity on partial melt was reported by Anderson and Spetzler (1970). Nur (1973) interpreted observed temporal velocity anomalies as diagnostic of dilatant strain and varying pore water saturation in the crust prior to certain earthquakes.

In exploration geophysics, a substantial effort has been made to develop more detailed theoretical and experimental correlations between longitudinal wave velocities, rock type and fluid content in the shallow crust. The goal in oil and gas exploration is to be able to distinguish reliably between gas, oil, and water in situ, as well as to infer their relative concentrations, rock type, porosity and permeability. Similar problems in geothermal exploration concern assessing water and steam content, as well as permeability and state of fracture.

Work by Domenico (1974), Kuster and Toksoz (1974a, b) and Elliott and Wiley (1975) indicates that the velocity of a liquid-saturated rock can differ substantially from that in the same rock with a partial saturation of a free gaseous phase. The two rocks in contact can account for a large reflection coefficient and an observed "bright spot." However, the dependence of velocity on the amount of gas saturation is very weak over the range 10 to 90 percent. The contrast in velocity is an indicator of gas, but a poor quantitative measure of economic value.

In this chapter we present a model of one particular mechanism for wave attenuation in partially saturated liquid-gas systems. The model predicts that for certain rocks with at least a small concentration of very flat pores, even a small amount of water can dramatically enhance the dissipation of energy of compressional waves. Furthermore, the level of attenuation is directly dependent on the actual concentrations of liquid and gas, as well as on the fluid viscosity and pore shape. This can in principle serve as an independent data point on the state of saturation of porous rocks. However not enough data are presently available to adequately test the model.

In the first section that follows we will discuss some general considerations of fluid attenuation and introduce our model of partial saturation. In the second section mathematical formulas are derived for calculating attenuation of compressional waves. The remainder of the paper gives a discussion of the model results including simplified expressions for attenuation for specific pore geometries, limiting expressions at high and low frequencies, and comparison with other models of fluid attenuation.

Fluid Attenuation

The primary source of fluid attenuation in porous media (ignoring nonmechanical effects) is relative motion between the solid and liquid. Such motion results in shearing stresses in the fluid and, consequently, viscous dissipation of mechanical energy. In our model of attenuation we examine the details of flow and energy dissipation on the scale of the individual pores. We approximate the rock as an isotropic elastic solid containing a distribution of randomly oriented, partially saturated cracks or pores of the type shown schematically in figure 1. We assume that the liquid is segregated into one or more discrete "drops" within each pore that flow as the pore is deformed. For mathematical convenience the separate pores are treated as two-dimensional cracks in plane strain with width, d, (into the page) equal to some function of the half-length, c. Furthermore, the separate pores are assumed not to interact, and only flat cracks with aspect ratio $\alpha_c < 0.1$ are considered (where $\alpha_c = a_0/c$ and a_0 is the maximum pore half width in the plane of the page). Rigorously, this might limit our applications to low porosity igneous rocks. However,

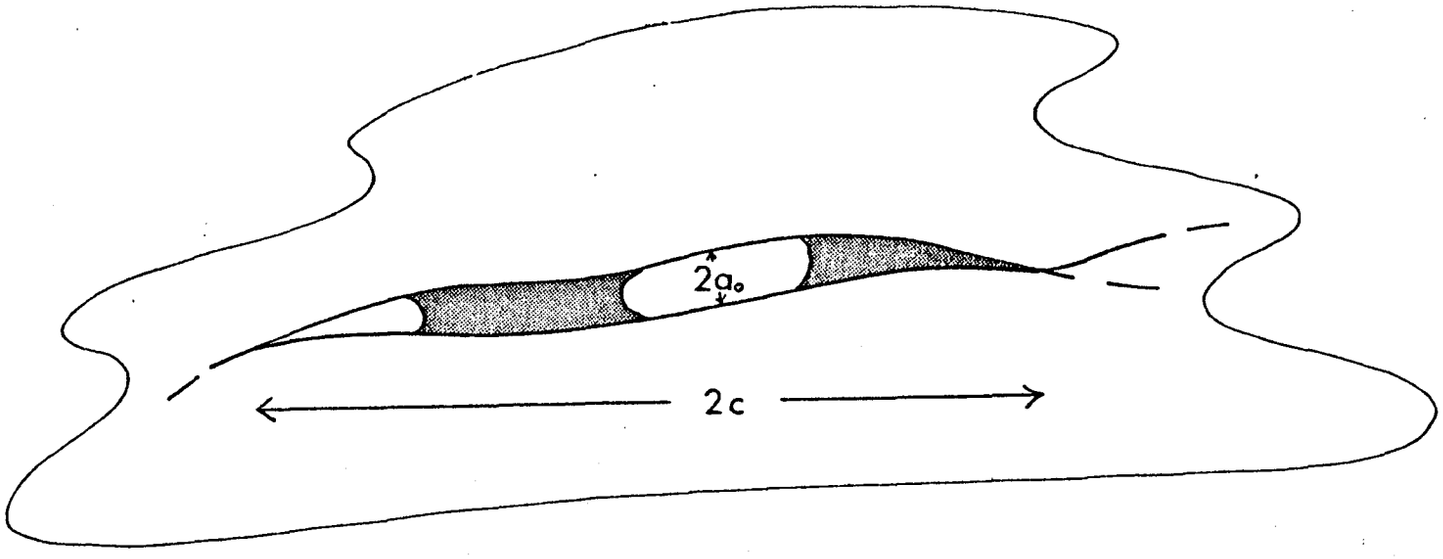

Figure 1. Schematic view of partially saturated, two dimensional pore. Thickness of pore into page is set equal to d to approximate the third dimension.

conceptually, the notions of dissipative flow that we will develop are quite applicable to more closely spaced, equidimensional pores. We will also find that flat pores give a much larger effect than the same volume of equant pores.

Our treatment of the details of flow in the individual pores will be reminiscent of Biot's (1956a, b) for the general porous solid except for the emphasis here on undersaturation. In this study, details of pore geometry will be retained, and both high and low frequencies are addressed.

Mathematical Derivation: Longitudinal Waves

A longitudinal (compressional) wave passing through our material exerts oscillatory stresses which can be resolved into normal and shear components in the plane of each pore. In this section we find the attenuation resulting from the normal component of excitation on the individual pore; a later section treats the shear component. For a given wave and distribution of crack orientations the total attenuation can then be found from a summation of both components over all pores. We will find, in fact, that the shear component of dissipation resulting from either compressional or shear waves gives a negligible contribution for most cases of interest involving water.

Seismic attenuation is estimated for a given fluid geometry by solving for the specific dissipation function Q^{-1} of the fluid-elastic composite, given by:

$$Q^{-1} = \frac{\Phi}{2\pi W}$$

where Φ is the energy dissipated in the fluid phase during one cycle of

sinusoidal oscillation and W is the peak energy stored during the same cycle. The spatial attenuation function can then be found from:

$$\alpha_x = \frac{\omega}{2C_p Q}$$

where α_x is the attenuation coefficient for plane wave amplitude decay with propagation and C_p is the compressional phase velocity at frequency ω. The method of solution will be to solve for the fluid flow field in each single partially filled pore resulting from a prescribed oscillation of the pore walls. The elastic energy of the rock surrounding the pore will then be obtained for the same oscillation.

For this study pore geometries are limited to long narrow two-dimensional cracks as shown in figure 1. Surface tension is neglected except for the assumption that during seismic oscillation, each fluid drop remains intact rather than breaking up into smaller drops or losing contact with one or both of the pore walls. Because the pores are undersaturated the flow is incompressible for most frequencies and geometries of interest (see appendix A). Furthermore, by assuming that the crack half width a(x) is a slowly varying function of x, the flow is essentially one-dimensional for small oscillations of the pore walls about the static position. Hence the approximate equation of motion governing the fluid flow reduces to

$$\rho \frac{\partial u}{\partial t} = - \frac{\partial P}{\partial x} + \eta \frac{\partial^2 u}{\partial y^2} \qquad (1)$$

where u is the x-component of velocity, ρ is the density, η is the viscosity and P is the pressure of the fluid. (A discussion of the assumptions involved in obtaining the equation of motion (1) is given in appendix A.)

The boundary conditions for the fluid are stated in terms of pore wall displacements (see fig. 2). For very small strains, the pore half width $\tilde{a}(x,t)$ is assumed to oscillate about the static shape $a(x)$ as

$$\tilde{a}(x,t) = a(x)[1 + \varepsilon e^{i\omega t}] \tag{2}$$

where $\varepsilon << 1$. Although the motion in (2) is in the y direction, the y-component of fluid velocity is neglected in the 1-D approximation. However, the oscillation in (2) results in a volumetric oscillation which causes a pressure gradient and a lateral displacement or flow of the fluid.

At any station, x, with local pressure gradient $\frac{\partial P}{\partial x}$, the solution of equation (1) for (approximately) parallel-plate flow is given by

$$u(x,y) = \frac{-\partial P(x)}{\partial x} \frac{1}{i\omega\rho}\left[1 - \frac{\cosh(\sqrt{\frac{i\omega}{\nu}}\, y)}{\cosh(\sqrt{\frac{i\omega}{\nu}}\, a(x))}\right] \quad ,\nu = \eta/\rho \tag{3}$$

The weak x-dependence is contained in $P(x)$ and $a(x)$. The explicit time dependence is dropped here and in the remaining derivation since all quantities go as $e^{i\omega t}$. Since the flow is incompressible, the net flow at x must be equal to the rate of change of volume $\dot{A}(x)$ of the portion of the pore to the right of x. Hence

$$\int_{-a(x)}^{a(x)} u(x,y)\,dy = -\dot{A}(x) \tag{4}$$

and we can solve for the pressure gradient from (3) and (4):

$$\frac{\partial P(x)}{\partial x} = \dot{A}(x) \frac{i\omega\rho}{2a\left[1 - \frac{1}{a}\sqrt{\frac{\nu}{i\omega}} \tanh\sqrt{\frac{i\omega}{\nu}}\, a\right]} \tag{5}$$

where

$$\dot{A}(x) = 2\int_0^x \frac{\partial}{\partial t}\tilde{a}(x,t)\,dx.$$

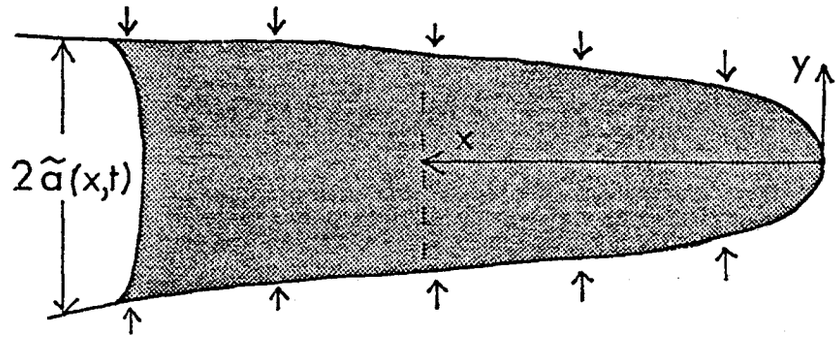

Figure 2. Liquid drop subject to oscillations of pore walls.

By combining (3) and (5) the flow field is obtained:

$$u(x,y) = \frac{-\dot{A}(x)}{2a(x)} \cdot \frac{1 - \dfrac{\cosh\sqrt{\dfrac{i\omega}{\nu}}\, y}{\cosh\sqrt{\dfrac{i\omega}{\nu}}\, a}}{1 - \dfrac{1}{a}\sqrt{\dfrac{\nu}{i\omega}}\tanh\sqrt{\dfrac{i\omega}{\nu}}\, a} \tag{6}$$

The energy dissipation Φ for the entire pore during one cycle is found by solving for the shear stress $\tau = \eta \frac{\partial u}{\partial y}$, and integrating the energy dissipation density over the period and the volume of fluid:

$$\Phi = \int_V \int_T \frac{1}{2\eta} \tau\cdot\tau^* dt dV$$

$$= \frac{3}{2}\frac{\pi\eta d}{\omega} \int_0^D \frac{\dot{A}\dot{A}^*}{a^3(x)} R(z)dx \tag{7}$$

where * means complex conjugate and R(x) is given in appendix B.

To find the peak elastic energy stored in the rock during oscillation of the pore we use the Betti-Rayleigh reciprocity theorem. The theorem states that for a body acted upon separately by two sets of tractions, the work done by the first set of tractions acting through the displacement produced by the second set of tractions is equal to the work done by the second set of tractions acting through the displacements produced by the first set of tractions.

In the derivation that follows we divide the rock into elements of volume, each containing a single pore. A uniform traction is applied to the boundary of each volume equal to the peak stress from the propagating wave. For cracks oriented at some arbitrary angle with the direction of propagation the applied traction can be resolved into normal and shear components of stress in the plane of the crack. The crack compression from the normal component results in the fluid flow and attenuation derived above. The crack shearing from the shear

component of stress results in the flow problem to be treated in a later section. (In most cases of interest the shear dissipation will be negligible.) To find the stored energy, W, for the arbitrarily oriented crack both components of stress must be considered. Jaeger and Cook (1969, p. 313) show in detail how this energy varies with orientation for the simple case of a dry crack and how to sum over a random distribution of orientations. In our problem the crack has a nonuniform internal fluid pressure distribution given by equation (5) which will modify the energy W from the simple dry case. We will only solve for the case of cracks perpendicular to the plane-wave propagation, in order to determine the first-order fluid effects on propagation. However, in principle, variation with orientation can be found by repeating the derivation which follows, keeping careful note of the resolved components of stress, in a fashion analogous to Jaeger and Cook. We expect that this would result in only a small perturbation on our results.

Walsh (1965a, b) discusses the difficulties and uncertainties associated with choosing the uniform stress vs. a uniform strain boundary condition, as well as the difference between the penny-shaped crack and a two-dimensional crack in plane strain or plain stress. He concludes, as we do, that the differences resulting from these various assumptions are negligible compared to the overall level of approximation in the analysis.

To apply the reciprocity theorem, consider the two sets of tractions shown in figure 3. The system on the left is loaded by an externally applied stress corresponding to the peak stress of the seismic wave. The pore wall displacement $s(x)$ is due to both the external stress σ,

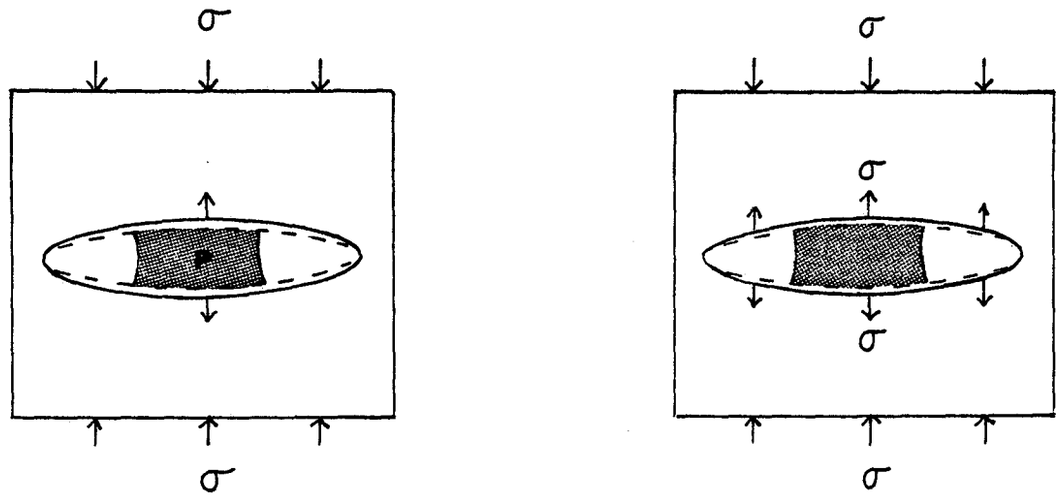

Figure 3. Applying the reciprocity theorem to a rock under two sets of applied stress. On the left only the induced pore pressure is applied to the pore. On the right the applied stress σ is applied to the pore making the rock deform as though uncracked.

tending to close the crack, and the instantaneous internal fluid pressure distribution P(x) tending to keep the crack open. The system on the right has the same external stress σ applied to both the external and internal surfaces. In this case the system, at least externally, behaves like a solid block without the cavity or fluid. Applying the reciprocity theorem we can write

$$-2d \int_{-c}^{c} P(x) \frac{\sigma}{M} a(x)dx + \sigma \frac{\sigma}{M} V = \sigma \frac{\sigma}{M'} V - 2\sigma d \int_{-c}^{c} S(x)dx \qquad (8)$$

where V is the volume of the block, M is the elastic modulus of the solid rock, M' is the effective elastic modulus of the rock-fluid system and the dimensions c and d are as given in figure 1. The integral on the left is negligibly small and can be dropped (see appendix D). For the case of plane wave propagation of a compressional wave, $M = \lambda + 2\mu$ where μ is the shear modulus and λ is Lame's coefficient for the intrinsic rock material. Rearranging equation (8) we get:

$$\frac{1}{2} \frac{\sigma^2 V}{M'} = \frac{1}{2} \frac{\sigma^2}{M} V + \sigma d \int_{-c}^{c} S(x)dx \qquad (9)$$

$$W = W_o + W_p$$

The first term on the left is recognized as the total strain energy of the composite system W, which we are seeking. The terms on the right are the strain energy W_o of a comparable rock without porosity, plus the energy contribution W_p due to the presence of the pore. In order to relate the displacement S(x) to the applied stress σ it is convenient to consider a crack with uniform pore pressure $\bar{P}$ (see appendix C). For very small stresses σ and $\bar{P}$ (as for a wave) the resulting small pore displacement and its integral W_p can be written as

$$S(x) \cong \frac{2(\sigma-\bar{P})c(1-\xi^2)}{E}\sqrt{1-(\frac{x}{c})^2} \tag{10}$$

$$W_p \simeq \frac{\pi\sigma(\sigma-\bar{P})c^2 d(1-\xi^2)}{E} \tag{11}$$

where ξ is Poisson's ratio, E is Youngs modulus and $\bar{P}$ is a uniform pore pressure. With nonuniform pressure P(x) the energy W_p can still be written in the form (11) if the pressure $\bar{P}$ is chosen as

$$\bar{P} = \frac{2}{\pi}\int_{-c}^{c} \frac{P(x)[(\frac{x}{c})^2-(\frac{x}{c})]}{c^2-x^2}\,dx \tag{12}$$

where P(x) is obtained by integrating equation (5) (see appendix C). Setting $S(0) \simeq a_0\varepsilon$ we can solve for σ in terms of $\bar{P}$ and ε or $\sigma = \bar{P} + \varepsilon\alpha_c E/2(1-\xi^2)$. Finally, combining this with equations (9) and (11) and setting $\lambda = \mu$ and $\xi = 1/4$ we arrive at the total strain energy in terms of ε and $\bar{P}$:

$$W = \frac{8}{27}\mu V\alpha_c{}^2\varepsilon^2(1+\frac{9}{4}\frac{\psi}{\alpha_c}) + \frac{\mu V}{6}(\frac{\bar{P}}{\mu})[\frac{8}{3}\alpha_c\varepsilon(1+\frac{9}{8}\frac{\psi}{\alpha_c}) + (\frac{\bar{P}}{\mu})] \tag{13}$$

Here ψ is the porosity and α_c is the crack aspect ratio.

The specific dissipation function Q^{-1} can now be given by combining equations (7) and (13)

$$Q^{-1} = \frac{\Phi}{2\pi W} = \frac{\frac{3}{2}\pi\eta\frac{d}{\omega}\int_0^D \frac{\dot{A}\dot{A}^* R(z)}{a^3(x)}dx}{\frac{8}{27}\mu V\alpha_c{}^2\varepsilon^2(1+\frac{9}{4}\frac{\psi}{\alpha_c})+\frac{\mu V}{6}(\frac{\bar{P}}{\mu})[\frac{8}{3}\alpha_c\varepsilon(1+\frac{9}{8}\frac{\psi}{\alpha_c})+(\frac{\bar{P}}{\mu})]} \tag{14}$$

Results: The Parallel-Walled Pore

Consider the specific example of a pore where a(x) is approximately a constant (i.e. $a(x) = a_0$) over the region occupied by the drop of length 2D. Here R(z), where $z = a(x)\sqrt{\omega/2\nu}$, is independent of x, and

$\dot{A}(x) = +2x\varepsilon a_0 i\omega e^{i\omega t}$. Equation (7) can easily be evaluated to give the energy dissipated per cycle:

$$\Phi = \frac{4\pi\eta\omega d\varepsilon^2 D^3}{a_0} R(z) \tag{15}$$

The pressure distribution P(x) is obtained by integrating equation (5) and taking the real (in phase) part:

$$P(x) = \mathrm{Re} \int \frac{\partial P}{\partial x}\, dx = \frac{\omega^2 \varepsilon \rho}{2} (D^2 - x^2) Y(z) \tag{16}$$

where Y(z) is given in appendix B. Using equation (12) we get finally the equivalent uniform pressure $\overline{P}$ that appears in the formula for W:

$$\overline{P} = \frac{\omega^2 \varepsilon \rho}{2\pi} c^2 \gamma Y(z) \tag{17}$$

where γ is also given in appendix B. The attenuation Q^{-1} can be found by replacing these simplified forms in equation (14).

A plot of Q^{-1} vs. z and ω for the parallel walled pore is given in figure 4. The most striking feature is the sharp peak at $\omega = \omega_o$, and the rapid fall off at both high frequencies, where $Q^{-1} \simeq \omega^{-5/2}$, and low frequencies, where $Q^{-1} \simeq \omega$. This high frequency result must be used with caution since for certain geometries the assumption of incompressibility (appendix A) is violated before such high frequencies are achieved. For most applications however the frequencies of interest are well within safe bounds.

Let us examine more closely the asymptotic behavior. Table 1 gives the high and low frequency forms of Φ, P, W, and Q^{-1} based on the limiting forms of R(z) and Y(z). The new parameters are β, the volume concentration of liquid in the rock and $\alpha_f = a_o/D$, the aspect ratio of the drop.

Table 1

	$\omega \ll \frac{2\nu}{a^2}$ (Poisseuille)		$\omega \gg \frac{2\nu}{a^2}$ (inertial)	
	$\omega \ll \frac{8\pi\mu\alpha_c^3}{\eta}$	$\omega \gg \frac{8\pi\mu\alpha_c^3}{\eta}$	$\omega \ll \frac{8\pi\mu\alpha_c^3}{\rho a_o^2}$	$\omega \gg \frac{8\pi\mu\alpha_c^3}{\rho a_o^3}$
R	1		$\frac{a_o}{3}\ \frac{\omega}{2\nu}$	
Y	$\frac{9}{16}\frac{\eta}{\rho\omega a_o^2}$		1/2	
Φ	$\frac{\pi\eta\varepsilon^2\nu\omega}{\alpha_f^2} \propto \omega$		$\frac{4\pi\eta\omega\varepsilon^2 D^3 d}{a_o}\ \frac{a_o}{3}\ \frac{\omega}{2\nu} \propto \omega^{3/2}$	
P(x)	$\frac{9}{32}\frac{\eta\varepsilon\omega}{a_o^2}(D^2-x^2)$		$\frac{\varepsilon\rho\omega^2}{4}(D^2-x^2)$	
W	$\frac{8}{27}\mu V\alpha_c^2\varepsilon^2(1+\frac{9}{4}\frac{\psi}{\alpha_c})$	$\frac{V}{6\mu}\ \frac{9}{32\pi}\frac{\omega\eta\varepsilon\gamma}{\alpha_c^2}^2 \propto \omega^2$	$\frac{8}{27}\mu V\alpha_c^2\varepsilon^2(1+\frac{9}{4}\frac{\psi}{\alpha_c})$	$\frac{V}{6\mu}\ \frac{\omega^2\varepsilon\rho c^2\gamma}{4\pi}^2 \propto \omega^4$
Q^{-1}	$\frac{27}{16}\frac{\eta\omega\beta}{\mu\alpha_c^2\alpha_f^2(1+\frac{9}{4}\frac{\psi}{\alpha_c})} \propto \omega$	$\frac{37.9\pi^2\mu\beta\alpha_c^4}{\omega\eta\gamma^2\alpha_f^2} \propto \omega^{-1}$	$\frac{9}{4}\frac{\eta\omega\beta a_o}{\mu\alpha_f^2\alpha_c^2(1+\frac{9}{4}\frac{\psi}{\alpha_c})}\ \frac{\omega}{2\nu} \propto \omega^{3/2}$	$\frac{16\pi^2\mu\eta\beta a_o}{\gamma^2\rho^2\omega^3\alpha_f^2 c^4}\ \frac{\omega}{2\nu} \propto \omega^{-5/2}$

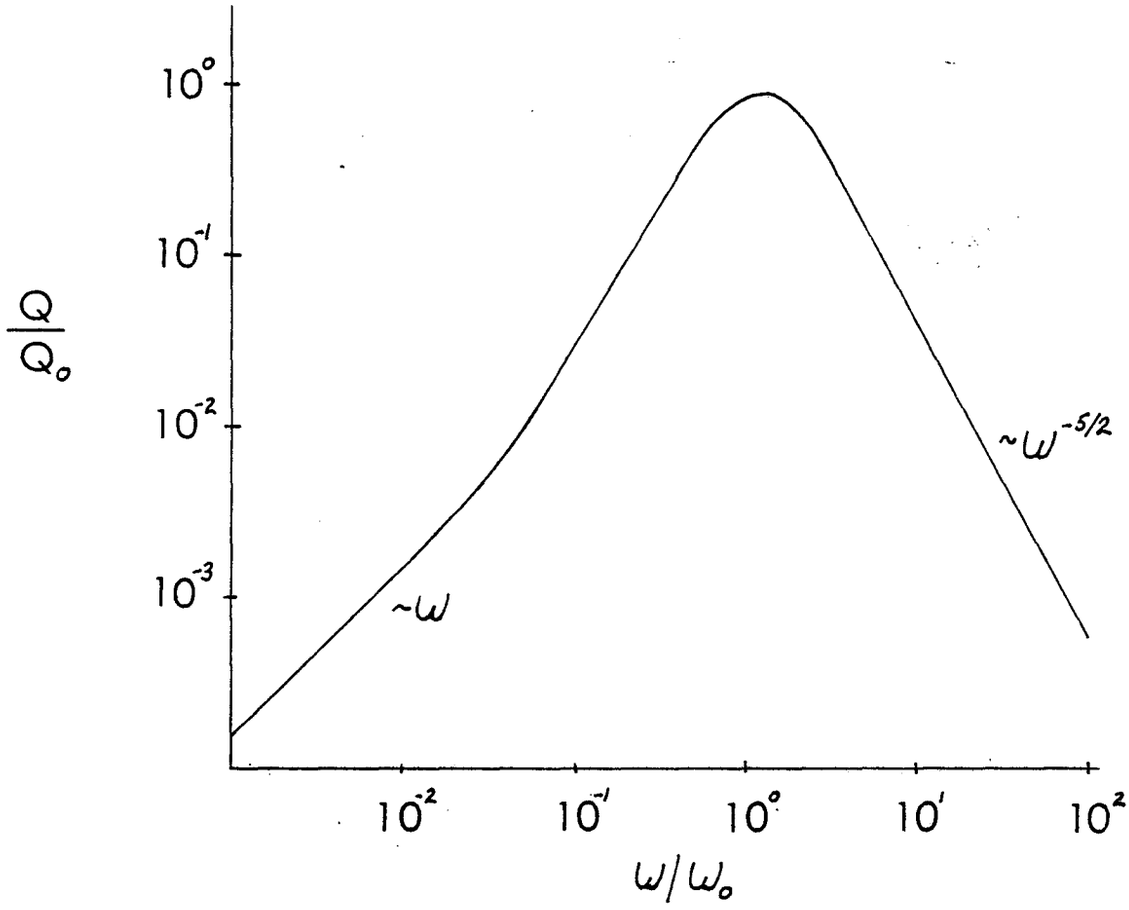

Figure 4. The frequency dependence of Q^{-1} for the parallel walled pore in compression.

Physically, the low frequency expressions ($\omega << 2\nu/a^2$) correspond to Poisseuille flow. That is, the inertial terms are negligible, and the flow is governed by the balance between viscous shear forces and the pressure gradient driving the flow. These viscous shear stresses are proportional to ω; the average dissipation goes as ω^2; and the dissipation during one period, $T = 2\pi/\omega$, varies as ω.

The fluid pressure P, varies as $\eta\omega\delta D^2/a^3$ at low frequencies. The pressure-shear balance is obvious here since peak velocity $\simeq \omega\delta D/a$, shear stress $\simeq \eta\omega\delta D/a^2$, and the integrated shear force over the drop length $\simeq \eta\omega\delta D^2/a^2$ this equals the change in pressure force over the length of the drop $\simeq Pa$. For the case of water, the low frequency pressure is usually small compared with the stress in the rock. Hence, at sufficiently low frequencies, the energy W is approximately the energy of a dry porous rock, independent of ω. The point at which the pressure dependent (i.e. frequency dependent) terms in W become comparable to the dry rock energy determines the position of the peak in Q^{-1} and can be found by examining equation (13). This point occurs at $\overline{P}/\varepsilon \simeq \mu\alpha_c$ (see appendix B). Depending on the viscosity and pore size, this point can occur either in the Poisseuille flow regime or in the higher range of inertial flow. When within the Poisseuille limits, the condition on $\overline{P}/\varepsilon$ is equivalent to $\omega_o \simeq 8\pi \frac{\mu}{\eta} \alpha_c^3$.

The condition for Poisseuille flow and therefore a condition on the low frequency form of Φ in table 1 corresponds to $z < 1$, $\omega < 2\nu/a^2$ or $f < \nu/\pi a^2$. For a water system $\nu = 0.01$ cgs, so that $f < 0.003/a$ where a^2 is in centimeters and f is in hertz. For the case of joints or fractures where $a \simeq 1$ mm, the low frequency expressions are restricted to frequencies below 0.3 hz; for pores or microcracks where $a \simeq 0.1$ mm,

the restriction is f < 30 hz. It would seem that for exploration frequencies the low frequency approximation is generally adequate. However, where unusually wide cracks or high frequencies are encountered (in the laboratory, for example) the other forms should be used.

The viscosity always appears with frequency as the product $\eta\omega$ in the poisseuille flow expressions (in table 1). This is a characteristic of viscous flow that can be particularly useful. For example in the laboratory, we can define $\eta\omega$ as an effective frequency $\omega' = \eta\omega$ and measure the frequency dependence of liquid-solid systems by varying either the real frequency ω or the fluid viscosity.

The dependence of Q^{-1} on crack shape and water content, given by $\beta/\alpha_f^2\alpha_c^2$ at the lowest frequencies is rather strong. Table 2 gives some numerical examples of Q^{-1} for several cases computed using the lowest frequency formula in table 1. The trend from top to bottom is to decrease each aspect ratio by a factor of 10. Although the total fluid content has also decreased by a factor of 10 from the first to last example, the attenuation has increased by three orders of magnitude. This is expected since the dependence is on the square of each aspect ratio and linear in fluid concentration. Examples 2 and 3 are for the same rock, i.e. identical pore shapes, and total porosity. In this case, the approximate doubling in saturation gives a factor of 10 increase in attenuation due to the combined changes in β and α_f.

Computed values of Q^{-1} for some specific rocks, Boise Sandstone, Bedford Limestone, and Troy Granite at 50 percent water saturation and f = 1.6 hz are shown in table 3. These are computed using the low frequency formula and aspect ratio data taken from Toksöz and others (1976). To estimate the upper limit of attenuation we assume for

f = 16 hz

β (%)	S(%)	α_c	α_w	Q^{-1}
.009	90	10^{-3}	$1.1\ 10^{-3}$	.0002
.005	50	$2 \cdot 10^{-4}$	$4 \cdot 10^{-4}$	.01
.009	90	$2 \cdot 10^{-4}$	$2.2 \cdot 10^{-4}$	.1
.0009	90	10^{-4}	$1.1 \cdot 10^{-4}$	.2

Table 2. Numerical examples of attenuation showing the strong aspect ratio dependence. β is the volume concentration of liquid, S is the saturation.

Table 3

Boise Sandstone

ψ	α_c	α_f	β	Q^{-1}
1.8×10^{-1}	1			
6.9×10^{-2}	$1.\times10^{-1}$			
$1.\times10^{-4}$	2.5×10^{-3}	$5.\times10^{-3}$	$5.\times10^{-5}$	5.4×10^{-7}
$1.\times10^{-4}$	$2.\times10^{-3}$	$4.\times10^{-3}$	$5.\times10^{-5}$	1.3×10^{-6}
1.5×10^{-4}	1.5×10^{-3}	$3.\times10^{-3}$	7.5×10^{-5}	6.2×10^{-6}
$2.\times10^{-4}$	$1.\times10^{-3}$	$2.\times10^{-3}$	$1.\times10^{-4}$	4.2×10^{-5}
$1.\times10^{-4}$	$5.\times10^{-4}$	$1.\times10^{-3}$	$5.\times10^{-5}$	3.3×10^{-4}
$2.\times10^{-5}$	$1.\times10^{-4}$	$2.\times10^{-4}$	$1.\times10^{-5}$	$4.\times10^{-2}$

Bedford Limestone

ψ	α_c	α_f	β	Q^{-1}
$1.\times10^{-1}$	1.			
$2.\times10^{-2}$	$1.\times10^{-1}$			
2.5×10^{-3}	$1.\times10^{-2}$	$2.\times10^{-2}$	1.2×10^{-3}	$5.\times10^{-8}$
$5.\times10^{-4}$	$5.\times10^{-3}$	$1.\times10^{-2}$	2.5×10^{-4}	1.7×10^{-7}
$5.\times10^{-4}$	$4.\times10^{-3}$	$8.\times10^{-3}$	2.5×10^{-4}	4.1×10^{-7}
$7.\times10^{-4}$	$3.\times10^{-3}$	$6.\times10^{-3}$	3.5×10^{-4}	1.8×10^{-6}
$6.\times10^{-4}$	$2.\times10^{-3}$	$4.\times10^{-3}$	$3.\times10^{-4}$	7.9×10^{-6}
$4.\times10^{-4}$	1.5×10^{-3}	$3.\times10^{-3}$	$2.\times10^{-4}$	1.7×10^{-5}
$5.\times10^{-4}$	$1.\times10^{-3}$	$2.\times10^{-3}$	2.5×10^{-4}	$1.\ 10^{-4}$

(Table 3 continued)

Troy Granite

ψ	α_c	α_f	β	Q^{-1}
$1. \times 10^{-3}$	1.			
$5. \times 10^{-4}$	$1. \times 10^{-1}$			
1.5×10^{-3}	$1. \times 10^{-2}$	$2. \times 10^{-2}$	7.5×10^{-4}	$3. \times 10^{-8}$
$5. \times 10^{-5}$	$5. \times 10^{-4}$	$1. \times 10^{-3}$	2.5×10^{-5}	1.7×10^{-4}
7.5×10^{-5}	$4. \times 10^{-4}$	$8. \times 10^{-4}$	3.5×10^{-5}	5.8×10^{-4}
$1. \times 10^{-4}$	$2.5 \times 1-^{-4}$	$5. \times 10^{-4}$	$5. \times 10^{-5}$	5.4×10^{-3}
$5. \times 10^{-5}$	$1. \times 10^{-4}$	$2. \times 10^{-4}$	2.5×10^{-5}	$1. \times 10^{-1}$
$5. \times 10^{-6}$	$1. \times 10^{-5}$	$2. \times 10^{-5}$	2.5×10^{-6}	

simplicity that all pores are oriented alike, and that each pore is exactly half or 90 percent filled with water. The contributions from the first two pore shapes from each rock type are not computed because the quantitative reliability of the model is low for such large aspect ratios. However, the trend indicates that smaller aspect ratios dominate the overall behavior, almost independent of the porosity of each aspect ratio group. The Q^{-1} for the last two pore shapes for Boise Sandstone and Troy Granite are calculated using equation (14) since for these extremely small aspect ratios, the low frequency assumption of a negligible fluid pressure used to calculate W breaks down, even though the flow is still in the Poisseuille regime. All three rock types show a similar sensitivity to saturation and a dominance of flatter pores or cracks in determining the overall attenuation. Although the three rocks are very different in nature, the population of small aspect ratio cracks is somewhat similar in each.

The high frequency behavior of dissipation and attenuation, table 1, is governed by the increasing importance of fluid inertial stresses with respect to viscous stresses. In particular, the high frequency limit of pressure is a balance between pressure gradient $\simeq P/D$ and inertial stress $\simeq \rho(\omega^2 \varepsilon D)$ where $\omega^2 \varepsilon D$ gives the acceleration. The peak in Q^{-1} occurs where the stored energy W transitions from the constant dry rock value to the pressure dependent high frequency value. As mentioned above this occurs at $P/\varepsilon \simeq \mu\alpha_c$. When the peak occurs in inertial flow, the P/ε condition is equivalent to $\omega_o \simeq \sqrt{\frac{8\pi\mu\alpha_c^3}{\rho a_o^2}}$.

Shear Component of Excitation

Consider once again the nearly parallel walled pore of width $2a_o$ over the region occupied by the drop of length 2D. This time the pore is excited by a pure shear in the plane of the pore as shown in figure 5. The equation of motion is

$$\frac{\partial u}{\partial t} = \nu \frac{\partial^2 u}{\partial y^2}$$

with the boundary conditions on velocity of:

$$u = \begin{cases} i\omega\delta e^{i\omega t} & y = +a_o \\ -i\omega\delta e^{i\omega t} & y = -a_o \end{cases}$$

at the upper and lower pore walls respectively. The flow field can easily be found:

$$u(y,t) = \frac{\delta \sinh\left(y\sqrt{\frac{i\omega}{\nu}}\right)}{\sinh\left(a_o\sqrt{\frac{i\omega}{\nu}}\right)} e^{i\omega t} \tag{18}$$

The energy dissipated in the entire pore during one cycle is found exactly as in the compressional problem and is given by

$$\Phi_{shear} = \frac{2\omega^2\pi\eta\delta^2 Dd}{\nu} \frac{\sinh\sqrt{\frac{2\omega}{\nu}}\, a + \sin\sqrt{\frac{2\omega}{\nu}}\, a}{\sinh^2\sqrt{\frac{\omega}{2\nu}}\, a \cos^2\sqrt{\frac{\omega}{2\nu}}\, a + \cosh^2\sqrt{\frac{\omega}{2\nu}}\, a \sin^2\sqrt{\frac{\omega}{2\nu}}\, a} \tag{19}$$

or in the limits of high and low frequency:

$$\Phi_{shear} = \begin{cases} 4\pi\omega\eta\varepsilon^2 Dad & \omega << 2\nu/a^2 \\ 4\pi\omega^2\eta\delta^2 Dd\sqrt{\frac{\nu}{2\omega}} & \omega >> 2\nu/a^2 \end{cases} \tag{20}$$

The relative importance of dissipation is shear and compression for this geometry is found by taking a simple ratio Φ (compression)/Φ (shear) with identical pores and fluid and equal amounts of peak pore displacements. Using equation (20) and table 1:

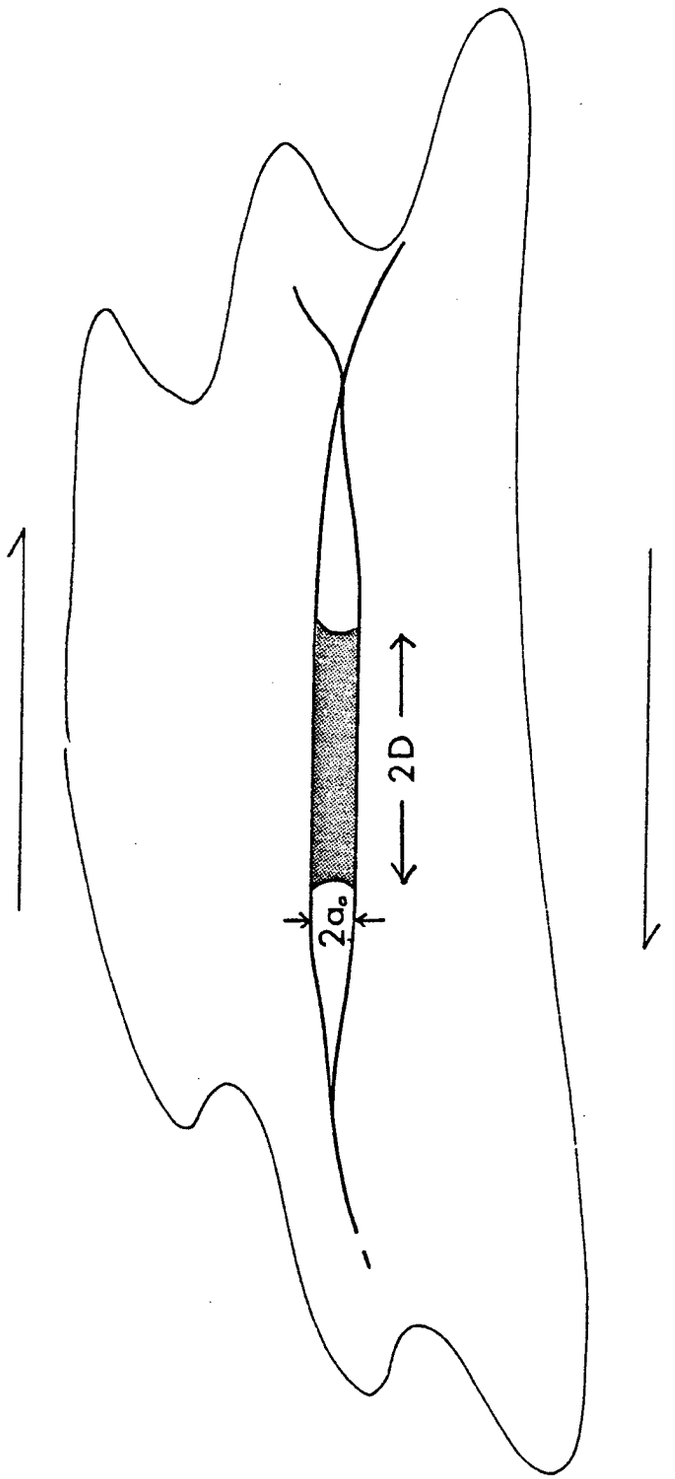

Figure 5. Nearly parallel walled pore in shear.

$$\frac{\Phi_{\text{compression}}}{\Phi_{\text{shear}}} = \begin{cases} 1/\alpha_f^2 & \omega << 2\nu/a^2 \\ 1/3\ \alpha_f^2 & \delta >> 2\nu/a^2 \end{cases} \tag{21}$$

It is clear that for small aspect ratios the dissipation is shear will be many orders of magnitude smaller than for compression in either limit. The interpretation of this is simple. The fluid velocity in the shear case is approximately the pore wall velocity $\simeq\omega\delta$. This gives an average fluid shear stress of $\eta\omega\delta/a$. On the other hand, the fluid velocity in the compressional case is on the order of $\simeq\omega\delta/\alpha_f^2$, with a fluid shear stress $\simeq\eta\omega\delta/\alpha_f^2 a$. The flow in compression is amplified by the aspect ratio.

We should emphasize that these analyses of dissipation in shear and compression refer to the shear and compressional components of stress resolved on each individual crack. The results are not identically the dissipation that would be associated with S and P wave propagation. For either type of wave, each crack depending on its orientation, would have both a shear and compressional contribution to energy dissipation in the fluid and strain energy stored in the elastic matrix.

Other Geometries

The parallel pore is particularly useful in understanding the characteristics of the model because the integral in equations (6) and (13) for compressional dissipation can very easily be evaluated. For other simple pore geometries the integral can also be evaluated if we work in the low frequency regime such that $R(z) \simeq 1$.

Consider the two geometries shown in figure 6. In each case the pore half width is given by $a(x) = a_o(x/c)^n$, $n = 1, 2$, and the maximum

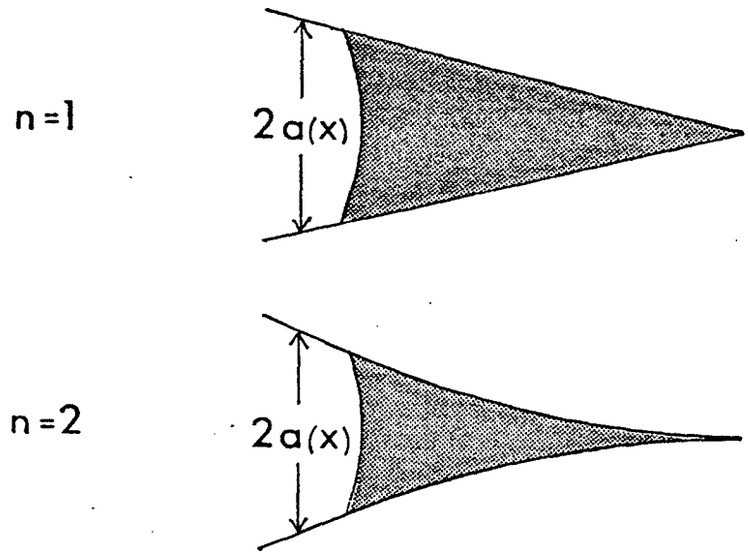

Figure 6. Two simple drop geometries. The upper drop is a linear or triangular wedge. The lower drop has parabolic shape.

pore displacement is δ. Using formula (6) we first note that

$$A(x) = \frac{2a_o}{c^n} \frac{x^{n+1}}{n+1} e^{i\omega t}$$

or

$$\ddot{A}A^* = \frac{4\omega^2\delta^2}{c^{2n}} \frac{x^{2n+2}}{(n+1)^2} \tag{22}$$

The dissipation Φ is then

$$\Phi = \begin{cases} \dfrac{3\pi\eta\omega\varepsilon^2\nu}{\alpha_f^2} & n = 1 \\ \dfrac{4\pi\eta\omega\varepsilon^2\nu}{\alpha_f^2} & n = 2 \end{cases} \tag{23}$$

This result compared with table 1 for the parallel pore suggests that for low frequencies the fluid dissipation can be approximated for a variety of geometries by

$$\Phi \simeq g \frac{n\omega\varepsilon^2\nu}{\alpha_f^2} \tag{24}$$

where g is a geometric factor which we have found to vary from π to 4π for the specific geometries studied. This rather weak dependence on geometry suggests that the results derived for the parallel pore have general applicability, particularly for order-of-magnitude behavior.

Comparison with Other Models

Perhaps the most comprehensive single treatment of wave propagation incorporating dissipative fluid motion was presented by Biot (1956a, b). His formulation assumes a fully saturated porous material and includes the effects of fluid compressibility and coupled fluid and solid stress. At low frequencies the relative fluid flow is assumed to resemble Poisseuille flow in a flat or circular duct, while at higher frequencies inertial terms are also included (laminar flow is always.

assumed). This microscopic flow field is used only to establish a frequency dependent proportionality between the average flow and the stresses transmitted to the solid rock. Details of pore shape and local flow are thereafter neglected and lumped into parameters which relate only the averaged solid and fluid motions on a scale much greater than the pore size.

The elimination of local flow and the condition of complete liquid saturation treated by Biot severely limit the amount of flow and dissipation that can occur under wave excitation. White (1965, p. 133) shows that for the saturated medium, the only sources of relative fluid motion from the passing wave are viscous drag due to acceleration of the solid with respect to the fluid and pressure gradients between the peak and trough of the passing wave. His numerical example of a water-saturated sandstone shows negligible dissipation.

In our model we specifically neglect the large-scale acceleration and diffusion and look only at the local flow. In this sense our mechanism of dissipation is more a point property. In addition, the undersaturation provides a strong local heterogeneity which causes locally high pressure gradients and flow.

At low frequencies Q^{-1} is proportional to ω in both Biot's model and ours, although the magnitude of attenuation is much greater in ours. At higher frequencies the dependence is quite different. Biot's expression for Q^{-1} varies as $\omega^{-\frac{1}{2}}$ while ours varies in a complicated fashion toward $\omega^{-5/2}$ at very high frequencies.

Another model of attenuation in porous media is by White (1975). His treatment resembles Biot's in that lumped parameters describe the material and flow properties on a scale much greater than a pore

dimension. Only low frequency viscous flow is considered. White includes undersaturation by considering regions of dry rock containing many pores imbedded in regions of saturated rock also containing many pores. High pressure gradients and flow occur at the contact between wet and dry rock and result in large attenuation. At low frequencies White's expression for Q^{-1} varies as ω while at higher frequencies (still within the Poisseuille range) Q^{-1} goes as ω^{-1}. A similar dependence is predicted by our model for the two frequency ranges within Poisseuille flow shown in table 1. The only physical comparison we can make between the two models is to suggest that the contact region between wet and dry in White's model is somehow similar to our description of the individual partially saturated pores.

Discussion

We have presented a simple model to describe the attenuation of seismic waves in rocks with partially liquid saturated flat cracks or pores. In this study the presence of at least a small fraction of a highly compressible gaseous phase permits the fluid to flow freely when the pore is compressed under seismic excitation. This leads to viscous shearing in the fluid and high energy dissipation. In general, the attenuation increases with increasing liquid concentration. However, only partially saturated pores contribute, and as successive pores saturate, the attenuation will fall off. In the limit of complete saturation the flow is stifled and the attenuation is expected to essentially disappear as is predicted by Biot's formulation. Likewise, the dissipation from pure shear distortion of the rock, whether completely saturated or not is negligible.

For compressional waves the attenuation or Q^{-1} is found to be extremely sensitive to the aspect ratios of the pores and the liquid droplets occupying the pores, with flatter pores and drops resulting in higher attenuation.

Details of pore shape other than aspect ratio appear to have little effect on the general behavior provided the crack width is slowly varying over the length of the liquid drop.

A limiting factor in actual values of attenuation in the laboratory and in situ is the distribution of liquid throughout the various shaped pores. Our results indicate that a wide variety of rock types have a sufficient number of flat pores to produce measureable attenuation in principle. However, if significant number of these pores are either empty or completely saturated, the attenuation will drop. Factors like temperature, surface tension (capillarity), and liquid and gas pressure must be considered.

APPENDIX A

THE FLUID EQUATION OF MOTION

In our treatment of fluid flow within the individual pores of a rock we assume that the fluid behaves as though incompressible. Usually the principal requirement for this to be approximately true is that the fluid speed be small compared to the speed of sound V_p (Batchelor, 1967, p. 174). Our results indicate that the peak fluid velocity is on the order of $\omega\varepsilon D$. Then for incompressible flow we demand

$$\omega\varepsilon D << V_p = \sqrt{\frac{K_f}{\rho}}$$

For water $V_p \simeq 10^3$ m/sec and for strains $\varepsilon < 10^{-4}$ this becomes

$$\omega D << 10^7 \text{ m/sec} \qquad \text{A1}$$

A second requirement that we can impose is that the volumetric strain due to fluid compression be small compared with the volumetric strain imposed as a boundary condition, i.e.

$$\frac{P}{K_f} << \frac{\delta}{a_o} = \varepsilon$$

Our results give a peak fluid pressure of

$$P \simeq \begin{cases} \dfrac{\eta\omega\varepsilon D^2}{a_o^2} & \omega \text{ small} \\ \omega^2\rho D^2\varepsilon & \omega \text{ large} \end{cases}$$

Then the requirement becomes

$$\frac{\eta\omega\varepsilon D^2}{a_o^2 K_f} << \varepsilon \Rightarrow \frac{\eta\omega D^2}{a_o^2} << K_f \qquad \omega \text{ small}$$

$$\frac{\omega^2\rho D^2\varepsilon}{K} << \varepsilon \Rightarrow \omega^2 D^2 << \frac{K_f}{\rho} = V_p^2 \qquad \omega \text{ large}$$

These are more restrictive than A1. For water $K_f = 2 \cdot 10^{10}$ dyne/cm^2 and $\eta \simeq 10^{-2}$ dyne-sec/cm^2. Therefore we require:

$$\frac{\omega}{\alpha_f^2} << 2 \cdot 10^{12} \text{ sec}^{-1} \qquad \omega \text{ small}$$

$$\omega D << 10^5 \text{ cm/sec} \qquad \omega \text{ large}$$

Within these bounds of incompressibility then the equation of motion for the fluid is (Batchelor)

$$\rho \frac{Du_i}{Dt} = - \frac{\partial P}{\partial X_i} + \eta \nabla^2 u_i$$

where $D/Dt = \partial/\partial t + \bar{u} \cdot \nabla$. We will assume that η is constant with time and position.

For two dimensional pore, $\bar{u}_z = \frac{\partial}{\partial z} = 0$. Furthermore if the pore width is slowly varying, i.e., $\frac{1}{a} \frac{\partial a}{\partial x} << 1$ and the pore strains are very small, then the flow is approximately unidirectional and we can neglect the terms $u \frac{\partial u}{\partial x}$ and $\frac{\partial^2 u}{\partial x^2}$. Hence the equation of motion becomes

$$\rho \frac{\partial u}{\partial t} = - \frac{\partial P}{\partial x} + \eta \frac{\partial^2 u}{\partial y^2}$$

APPENDIX B

FREQUENCY-DEPENDENT EXPRESSIONS AND THEIR LIMITING FORMS

The frequency dependence of Φ and $P(x)$ is found as follows. The flow field is given by equation (6):

$$u(x,y) = \frac{-\dot{A}(x)}{2a(x)} \frac{1 - \dfrac{\cosh\sqrt{\frac{i\omega}{\nu}}\, y}{\cosh\sqrt{\frac{i\omega}{\nu}}\, a}}{1 - \frac{1}{a}\sqrt{\frac{\nu}{i\omega}}\tanh\sqrt{\frac{i\omega}{\nu}}\, a}$$

The shear stress $\tau = \eta \dfrac{\partial u}{\partial y}$ is then

$$\tau(x,y) = \frac{\eta\dot{A}(x)}{2a} \frac{\sqrt{\frac{i\omega}{\nu}}}{\left[1 - \frac{1}{a}\sqrt{\frac{\nu}{i\omega}}\tanh\sqrt{\frac{i\omega}{\nu}}\, a\right]} \frac{\sinh\sqrt{\frac{i\omega}{\nu}}\, a}{\cosh\sqrt{\frac{i\omega}{\nu}}\, a}$$

The average dissipation rate per unit volume of fluid is given by

$$\frac{1}{2\eta}\tau\tau^* = \frac{\omega\rho}{8a^2}\frac{\dot{A}\dot{A}^*}{T(z)}\left[\frac{\sinh^2\sqrt{\frac{\omega}{2\nu}}\, y\cos^2\sqrt{\frac{\omega}{2\nu}}\, y + \cosh^2\sqrt{\frac{\omega}{2\nu}}\, y\sin^2\sqrt{\frac{\omega}{2\nu}}\, y}{\cosh^2 z\cos^2 z + \sinh^2 z\sin^2 z}\right]$$

where

$$T(z) = 1 - \frac{1}{z}\left[\frac{\tanh z + \tanh z\tan^2 z - \tanh^2 z\tan z + \tan z}{1 + \tanh^2 z\tan^2 z}\right] + \frac{1}{2z^2}\left[\frac{\tanh^2 z + \tan^2 z}{1 + \tanh^2 z\tan^2 z}\right]$$

$$z = a\sqrt{\frac{\omega}{2\nu}}$$

Finally, integrating over the volume and period gives

$$\Phi = \int_0^D \frac{\pi d\eta\dot{A}\dot{A}^* z}{4a^3\omega T(z)}\left[\frac{\sinh 2z - \sin 2z}{\cosh^2 z\cos^2 z + \sinh^2 z\sin^2 z}\right] dx$$

$$= \frac{3}{2}\frac{\pi\eta d}{\omega}\int_0^D \frac{\dot{A}\dot{A}^*}{a^3} R(z)dx$$

$$R(z) = \frac{z}{6T(z)} \left[\frac{\sinh 2z - \sin 2z}{\cosh^2 z \cos^2 z + \sinh^2 z \sin^2 z} \right]$$

The asymptotic expressions given in table 1 are found by noting that at large z, sinh z ≃ cosh z and at small z by expanding the trigonometric and hyperbolic functions in power series and dropping higher order terms. Hence the definition of large and small z is $z >> 1$ and $z << 1$ respectively or in terms of ω: $\omega >> \frac{2\nu}{a}$, $\omega << \frac{2\nu}{a}$.

The peak pressure P(x) is obtained by taking the real part of the integral of equation (5):

$$\frac{\partial P}{\partial x} = \frac{\dot{A}(x) i\omega\rho}{2a\left[1 - \frac{1}{a}\sqrt{\frac{\nu}{i\omega}} \tanh\sqrt{\frac{i\omega}{\nu}}\, a\right]}$$

$$P(x) = \mathrm{Re}\left[P_o + \int_0^x \frac{\partial P}{\partial x}\, dx\right]$$

For the parallel drop we set $\dot{A}(x) = 2x\varepsilon a_o i\omega$, and assume for simplicity that the pressure at the edge of the drop, x = D, is zero, $P_o = 0$. This gives

$$P(x) = \frac{\omega^2\varepsilon\rho}{2} (D^2 - x^2)\mathrm{Re}\left[1 - \frac{1}{a}\sqrt{\frac{\nu}{i\omega}} \tanh\sqrt{\frac{i\omega}{\nu}}\, a\right]^{-1}$$

$$= \frac{\omega^2\varepsilon\rho}{2} (D^2 - x^2) Y(z)$$

$$Y(z) = \frac{(\cosh 2z + \cos 2z)\left[(\cosh 2Z + \cos 2Z) - \frac{1}{2z}(\sinh 2z + \sin 2z)\right]}{\left[(\cosh 2z + \cos 2z)\cdot\frac{1}{2z}(\sinh 2z + \sin 2z)\right]^2 + [\sin z - \sinh z]^2}$$

$$z = a\sqrt{\frac{\omega}{2\nu}}$$

To find the equivalent pressure $\overline{P}$ for the case of a drop centered in the pore we plug this value of P(x) into equation (12):

$$\overline{P} = \frac{\omega^2\varepsilon\rho}{2} Y(z) \frac{2}{\pi} \int_{-D}^{D} \frac{(D^2 - x^2)\left[\left(\frac{x}{c}\right)^2 - \left(\frac{x}{c}\right)\right]}{\sqrt{c^2 - x^2}}\, dx$$

$$= \frac{\omega^2\varepsilon\rho c^2}{2\pi} \gamma Y(z)$$

where

$$\gamma = [(\frac{3}{2} - \frac{D^2}{c^2}) \frac{D}{c}\sqrt{1 - (\frac{D}{c})^2} + [2(\frac{D}{c}) - \frac{3}{2}] \sin^{-1} \frac{D}{c}]$$

The high and low frequency limits of Y(z) are found in the same manner as R(z).

The frequency at which the pressure dependent terms in W become comparable to the dry rock energy can be found by examining equation (13):

$$W = \frac{8}{27} \mu V \alpha_c^2 \varepsilon^2 (1 + \frac{9}{4} \frac{\psi}{\alpha_c}) + \frac{\mu V}{6} (\frac{\overline{P}}{\mu}) [\frac{8}{3} \alpha_c \varepsilon (1 + \frac{9}{8} \frac{\psi}{\alpha_c}) + (\frac{\overline{P}}{\mu})]$$

The second term equals the first at

$$\frac{\overline{P}}{\varepsilon} = \frac{4}{3} \mu \alpha_c (1 + \frac{9}{8} \frac{\psi}{\alpha_c}) \left\{ \left[1 + \frac{(1 + \frac{9}{4} \frac{\psi}{\alpha_c})}{(1 + \frac{9}{8} \frac{\psi}{\alpha_c})^2} \right]^{1/2} - 1 \right\}$$

In either limit $\psi << \alpha_c$ or $\psi >> \alpha_c$ this becomes

$$\frac{\overline{P}}{\varepsilon} \simeq \mu \alpha_c$$

although for noninteracting cracks we are restricted to $\psi < \alpha_c$.

Setting $\gamma = 1/2$ and using the high and low frequency expressions for Y(z) from table 1 we have:

$$\frac{\overline{P}}{\varepsilon} \simeq \begin{cases} \frac{9}{64\pi} \frac{\omega \eta}{\alpha_c^2} & \omega \text{ small} \\ \frac{\omega^2 \rho c^2}{8\pi} & \omega \text{ large} \end{cases}$$

Then in terms of ω the transition in W occurs at

$$\omega \simeq \frac{8\pi\mu\alpha_c^3}{\eta} \qquad \omega \text{ small (Poisseuille)}$$

$$\omega \simeq \sqrt{\frac{8\pi\mu\alpha_c^3}{\rho a^2}} \qquad \omega \text{ large (inertial)}$$

APPENDIX C

SHAPE APPROXIMATIONS IN CALCULATING ENERGIES

The separate calculation of Φ and W assumes a certain degree of uncoupling between the details of the fluid flow field and strain field in the rock around the pore. In a rigorous approach the pore strain ε in equation (2) is a function of x and is coupled to the fluid pressure distribution P(x).

The general form for the dissipation Φ is given by equation (7) as a function of $\dot{A}$ where

$$\dot{A}(x) = 2 \int_0^x \frac{\partial}{\partial t} \tilde{a}(x,t)dt$$

This can be rewritten using (2) as

$$\dot{A} = 2i\omega e^{i\omega t} \int_0^x a(x)\varepsilon(x)dx$$

In our calculations for specific geometries we simplify the integral by replacing $\varepsilon(x)$ by an appropriate average constant value ε such that

$$\dot{A} \simeq 2i\omega\varepsilon e^{i\omega t} \int_0^x a(x)dx$$

We further assume that this constant value of ε is approximately the strain that would occur for a uniformly pressurized pore deforming as equation (10).

In general the pore wall displacement S(x) resulting from uniform confining pressure and uniform pore pressure will depend on the details of crack shape. However, Mavko and Nur (1977a) have shown for a broad

class of 2-D flat crack shapes that for very small increments of loading, as we might expect from a passing wave, the incremental change of pore shape is elliptical in form, i.e.

$$\frac{\partial a(x)}{\partial \sigma} = \frac{2c(1-\xi^2)}{E}\sqrt{1 - \left(\frac{x}{c}\right)^2}$$

Then we can approximate s(x) by

$$S(x) = \frac{\partial a}{\partial \sigma}(\sigma - \bar{P}) = \frac{2(\sigma - \bar{P})c(1 - \xi^2)}{E}\sqrt{1 - \left(\frac{x}{c}\right)^2}$$

which is equation (10). The maximum displacement is $S(0) = 2(\sigma-\bar{P})c(1-\xi^2)/E$. Comparing with equation (2) the maximum displacement is $a_o\varepsilon$ so that we set

$$\frac{2(\sigma - P)c(1 - \xi^2)}{E} \simeq a_o\varepsilon$$

Equation (8) shows that the energy W depends only on the integral of crack displacement $\bar{S} = \int_{-c}^{c} S(x)dx$. Hence, for calculating W any approximation of pore wall deformation S(x) is valid as long as it has the correct average value $\bar{S}$. Mavko and Nur (1977b) have shown that for a broad class of 2-D flat cracks the integrated displacement due to pressure distribution P(x) is exactly the same as for a uniform pressure $\bar{P}$ where $\bar{P}$ is an appropriately weighted average of P(x), equation (12).

APPENDIX D

The pore pressure term in equation (8) can be shown negligible as follows. Since the bulk modulus of water K_f is less than M, the modulus of rock then

$$2d \int_{-c}^{c} P(x) \frac{\sigma}{M} a(x)dx < 2d \int_{-c}^{c} P(x) \frac{\sigma}{K_f} a(x)dx$$

In appendix A we require for the incompressible analysis to be valid that $P << \varepsilon K_f$, then

$$2d \int_{-c}^{c} \frac{P(x)}{K_f} \sigma \, a(x)dx << 2d \int_{-c}^{c} \sigma\varepsilon \, a(x)dx$$

But by equation (2), $\varepsilon a(x) \simeq S(x)$:

$$2d \int_{-c}^{c} \sigma\varepsilon \, a(x)dx \simeq 2d \, \sigma \int_{-c}^{c} S(x)dx$$

Therefore

$$2d \int_{-c}^{c} P(x) \frac{\sigma}{M} a(x)dx << 2d\sigma \int_{-c}^{c} S(x)dx$$

References

Anderson, Don L. and Harmut Spetzler, Partial melting and the low velocity zone, Phys. Earth Planet Interiors, 4, 62-64, 1970.

Batchelor, G. K., An Introduction to Fluid Dynamics, Cambridge University Press, 1967.

Biot, M. A., Theory of propagation of elastic waves in a fluid-saturated porous solid. I. Low-frequency range, J. Acoustical Soc. of Am., 28,2, 168-178, 1956a.

Biot, M. A., Theory of propagation of elastic waves in a fluid-saturated porous solid.II. Higher frequency range, J. Acoustical Soc. Am., 28, 2, 179-191, 1956b.

Domenico, S. N., Effect of water saturation on seismic reflectivity ofsand reservoirs encased in shale, Geophysics, 39, 6, 759-769, 1974.

Elliot, S. E. and B. F. Wiley, Compressional Velocities of partially saturated, unconsolidated sands, Geophysics, 40, 6, 949-954,1975.

Jaeger, J. C. and N. G. W. Cook, Fundamentals of Rock Mechanics: London, Methuen and Co. Ltd., 1969.

Kuster, G. T. and M. N. Toksöz, Velocity and attenuation of seismic waves in two-phase media: Part I. Theoretical formulations, Geophysics, 39, 5, 587-606, 1974a.

Kuster, G. T. and M. N. Toksöz, Velocity and attenuation of seismic waves in two-phase media: Part II. Experimental results, Geophysics, 39, 5, 607-618, 1974b.

Mavko, G. and A. Nur, The effect of non-elliptical cracks on the compressibility of rocks, J. Geophys. Res., preprint, 1977a.

Mavko, G. and A. Nur, Unpublished manscript, 1977b.

Nur, A., Viscous phase in rocks and the low-velocity zone, Phys. Earth Planet. Interiors, 4, 62-64, 1970.

Nur, A., Role of pore fluids in faulting, Phil. Trans. R. Soc. Lond. A, 274, 297-304, 1973.

Solomon, S. C., Seismic wave attenuation and partial melting in the upper mantle of North America, J. Geophys. Res., 77, 8, 1483-1502, 1972.

Toksöz, M. N., C. H. Cheng, and A. Timur, Velocities of seismic waves in porous rocks, Geophysics, 41, 4, 621-645, 1976.

Walsh, J. B., The effect of cracks on the compressibility of rock, J. Geophys. Res., 70, 2, 381-389, 1965a.

Walsh, J. B., The effect of cracks on the uniaxial elastic compression of rocks, J. Geophys. Res., 70, 2, 399-411, 1965b.

Walsh, J. B., New analysis of attenuation in partially melted rocks, J. Geophys. Res., 74, 4333-4337, 1969.

White, J. E., Seismic Waves: New York, McGraw-Hill Book Co., Inc., 1965.

White, J. E., Computed seismic speeds and attenuation in rocks with partial gas saturation, Geophysics, 40, 2, 224-232, 1975.